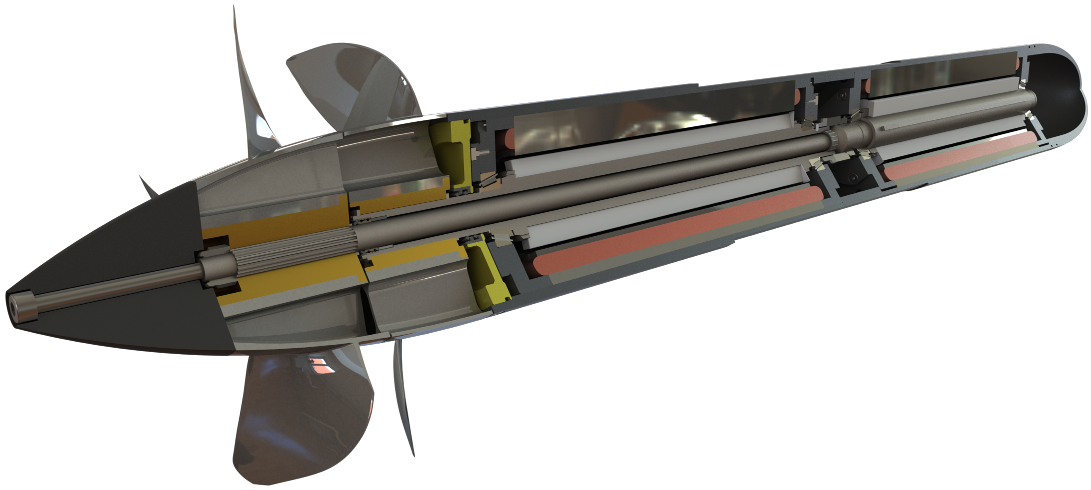

MPSD - Marine propulsion system design applied to Técnico Solar Boat prototype

Robin Rauterberg Tomaz

Thesis to obtain the Master of Science Degree in

Mechanical Engineering

Supervisor: Prof. João Manuel Ribeiro Costa Baltazar

Examination Committee

Chairperson: Prof. José Manuel da Silva Chaves Ribeiro Pereira
Supervisor: Prof. João Manuel Ribeiro Costa Baltazar
Member of the Committee: Prof. José Alberto Caiado Falcão de Campos

November 2023

Declaração

Declaro que o presente documento é um trabalho original da minha autoria e que cumpre todos os requisitos do Código de Conduta e Boas Práticas da Universidade de Lisboa.

Declaration

I declare that this document is an original work of my own authorship and that it fulfils all the requirements of the Code of Conduct and Good Practices of the Universidade de Lisboa.

Dedicated to the entire Técnico Solar Boat team

Acknowledgments

First and foremost, I would like to thank all of Técnico Solar Boat team. The work done in this thesis and the motivation to do it could not have been possible without your help. For the last five and a half years, I have had the opportunity and fortune to work with some of the most incredible people within Técnico Solar Boat. It was for sure a wonderful experience.

Thank you also to everyone who has been part of this team for making this project such a great one.

I would like to thank my friends who helped me find every mistake and made awesome suggestions that transformed this work into something I can truly be proud of. Special thanks go to: Milo Marques, Mariana Viegas, Sebastião Beirão and Beatriz Silva who suported me the most.

I would also like to express my gratitude towards my supervisor, Prof. João Baltazar, for helping and guiding me throughout this thesis and for his corrections and suggestions that certainly made my thesis a lot better. My thanks extend also to Prof. João Fernandes and PhD student Pedro Bhagubai for their input and help on the design of the electric motor.

Finally, a special thanks to my parents and brother for all their lessons and support, for always pushing me forward throughout my student years, and for investing in my future. Another word goes to my grandmother, for her teachings and for always caring about me.

Abstract

Since 2015 Técnico Solar Boat (TSB), a student project from Instituto Superior Técnico (IST), develops manned competition boats powered exclusively by renewable energies. The project started with solar-powered boats, but nowadays, hydrogen-powered boats are also developed. TSB's boats are designed to participate in international competitions that take place in Portugal, the Netherlands and Monaco. The main goal of this thesis is to design a propulsion system for TSB's open sea boats.

The system being developed is a unified drive system that encompasses the electric motors and the propellers. The electric motors receive their energy from a hydrogen fuel cell and a supercapacitor which then convert this energy to mechanical rotational energy and are coupled to the propellers, which in turn, produce the necessary thrust for the propulsion of the vessel.

A set of requirements imposed by the competition's regulations and others imposed by the team have to be respected. Given the characteristics of the vessel in which the system will be implemented, the proposed Marine Propulsion System (MPS) should be as reliable as possible so that the endurance race can be completed safely. The system should also be lightweight.

For the optimisation of the MPS a Genetic Algorithm (GA) is used for both the electro-magnetic design of the electric motor and the hydrodynamical design considering the Contra-Rotating Propellers (CRP). Post optimisation analyses were performed to verify the obtained results and a Three Dimensional (3D) engineering model is presented along with the mechanical design of critical connections, such as shaft splines, bearings, and sealants.

Keywords: Marine propellers, Electric Motors, Hydrogen-Powered Boat, Electrical Vehicle, Genetic Algorithm.

Resumo

Desde 2015 que o Técnico Solar Boat (TSB), um projeto de alunos do Instituto Superior Técnico (IST), desenvolve barcos de competição movidos exclusivamente a energias renováveis. No início apenas eram desenvolvidos barcos solares, no entanto, hoje em dia, também já são desenvolvidos barcos movidos a hidrogénio. Os barcos do TSB são desenvolvidos para participar em competições internacionais que têm lugar em Portugal, nos Países Baixos e no Mónaco. O objetivo principal desta dissertação é projetar um sistema de propulsão marítimo para os barcos de alto mar do TSB.

Um conjunto de requisitos definidos pelo regulamento da competição assim como outros impostos pela equipa deverão ser respeitados. Dadas as características do barco no qual o sistema será implementado, é fundamental que o sistema proposto seja fiável, de forma a que as provas de resistência possam ser realizadas em segurança. O sistema deverá também ser o mais leve possível de modo a maximizar o rendimento do barco.

Para a optimização um algoritmo genético foi utilizado para o projeto eletromagnético dos motores eletricos tal como para o design hidrodinâmico do sistema CRP. Posteriormente, uma análise dos resultados obtidos foi realizada para verificar a otimização, e um modelo de engenharia 3D foi desenvolvido juntamente com um projeto mecânico das ligações críticas, tais como, o veio, rolamentos e vedantes.

Palavras-chave: Sistema de Propulsão Marítimo, Motores Elétricos, Barco Movido a Hidrogénio, Veículo Elétrico, Algoritmo de Optimização Genético.

Contents

List of Figures **xiii**

List of Tables **xvii**

Acronyms **xix**

1 Introduction **1**

1.1 Objectives and Goals of the Dissertation 4

1.2 Thesis Outline 5

2 Technical Overview **7**

2.1 Electric Race Boat 8

2.1.1 SG01 Prototype 9

2.2 Electric Machine Design and Approaches 11

2.2.1 Electric Motor Components 12

2.2.2 Types of Electrical Machines 13

2.2.3 Synchronous Machine Overview 14

2.3 Marine Propeller Design and Approaches 20

2.3.1 Types of Propulsors 20

2.3.2 Contra-Rotating Propeller Overview 23

2.3.3 Propeller Materials and Manufacturing Considerations 25

3 MPS Design Parameters **27**

3.1 Design Parameters 28

3.1.1 Vessel Resistance Overview 28

3.1.2 CRP Design Parameters 36

3.1.3 Motor Design Parameters 37

4 MPS Detailed Design Methodology **39**

4.1 Genetic Algorithm -NSGA-II 40

4.2 Propeller Design Methodology 41

4.3 PMSM Design Methodology 48

4.3.1 Time-Dependent Simulation 50

4.3.2 Thermal Analysis 51

5 MPS Detailed Design **53**

5.1 Detailed Motor Design 54

5.1.1 First Iteration 55

5.1.2 Final Motor Iteration 57

5.1.3 Efficiency Map 59

5.1.4 Choosing Winding Characteristics 60

5.1.5 Thermal Simulation 60

5.2 Detailed CRP Design 61

5.2.1 Iterations 63

5.2.2 Cavitation Results 66

5.2.3 Structural Analysis 67

5.2.4 CFD Analysis 68

5.3 MPS Mechanical Design 72

5.3.1 Rotor and Stator Assembly 72

5.3.2 Splined Shaft 75

5.3.3 Bearing Selection 76

5.3.4 Sealing 77

6 Conclusions **78**

6.1 Future Work 80

Bibliography **81**

A Detailed Boat Angle Calculations **89**

B Detailed Press Fit Calculations **91**

C SKF seal datasheet **92**

List of Figures

1.1 SR03 during tests on Montargil dam reservoir. 3
1.2 Evolution of propulsion columns of the last three solar prototypes. 3

2.1 Overall dimensions of SG01. 10
2.2 Power train schematic of SG01, with one motor and one controller per propeller, and hydrogen power system. 10
2.3 3D render of the proposed drive train with a section cut. 11
2.4 Bottum Up vs Top Down design approaches, based on [9]. 12
2.5 Main types of electric motors, based on [10]. 13
2.6 Ideal characteristic of a synchronous motor, according to [11]. 15
2.7 Common topologies of PM rotors, taken from [15]. (a) SPM topology, (b) IPM topology, (c) SPM topology 16
2.8 Propeller arrangements behind the hull 21
2.9 Acelerating ducted propeller (a). Decelerating ducted propeller (b), taken from [29]. 21
2.10 The Kongsberg Kamewa Controllable Pitch Propeller system diagram, taken from [30] . . 22
2.11 Spitfire XIV prototype JF321 with contra-rotating propellers, taken from [31]. 23
2.12 Representation of a CRP system using the actuator disc theory, taken from [32]. 24
2.13 Contra-rotating propeller of the SR03 prototype. 24

3.1 Rendered image of the free-surface simulation of SG01. 29
3.2 Fitted curve for CFD data points for SG01's hull resistance. 30
3.3 Diagram of relevant forces acting on SG01. 30
3.4 Representation of total drag of hydrofoil system versus velocity, taken from [38] 32
3.5 Coefficient of form drag in function of Re and AoA 32
3.6 Interference drag coefficient of wing and strut section; with and without fillets, taken from [36]. 33
3.7 Drag coefficients of cylindrical bodies in axial flow, with blunt shape and with rounded or streamlined head forms - as a function of length ratio l/d, taken from [42] 35

3.8 Lift and drag profile for SG01. 36

4.1 Design algorithm process for the electric motor. 40
4.2 Induced velocities example from OpenProp. 42
4.3 Inflow angles example from OpenProp. 43
4.4 Expanded blade contour. 43
4.5 Blade section angles and force diagram, adapted from [3] 44
4.6 OpenProp CRP routine overview. 46
4.7 Visualisation of sheet, tip and hub cavitation, taken from [50]. 47
4.8 Visual representation of the motor design variables, taken from [14] 48
4.9 Synchronous machine equivalent circuit considering core-losses on a d-q reference frame, taken from [14]. 49

5.1 Pareto curve from the first optimisation. Population size 150, at generation 222, selected solution in red. 55
5.2 Geometry of solution 148 of the population at generation 222. 56
5.3 Time-dependent torque result of solution 148. 56
5.4 Pareto curve from the first optimisation. Population size 150, at generation 500. Selected Solution in red. 57
5.5 Geometry of solution 132 of the population at generation 500. 58
5.6 Optimised cut rotor geometry. 58
5.7 Torque ripple before and after the adapted solution. 58
5.8 Predicted efficiency map of the motor, the points represent the simulated data from which the map is interpolated. 59
5.9 Heat transfer coefficient for the forced convection along the motor. 60
5.10 Temperature distribution inside the motor. 61
5.11 Thrust demand curve intersection with propeller K_T open water curve. 63
5.12 Propeller geometry output of solution 4 generated by OpenProp. 64
5.13 Propeller open-water graph of solution 4 generated by OpenProp. In the top left corner is the forward propeller, in the top right corner is the rear propeller and at the bottom is the combined graph for the CRP. Vertical dotted lines indicate the cruise advance coefficient. 65
5.14 Cavitation map of the propellers at takeoff condition. 66
5.15 Cavitation map of the propellers at cruise condition. 67
5.16 Blade stress of the propellers at take condition. 67
5.17 Computational domain and boundary conditions. 68
5.18 Propeller mesh with close up. 69

5.19 Residual evolution for simulation after 12000 iterations. 70
5.20 Integral values over time. 71
5.21 Results of mean propeller force coefficients comparison including CFD results in dashed lines with circle markers, and OpenProp results with and without drag coefficient correction. 71
5.22 Final rotor geometry of the electric motors. 73
5.23 Magnet bridge of rotor. 73
5.24 3D render of the front and rear shaft splines. 75
5.25 3D render of the rear propeller hub. 76
5.26 Locations of selected bearings. 76

List of Tables

2.1 Soft magnetic material properties for use in motor cores. Taken from [16–18]. 17
2.2 Properties of the materials for the PMs. Taken from [22–24]. 18
2.3 Properties of the materials for the shaft. Taken from [27]. 19
2.4 Properties of common materials used in ship propellers, taken from [33]. 25

3.1 Simulation results from CFD for SG01. 29
3.2 Requirements for the CRP prototype. 37
3.3 Requirements for the motor prototype. 37
3.4 Electric motor design constraints. 38

4.1 Thermal properties of materials used in the thermal simulation. 51

5.1 Design variables for the electric motor. 54
5.2 Variable and objective results for individual 132/150. 57
5.3 Performance of adapted solution. 59
5.4 Design variables for the CRP system. 62
5.5 Solution data for takeoff condition. 63
5.6 Solution data for cruise condition. 63
5.7 Mesh size data and mesh quality data. 69
5.8 Shrink fit interferences, temperature deltas and maximum allowable torque results. 75
5.9 Geometry data and factor of safety results for the Spline sizing. 75
5.10 Bearing selection size data and load limits. 77

Acronyms

2D Two Dimensional

3D Three Dimensional

AC Alternating Current

AoA Angle of Attack

AR Aspect Ratio

CFD Computer Fluid Dynamics

CRP Contra-Rotating Propellers

DC Direct Current

FEA Finite Element Analysis

FEM Finite Element Method

GA Genetic Algorithm

IST Instituto Superior Técnico

ITTC International Towing Tank Conference

MEBC Monaco Energy Boat Challange

MPS Marine Propulsion System

NSGA-II Non-Sorting Genetic Algorithm - II

NSPSM Non-Salient-Pole Synchronous Machines

PM Permanent Magnet

PMSM Permanent Magnet Synchronous Motor

RANS Reynolds Averaged Navier-Stokes

RMS Root Mean Square

SG01 São Gabriel 01

SMPM Surface Mounted Permanent Magnet

SPM Spoke Permanent Magnet

SPSM Salient-Pole Synchronous Machines

SR03 São Rafael 03

TSB Técnico Solar Boat

1

Introduction

Introduction

Since ancient times, humans have used waterways such as rivers, seas and oceans as primary means of transport. Protecting these natural resources and the marine environment has become paramount in recent decades. The maritime transport industry contributed 13.5 % of all greenhouse gas emissions from transport in the EU in 2020 and has contributed to the fact that underwater noise levels in EU waters have more than doubled between 2014 and 2019, according to the European Environment Agency [1]. In the recreational sector, fuel prices have also increased the demand for electric-powered boats. Companies such as Candela, Silent-Yachts, Sunreef Eco and some Portuguese-owned companies such as Sun Concept and FaroBoats already produce electric and solar-powered boats. With the development of hydrogen fuel cells in recent years, the possibility of hydrogen-powered boats is on the horizon. One such boat, the Energy Observer, is a hydrogen-powered, zero-emission vessel designed to be self-sufficient in energy. Energy Observer explores and develops solutions for alternate energy production methods [2].

With the electrification of marine transportation, the design of new propulsion systems needs to be developed and studied further. The whole transmission system must be analysed to ensure optimal efficiency leading to usable ranges. High efficiency may be the leading design goal, but several other factors, such as vibration, noise and cavitation behaviour must be considered.

This thesis concerns itself with the design and optimisation of the propulsion system for the hydrogen-electric boat São Gabriel 01 (SG01) developed by the TSB team. The SG01 is the future vessel for the TSB team to use in global competitions. The main competition that the team participates in is the Monaco Energy Boat Challange (MEBC), an international competition where engineering students from various universities compete with self-built electric boats.

In the past, the TSB team competed with four prototypes, three being solar-powered and one hydrogen-powered. Figure 1.1 shows the São Rafael 03 (SR03) prototype, which competed for three consecutive years in the solar A class from 2021 to 2023, garnering various prizes. The SG01 prototype will compete in a different class, the Open Sea Class, where boats of more significant dimensions compete and perform longer offshore routes.

Figure 1.1: SR03 during tests on Montargil dam reservoir.

In the past, the propulsion systems for the solar boat prototypes from TSB followed a similar design approach: the electric motors were mounted inside the vessel and connected to the propeller system through a bevel gear transmission. Figure 1.2 shows the evolution of the propulsion systems of the last three solar boat prototypes. These propulsion columns, as they are called inside the team, evolved in complexity as they started to include more features and more advanced systems. The SR03's propulsion column was the first to include a contra-rotating propeller system entirely designed by the team.

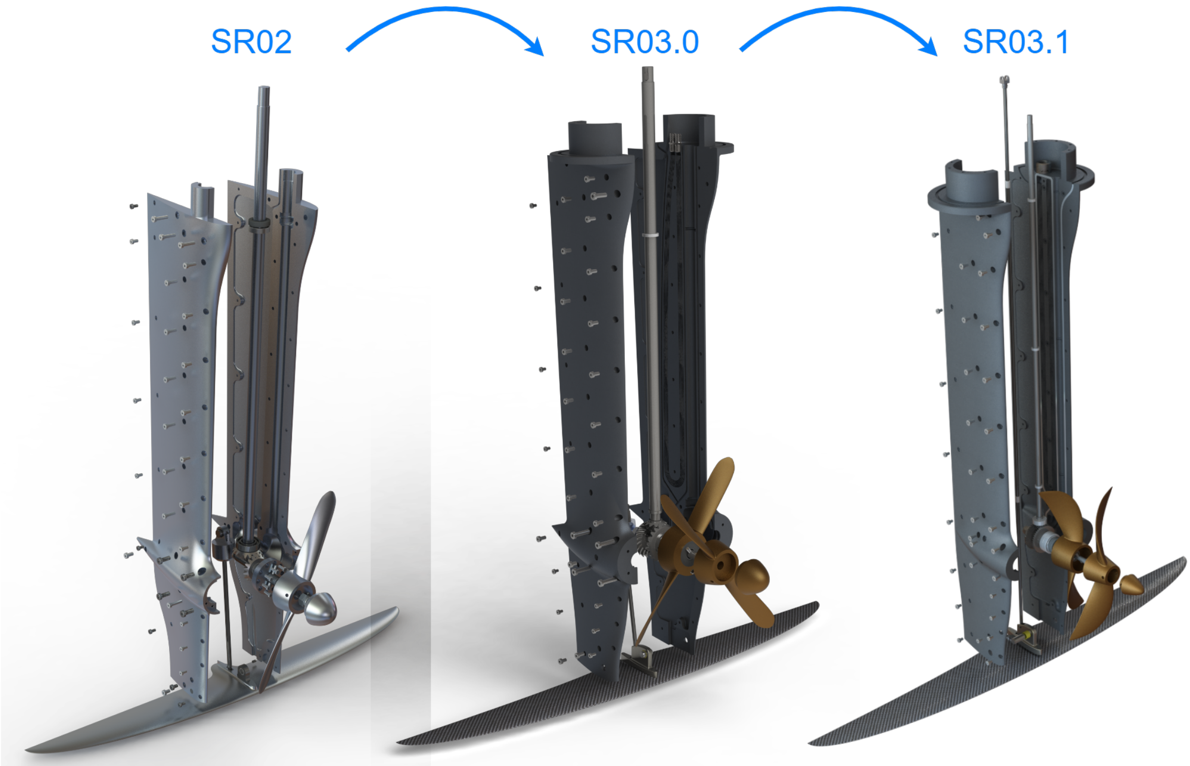

Figure 1.2: Evolution of propulsion columns of the last three solar prototypes.

In the past, the electric motors used in the vessels were all commercially obtained as they were still relatively affordable and suitable for our application. The electrical system architecture was based on a $48\,\mathrm{V}$ electrical system. This new prototype would be based on a $400\,\mathrm{V}$ system, bringing new challenges to finding an appropriate drive motor. The propellers need to be sized accordingly.

The main tasks to be completed are: the design of the motor prototype, the design of the propeller system, the optimisation of the complete system and finally, the construction of a 3D model ready for production.

A theoretical background is given for the design of marine propellers and an overview of the motor's main components, including the most common electric motor types. Special emphasis is applied to Permanent Magnet Synchronous Motor (PMSM), the solution adopted for the MPS in this work.

1.1 Objectives and Goals of the Dissertation

Since the creation of TSB, the team strived to develop their own propulsion system, using commercially available motors coupled to custom gear trains and custom propellers designed by team members. This approach worked well for the smaller solar class of the competition (where boat size is limited to $6\,\mathrm{m}$ by the competition rules and motor power required is between 5 and $15\,\mathrm{kW}$), but for boats of the size of SG01 there start to be a few limitations. For example, PMSM with power around $50\,\mathrm{kW}$ are commercially available. However, since the boat uses hydrofoils, the drive shaft necessary to connect the inboard motor to the propellers would be excessively long and heavy.

In order to reduce complexity and improve efficiency by removing moving parts, the proposed solution is a pod propulsion system where the motor is connected directly to the propeller of the boat.

The team has designed simple propellers for the first two solar prototypes. Later, developed in-house code for developing contra-rotating propellers with improved efficiency and better acceleration properties than simple propellers. A contra-rotating propeller system is also proposed for the SG01.

The proposed objectives of this thesis are the following:

- To present and review the literature on PMSM and marine propeller design;
- To design and optimise the geometry for the PMSM, given the performance requirements of the desired maximum power, nominal speed and maximum torque, respectively: $50\,\mathrm{kW}$, $2500\,\mathrm{RPM}$, $105\,\mathrm{N}\cdot\mathrm{m}$. The optimisation will use an evolutionary algorithm coupled to a Finite Element Analysis (FEA) program. The optimisation objectives will be the minimisation of weight and the maximisation of efficiency;
- To design a CRP set given the propulsion requirements of the vessel using a custom version of Openprop [1].

[1] OpenProp is free software for the design and analysis of marine propellers and horizontal-axis turbines developed by Dartmouth College. This software is coded as a suite of MATLAB m-files [3].

1.2 Thesis Outline

The present dissertation comprises six chapters. Following this introduction, Chapter 2 presents the main technologies that are available for electric motors and the most relevant propulsion systems that exist. Material and design choices are presented and discussed.

In Chapter 3 the design parameters were explored, starting with the development of an analytical static model to predict the resistance characteristics of the boat while flying on top of the hydrofoils, taking into account various hydrodynamical phenomena. The design parameters and constraints for the electric motor and propeller system are also presented and discussed.

Chapter 4 focuses on the design methodology and methods used for the design and optimisation process. Using the Non-Sorting Genetic Algorithm - II (NSGA-II) and coupling it to the analytical and numerical methods presented. In the same chapter, solutions for a variety of different problems can be found.

Chapter 5 presents the obtained solutions of the optimisation process and delves deeper into the necessary changes needed to implement the obtained geometry into the final system. Electromagnetic, thermal and hydrodynamical simulations were developed to evaluate the performance of the solutions to verify the results.

Finally, Chapter 6 compares the achieved system with the objectives that were set at the beginning, detailing all the problems and achievements experienced throughout this master thesis. A final section with some future work is also described in this chapter.

2

Technical Overview

Technical Overview

This study concerns itself with the propulsion system's design for the SG01 prototype. Designing and selecting a marine propulsion system is a complex process that must balance several factors. The propulsion system is divided into two main components: the CRP and the PMSM. The design process of both components was divided into three distinct phases:

- Concept design;
- Preliminary design;
- Detailed design.

This chapter presents the principal methodologies and approaches for electric motor design and marine propellers. Also, an overview of the main components and types of electric motors as well as the main types of marine propulsors is presented. Particular emphasis is given to PMSM and CRP, the solutions adopted for the SG01 prototype.

2.1 Electric Race Boat

Electric boats have a long history since their humble beginnings in the 19^{th} century with the development of the first actual electric motor by Moritz Hermann Jacobi in 1834 [4]. The first electric boat in 1839 was powered by an improved version of Moritz's motor [5]. Performance was limited by the technology of the time, but through countless innovations in electric motors, energy storage and propulsor design, the electric boats of today rival boats powered by internal combustion engines in performance and range. Furthermore, being silent and environmentally friendly, these boats appeal to consumer and tourist markets.

The MEBC is an international challenge open to the public, which welcomes students and professionals from all over the world to race in three different classes: Energy, Solar and Open Sea class. The event aims to create a platform where open-source information sharing is the focus, creating a bridge between the engineers of tomorrow and the industry leaders of today [6]. The Open Sea Class is opened to the following boats:

1. Boats propelled by alternative energies must be less than twelve meters.
2. Boats with the following standard:
    (a) CE[1] certified boats (or equivalent national standard), built to Category C standards (Inshore), with appropriate paperwork.
    (b) Non-certified boats built to Category C standards (Inshore) must be checked by the technical inspection team.
3. Boats capable of carrying at least three persons.
4. Boats carrying the standard boat safety equipment.
5. Boats carrying a marine Very High Frequency when outside of the harbour walls.

The competitions revolve around three main trials: the manoeuvrability, the endurance and the $16\,\mathrm{Nm}$ speed trial. Since the endurance trial and the $16\,\mathrm{Nm}$ speed trial are in a straight line, the efficiency at cruise speed and the time to achieve cruise speed and top speed are the most critical factors. So acceleration is also essential, but only second to steady state efficiency and power.

Throttle response, system reliability and ride comfort are all important considerations since, in order to complete the long endurance trails, all three are needed.

Ride comfort is an interesting design requirement as it involves a fine-tuned propulsion system that is not plagued with excessive vibrations, mechanical noise or rough handling.

In recent years, the development of electric boats has led to several technological improvements, including hydrofoils, which are explained in detail later in this chapter, the adoption of hydrogen fuel cells, and the constant improvement of battery technology. TSB already has a history of designing electric race boats that implement these technologies, and SG01 is a big step to scale these up to a level that would be commercially viable.

2.1.1 SG01 Prototype

The vessel under study is the newest prototype developed by TSB, named SG01. This prototype is designed to compete in the MEBC under the open sea class. SG01 will be a non-certified boat with a length of $8\,\mathrm{m}$, a beam of $2.4\,\mathrm{m}$, a depth of $2.4\,\mathrm{m}$ and a draught of $1.2\,\mathrm{m}$.

[1] CE marking indicates that a product has been assessed by the manufacturer and deemed to meet EU safety, health and environmental protection requirements. It is required for products manufactured anywhere in the world that are then marketed in the EU [7]

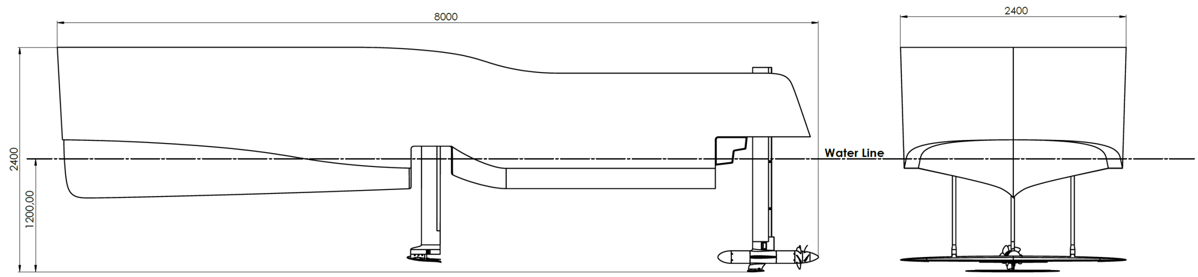

Figure 2.1: Overall dimensions of SG01.

The vessel will use hydrofoils as shown in Figure 2.1. Hydrofoils are lifting surfaces that operate underwater and generate a lifting force that helps lift the vessel's hull out of the water, reducing the total resistance and allowing for higher speeds and more efficient use of energy once the cruise speed is reached. The winglike structures are mounted on the underside of the hull using struts. Struts are streamlined support structures that also house the control systems for the hydrofoil actuation and cooling inlets. The hydrofoil configuration chosen for this prototype was a conventional, non-split, fully submerged configuration [8]. The front hydrofoil has a span of $2.4\,\mathrm{m}$ and takes care of the overall lift and roll stability with the help of two ailerons that are electronically actuated. The rear hydrofoil takes care of the pitch control of the boat during flight. The hull was designed as a planning hull in order to help the boat take off at around $14\,\mathrm{kn}$. In addition, planning hulls are designed to rise and skim on top of the water, reducing power requirements at the design speed.

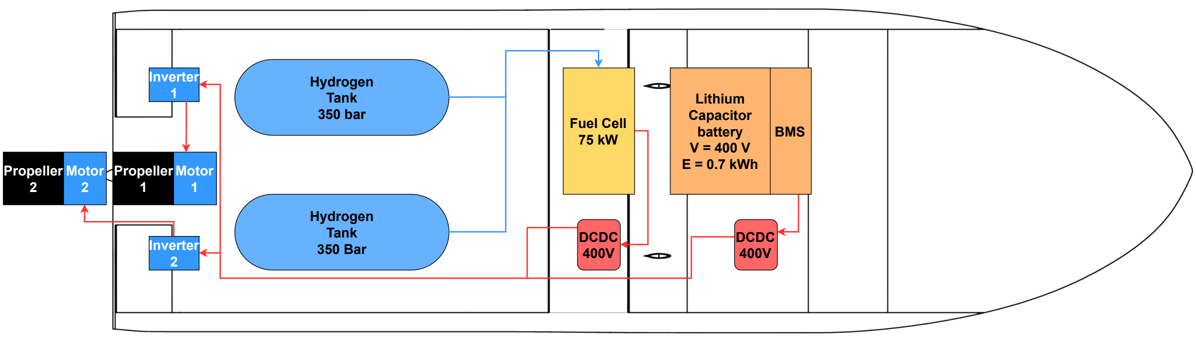

Figure 2.2: Power train schematic of SG01, with one motor and one controller per propeller, and hydrogen power system.

Figure 2.2 presents the powertrain schematic for SG01. It comprises two electric motors, each directly coupled to one propeller of the CRP system. Each motor is controlled by one inverter. The inverters are connected to the fuel cell and the lithium capacitor battery. The system nominal voltage is $400\,\mathrm{V}$ since the power requirement of the vessel is high and lower voltages would result in excessive currents that lead to high losses.

The inverters are responsible for converting the Direct Current (DC) of the fuel cell and battery to Alternating Current (AC) used to power the motors. The pilot sets the desired motor Rotation per Minute using the throttle which is then converted to the necessary current and voltage input by a pulse width modulation control for the motor.

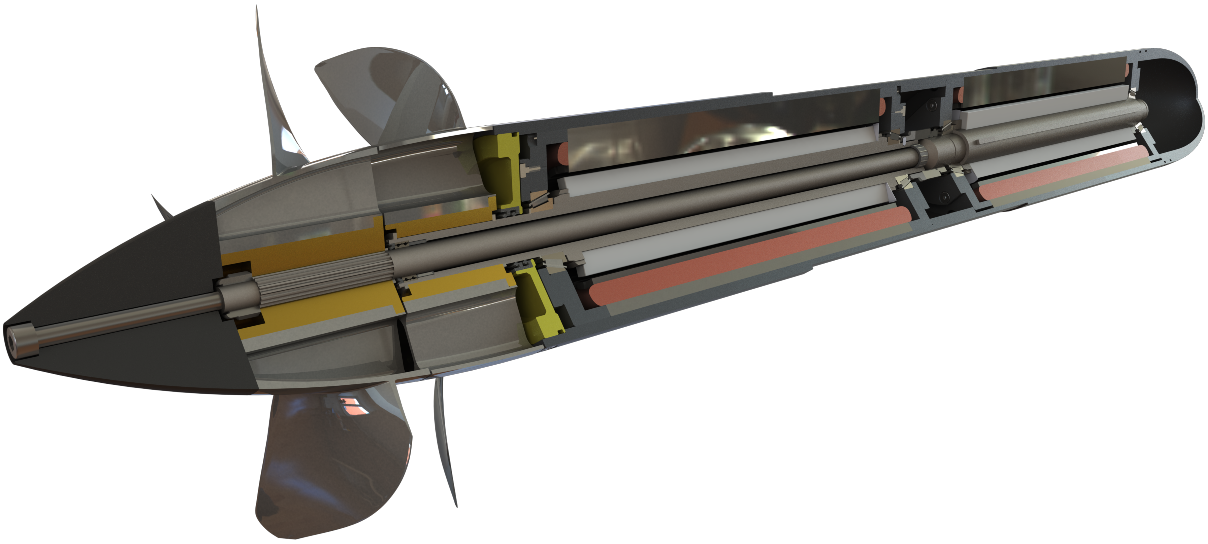

Figure 2.3: 3D render of the proposed drive train with a section cut.

Figure 2.3 shows a 3D model of the drive train, highlighting the direct drive of each propeller. Since the motors are positioned in line with the propellers and are part of the boat's hydrodynamic package, some constraints to the motor were set, for example, the weight and the outer diameter. These constraints will be further analysed in Chapter 3.

2.2 Electric Machine Design and Approaches

The design of an electric machine involves many variables and conflicting objectives, so different physical models must be considered, such as: electromagnetic, thermal, mechanical and electronic. Electric machine development includes defining the design requirements and operating conditions and requires selecting materials, manufacturing the prototype, and testing. Two approaches are possible: i) top-down design and ii) bottom-up design. The two approaches are detailed in Figure 2.4 according to [9]. In the first approach, top-down design, the development of the motor is carried out by working in parallel with the different physical principles systematically. This is only possible when the knowledge of the overall system is established. The problem is solved by optimising the overall multi-physics system, requiring a high knowledge of boundaries and inter-relations.

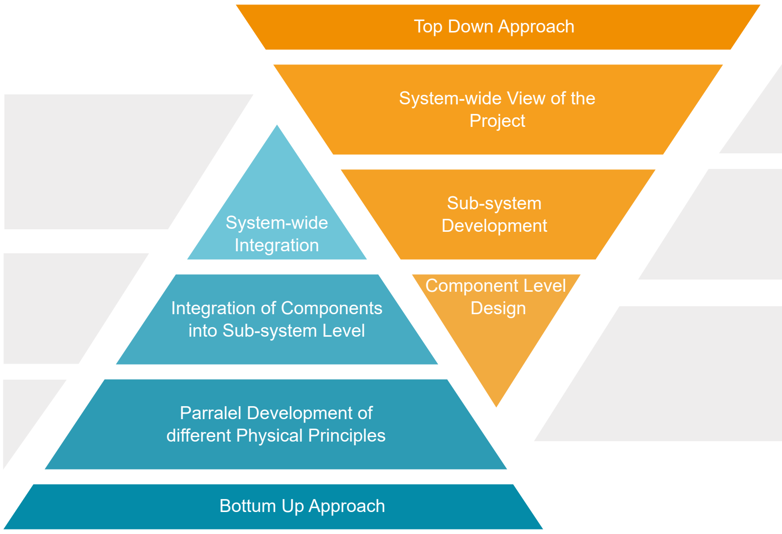

Figure 2.4: Bottum Up vs Top Down design approaches, based on [9].

In the second approach, bottom-up design, the development of the electric machine is carried out by initially working at the component level followed by integration on the overall system. This approach can be easier and faster to implement whilst the overall system knowledge is not needed for those working outside their expertise areas.

The bottom-up approach was chosen for this thesis as it is the first electric motor developed by TSB, and knowledge in this area is lacking for a proper top-down design approach. Furthermore, iteration is a crucial part of the design process of an electric machine, the beginning of the project is always filled with many iterations as knowledge is gathered, and some iterations are made later in the project timeline as specific components are optimised by coupling two or more physical principles.

2.2.1 Electric Motor Components

The main components of an electric motor are the shaft, motor housing, stator core, coils and rotor. All these components will be studied in this thesis.

First, the motor shaft transmits torque to an external load, specifically, in this instance, the propeller. During operation, this constituent experiences a combination of mechanical forces such as tension, compression, bending, and torsion. Consequently, shafts are typically engineered to exhibit optimal stiffness, rigidity, and minimal deflection, thereby ensuring that the stresses and strains imposed on the shaft remain within permissible thresholds under diverse loading and operational circumstances.

The motor housing comprises covers responsible for guaranteeing the motor's structure and protecting its components from the external environment. This is a significant consideration for this case as the motors will be wholly submerged in seawater. Even with a waterproof casing, corrosion can still occur with time as the seals wear out and moisture gets in.

The stator core serves as the immobile element that securely houses the windings within its surface slots. The windings assume the crucial role of generating a revolving magnetic field through alternating currents. Typically, the stator is constructed using multiple laminated sections of electrical steel, thereby mitigating the formation of eddy currents [9].

The rotor is the rotating component that accommodates the Permanent Magnet (PM) (in the case of a PMSM) and follows the rotating magnetic field produced by the stator winding, producing mechanical power. It can either be the outer piece or the inner relative to the stator, depending if the motor is an inrunner or outrunner. The motor considered for this thesis will be an inrunner as the motors are mounted in a pod configuration and to minimise occupied volume the motor housing will be mounted solid to the stator and the rest of the structure that connects it to the vessel. An outrunner motor must have additional space to allow for the rotor to spin freely, complicating the mechanical fixture of the motor to the housing.

2.2.2 Types of Electrical Machines

The performance of a hydrofoiling boat depends on lightweight and compact solutions for its propulsion system. Figure 2.5 presents the different options of electric machines, where two main categories are found: DC motors (with brushed and brushless solutions) and AC motors (with inductions and synchronous variants) [10].

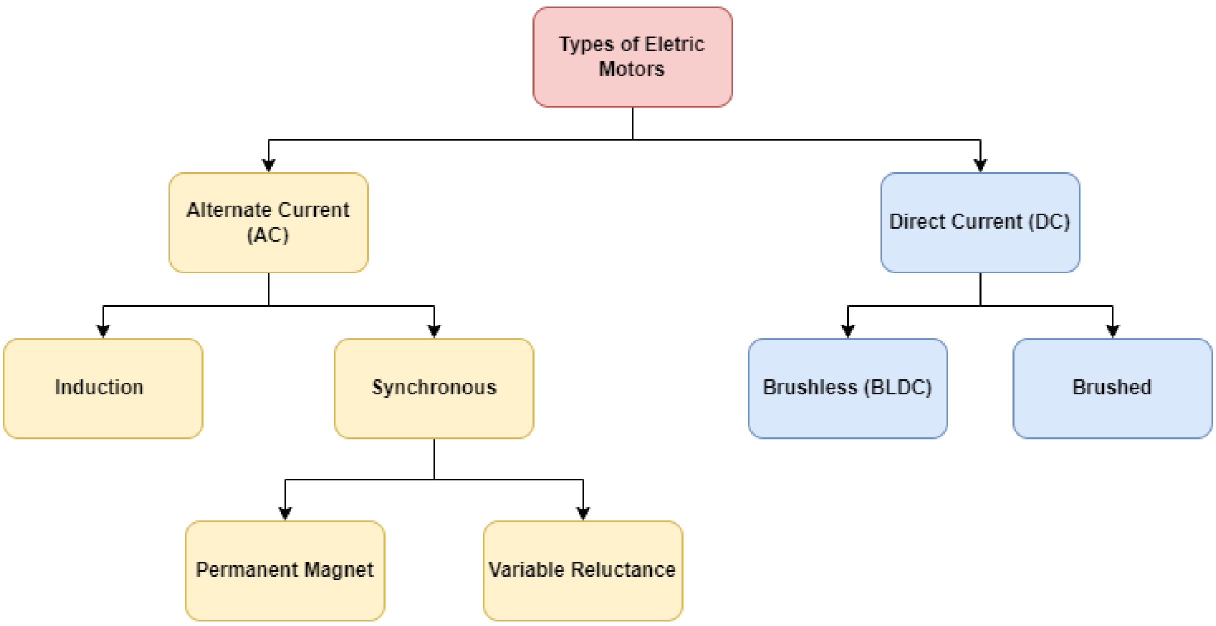

Figure 2.5: Main types of electric motors, based on [10].

The decision to implement a synchronous motor considered its main advantages and disadvantages. However, these motors are more expensive nowadays because of the PM. They are also more sensitive to high temperatures and mechanical vibrations since the PM can be partially or fully demagnetised with the increase of temperature or as a result of crack formation, which leads to decreasing the available motor power and an unbalanced magnetomotive force. On the other hand, they present undeniable advantages, such as high torque to weight and power-to-weight ratios. In general, PMSM are more energy efficient and possess faster dynamical response times than other options.

PMSM eliminate the need for mechanical brushes, thus having longer service life than typical DC motors. Reduced joule losses compared to induction motors, as well as reduced time constants make this option the most suitable for the application.

2.2.3 Synchronous Machine Overview

Synchronous machines operate as other types of electric motors by using a rotating magnetic field, in this case, generated by the armature currents. These are synchronous with the rotor magnetic field. Therefore, the rotor field will align with the stator field just like two bar magnets would if placed near each other [10]. This magnetic field can either be produced by PM, these motors are known as PMSM, or by DC flowing through the rotor windings also described as field windings, known as Salient-Pole Synchronous Machines (SPSM) or Non-Salient-Pole Synchronous Machines (NSPSM) [10].

The rotor field of a SPSM or NSPSM can be adjusted by changing the current flowing through the field windings enabling high efficiencies. NSPSM are used for high-speed operations due to their robust construction and smaller diameter. They also have better dynamic responses than SPSM due to their lower moment of inertia. The optimisation routine developed by the Energy Laboratory focused exclusively on the PMSM motors and thus was a contributing factor to the choice made. Compounding the fact that to supply the DC to the field windings a complex mechanical assembly known as a slip-ring assembly is necessary, occupying precious volume and increasing the risk of mechanical failure.

As previously stated, the magnetic field of a PMSM is generated by the PM. This eliminates the need for rotor coils and other supply mechanisms, thus making these motors mechanically simple. However, the PM poses other constraints, such as temperature and cost. Rare earth magnets with high remanence are expensive and can not endure high temperatures before losing their magnetic properties. As the motor in question will be applied to a race boat, the cost is not the highest priority, and submerging in water helps maintain the temperatures reasonably.

The rotation of the rotor is made possible by two main forces: the Lorentz force and the reluctance force. The Lorentz force combines the magnetic and electric forces on a point charge due to electromagnetic fields. The principle states that a point charge is subjected to a force when moving with a given velocity through an electric and magnetic field. From this principle, the Laplace force is defined as the magnetic force produced by a current flowing through a wire. This is the case when a current is flowing through the windings of the stator: it creates an electromagnet. As the current decreases in one winding and increases in the next, it produces an apparent rotation in the magnetic field. The magnetic field of the PM is attracted to the rotating field, thus producing mechanical rotation and torque.

The reluctant force typically contributes equally to the torque that rotates the rotor. It is created by forming non-permanent electromagnets in the ferromagnetic part of the rotor. Thus the rotating magnetic field attracts both the permanent magnet and the iron rotor. The characteristics of an ideal synchronous motor are shown in Figure 2.6, where the ideal power and voltage increase linearly with motor speed or frequency while the torque is constant. At the base speed, the back electromotive force voltage that is induced in the stator coils by the rotation of the rotor is the same as the voltage fed to the motor by the inverter. When this occurs, no current flows through the motor, and speed can only be increased via the reduction of the rotor magnetic field. This is a method known as field-weakening. At the base speed, power reaches its maximum, and as speed increases, power is kept constant while torque is reduced.

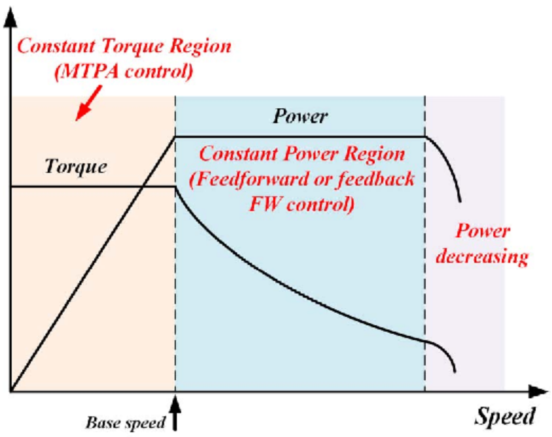

Figure 2.6: Ideal characteristic of a synchronous motor, according to [11].

The speed of a synchronous motor is limited by the inverter voltage supply and the back electromotive force characteristics; the rotor's structural integrity can sometimes limit it due to centripetal forces. In addition, thermal constraints set the torque limit as higher torque requires more current; therefore, higher losses occur, and temperatures increase.

Rotor Geometry

The rotor in a PMSM houses the PM and transmits the torque to the load. The PM can be arranged in various topologies. The two main ones are Surface Mounted Permanent Magnet (SMPM), Spoke Permanent Magnet (SPM) and Interior Permanent Magnet machines.

SMPM motors, represented in Figure 2.7 c), require less complex rotor designs and are simple in construction but may require more complex curved magnets to follow the rotor curvature. Furthermore, the PM are exposed to demagnetisation due to the reverse magnetic fields applied to the rotor magnets by the stator currents in the magnetic air-gap. In the case of inrunner motors, the PM are also subjected to centripetal forces that can cause the separation of the magnet from the rotor surface at higher speeds.

The main strength of an SPM motor, represented in Figure 2.7 a), is the possibility of concentrating the magnetic flux generated by the PM in the rotor achieving higher air gap flux densities, which is beneficial for increasing the electromagnetic motor torque, also having better protection against demagnetisation and mechanical vibrations.

In order to reduce the cost, the possibility of using rectangular magnets and mounting them while already having a magnetic remnant field narrowed the options down. Since previous works had already been developed for optimising the aforementioned topology in [12–14] the SPM topology was chosen.

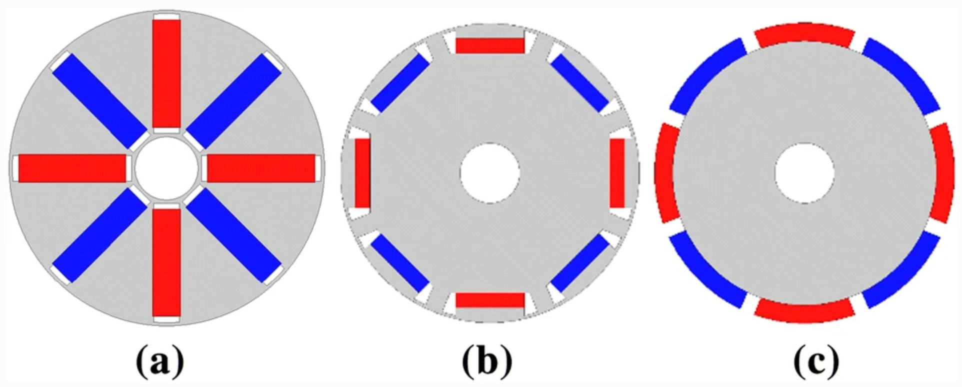

Figure 2.7: Common topologies of PM rotors, taken from [15].
(a) SPM topology, (b) IPM topology, (c) SPM topology

Although this topology has many advantages, magnet bridges must be avoided to prevent the flux from moving inside the rotor from one magnetic pole to another, decreasing the air-gap flux and torque generation. Furthermore, the shaft must be made of a non-ferromagnetic material to prevent a large portion of flux generated by the PM from leaking through it.

Motor Materials

Three factors limit the performance of the motor:

- Saturation of the magnetic field, limiting torque;
- Quality of execution of construction;
- Cooling solution and material choice that limit maximum continuous power.

The saturation of the magnetic core is highly dependent on the geometry chosen for the motor and magnetic material selection. The geometry can be made to avoid areas where saturation can appear during the design phase with the help of optimisation algorithms. The materials are chosen for the core, the PMs, the shaft, the housing, motor windings and the insulation. The shaft and rotor materials were chosen to withstand the high torque requirements set out in the mechanical project.

The motor performance is highly dependent on the capability to manage the heat produced by the different types of losses. The cooling for the motors in the MPS designed in this thesis is achieved by the water flowing around the housing of the motors as the whole system is part of the rudder of SG01. On the other hand, the capability of the PMs and copper windings to resist higher temperatures enables the motor to operate at a higher continuous torque (without saturation) and power.

Core Materials

The core material is what the stator and rotor are made from. Soft magnetic materials are defined as materials that do not retain a magnetic field but are easy to magnetise and demagnetise. They also have a low remnant magnetisation, a small area enclosed by the hysteresis loop (low losses), low coercivity and high initial permeability. The main characteristics to consider for selecting the core materials are the saturation point, the permeability, the specific losses and the density. The saturation point and permeability affect the maximum torque that the motor can produce. The specific losses directly affect the overall efficiency. Finally, the density has a significant impact since the rotor and the stator are the most voluminous parts of the motor.

The stator and rotor are made from thin sheets of core material stacked together in order to reduce losses from Foucault currents (eddy currents). The thinner the magnetic sheets are, the lower the current amplitude and losses will be since the currents in the rotational axis produced by the magnetic flux density moving in the perpendicular axis face a higher resistive path.

Table 2.1 shows the relevant material properties for selecting soft magnetic materials.

Table 2.1: Soft magnetic material properties for use in motor cores. Taken from [16–18].

Characteristics\Materials	M250-35A	NO15	Hiperco50
Magnetic Saturation [T] at $10\,kA/m$	1.7	1.8	2.29
End of linear zone [T]	1.2-1.5	1.2-1.5	1.9-2.1
Losses at 50 Hz with 1T [W/kg]	1.05	1.08	1.01
Losses at 400 Hz with 1.4T [W/kg]	24.1	12.1	10
Ultimate Tensile Strength [MPa]	585	450	930
Density [kg/m^3]	7600	7650	8110

The NO15 core material was selected as it offers good magnetic saturation values and lower losses than the M$250-35$A. Previous works also used this material so previous experiences help with its application [13].

Permanent Magnet

A PM can produce a magnetic field in an air gap without field excitation winding and electric power dissipation. External energy is involved only in changing the energy of the magnetic field, not in maintaining it. As with any other ferromagnetic material, a PM can be described by its B|H hysteresis loop. The delay of a magnetic material known commonly as Magnetic Hysteresis, relates to the magnetisation properties of a material by which it first becomes magnetised and then de-magnetised according to [19]. PMs are also called hard magnetic materials, meaning ferromagnetic materials with a wide hysteresis loop [20].

By having a wide hysteresis loop PMs have high losses and adding that they can not withstand high temperatures without losing their magnetic properties (Curie temperature), selecting the appropriate material becomes paramount. A list of possible PMs is shown in Table 2.2. The Curie temperature is lower than the temperature at which the material loses its mechanical properties. Since PMs have high losses and are mounted in the rotor, which is difficult to cool, the operating temperature should not exceed the Curie temperature.

There are three types of PMs currently used for electric motors: [21]

- Alnicos (Al, Ni, Co, Fe);
- Ceramics (ferrites) e.g., barium ferrite $BaFe_{12}O_{19}$ and strontium ferrite $SrFe_{12}O_{19}$;
- Rare-earth materials, i.e., samarium-cobalt $SmCo$ and neodymium-ironboron $NdFeB$.

Table 2.2: Properties of the materials for the PMs. Taken from [22–24].

Characteristics\Materials	Alnico	SmCo	NdFeB
Remanence [T]	0.55-1.08	0.87-1.19	1.075-1.49
Coercivity [$\mathrm{kA\,m^{-1}}$]	44-147	1040-2400	875-2388
Energy product $(\mathbf{BH})_{\mathbf{max}}$ [$\mathrm{kJ\,m^{-3}}$]	11.1-39.8	135-265	227-430
Maximum Curie Temperature [$^{\circ}\mathrm{C}$]	538	250-350	60-100
Saturation H [$\mathrm{kA\,m^{-1}}$]	176-735	600-880	716-923
Density [$\mathrm{kg\,m^{-3}}$]	7000	8400	7600

The selected motor's magnet material was Neodymium Iron Boron ($NdFeB$), as it enables the highest performance and provides the highest energy product and remnant magnetic field. It has a lower Curie temperature than the alternatives, such as samarium cobalt ($SmCo$), often used in motor applications [25], but considering that the motor will be submerged, cooling will not be a significant concern.

In a marine environment, the corrosion of magnets is a major concern, so a protective layer of protective film should be applied to the magnet to protect it from the elements. There are three main ways to achieve this: phosphorization, electroplating and electrophoresis [26]. Phosphorization is a process through chemical and electrochemical reactions to form a phosphate chemical transformation film. Electroplating is the process of plating a thin layer of other metals or alloys on the surface of some metals by electrolysis. Electrophoresis consists of charged particles moving towards electrodes opposite to their electrical properties under the action of electric fields.

Shaft Material

The shaft is the mechanical link from the motor to the load. In this case, it is mechanically coupled to the propeller. Therefore, the shaft must withstand the high torque the motor produces during takeoff. Furthermore, the shaft material, in the case of spoke geometry, must be non-ferromagnetic, as pointed out before. As the shaft is quite long, the torsional stiffness must be considered. So, the material chosen was a non-magnetic material with high tensile strength and low losses.

Table 2.3 shows the properties of the non-magnetic materials suitable for a shaft in this application.

Table 2.3: Properties of the materials for the shaft. Taken from [27].

Characteristics\Materials	Aluminium 7075	Stainless steel AISI 316	Titanium Grade 5
Density [$\mathrm{kg\,m^{-3}}$]	2810	8000	4430
Yield Tensile Strength [MPa]	503	290	880
Ultimate Tensile Strength [MPa]	572	580	950
Electrical Resistivity [$\mathrm{\mu\Omega\,cm}$]	5.15	75	178
Thermal Conductivity [$\mathrm{W\,m^{-1}\,K^{-1}}$]	130	16.2	6.7
Magnetic Relative Permeability	1.000022	1.0008	1.00005

Since TSB has a stainless steel sponsorship, 316L stainless steel was chosen as the primary material for the motor shaft. While also providing an adequate balance between tensile strength and stiffness.

2.3 Marine Propeller Design and Approaches

Ship propellers have a relatively simple function, to turn the rotating motion from the engine into thrust to propel the vessel through the water. The first modern ship propellers were patented in 1836 by Francis Pettit Smith after several years of experiments and in 1839 the first successful screw-propelled steamship was built using Smith's design, the SS Archimedes [28]. To design and operate a ship, it's essential to estimate the propulsive power accurately. Knowing the power helps determine the size and weight of the engines, estimate fuel consumption, and predict operating costs. While evaluating ship resistance and propulsion is not an exact science, it requires a combination of empirical, analytical and numerical models. In this thesis a combination of these models is used to determine the ship resistance and numerical methods are used to calculate the propulsive power and efficiency of the propellers.

A summary and comparison of the numerous propulsor types is presented. Subsequently, a more detailed description of the selected propulsion type is given, scrutinizing its theoretical basis. Lastly, an examination of the material and manufacturing techniques relevant to the chosen propulsor type is conducted, ensuring a comprehensive and informed decision-making process.

2.3.1 Types of Propulsors

The general mechanism for thrust generation is the change of fluid linear momentum through a device called the propulsor. By Newton's third law, the fluid exerts a thrust force on the propulsor as a reaction to the propulsor imparting a change of its linear momentum. The kinetic energy of the fluid increases as a byproduct and is left in the wake of the propulsor, this energy is not used for propulsion, so, it represents a loss of energy.

There are many different propulsor types in existence with a variety of benefits and drawbacks, either hydrodynamically, in terms of efficiency and cavitation properties, or other considerations like structural integrity, reliability, manufacturing and cost. Most of the unconventional types of propulsor lie outside the scope of this work and will therefore not be considered.

Conventional Propellers

The screw propeller is widely used around the world and is the most common propulsor used in the marine industry. With helicoidal blades that are placed around a round hub, the screw propeller takes advantage of the properties of lifting surfaces, as the blade sections operate like hydrofoils set at an angle of attack relative to the incoming flow. Both the lift and the drag forces produced by the blades contribute to the thrust and resistive torque of the propeller. The blade shape is therefore critical for optimising the efficiency and reducing cavitation as will be discussed in section 4.2.

In general, these propellers are installed at the aft of the ship. The reason is that it improves overall propulsive efficiency, by means of recovering part of the kinetic energy spent in the generation of hull boundary layers. Figure 2.8 illustrates a few arrangements for single screw systems most commonly used in commercially available vessels.

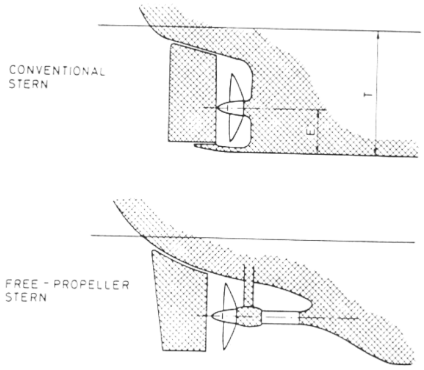

Figure 2.8: Propeller arrangements behind the hull

Each propeller must be matched to the driving machinery and the operating conditions it will face. Although this type of propulsor is efficient, there is wasted energy in the form of rotational and kinetical energy in the wake that limits the maximum efficiency of the screw propeller.

This propulsor type, while mechanically simple to implement into a drive system, has a crucial disadvantage if implemented in SG01: by relying on one screw propeller for all the necessary thrust, the loading on that propeller will be high and all the torque needed will have to be generated by a single electric motor compromising the design of the electric machine.

Ducted Propellers

A ducted propeller system is described as a propeller that operates inside a duct (or nozzle). This duct is shaped like a ring airfoil. There are two types of ducts: the accelerating and the decelerating duct. Their working principles are illustrated in Figure 2.9.

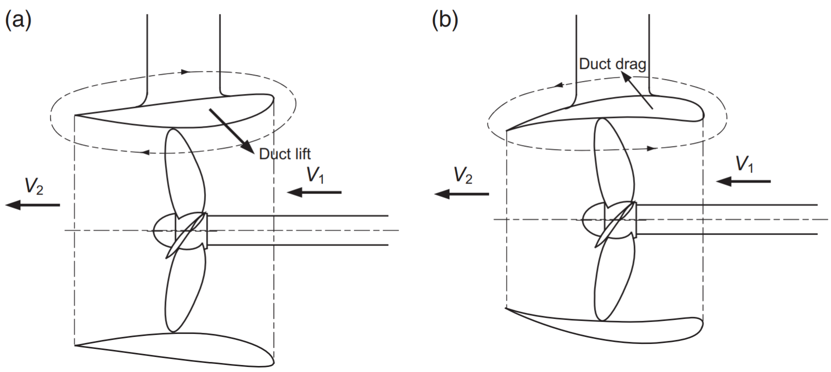

Figure 2.9: Acelerating ducted propeller (a). Decelerating ducted propeller (b), taken from [29].

In the accelerating duct case, due to Bernoulli's law, the inside pressure is reduced with regard to the outside surface. This reduction in pressure enables the duct to deliver a thrust force that adds to the propeller's thrust, increasing efficiency in the case of heavily loaded propellers. However, it negatively impacts efficiency for not-so-heavily loaded propellers as the added drag from the duct counteracts the thrust it generates. Therefore, this duct type is reserved for use in trawlers and tugs.

In the case of decelerating ducts, the pressure increases on the inside of the duct as the flow decelerates, helping reduce the susceptibility of cavitation onset. However, the propeller's efficiency decreases since the forces acting on the duct are opposite to the thrust, increasing overall drag. Therefore, this duct type is reserved for use in navy vessels where stealth is paramount or marine exploring vessels where disturbances to marine environments are to be minimised.

Controllable Pitch Propellers

Controllable pitch propellers, as their name indicates, allow the pitch of the blades to be adjusted. As thrust is generated by the relative angle of attack of the blades to the incoming flow, by changing the propeller's pitch, thrust can be adjusted without changing the propeller's rotational speed. This brings a significant advantage to combustion engines that operate more efficiently at their nominal speed while also providing better manoeuvrability since the engine can be kept at full power, and by inverting the propeller pitch, the vessel is put into "reverse".

The main downside of this propulsor type is the added mechanical complexity of the mechanism needed to control the rotation of each blade, making the miniaturisation of these systems extremely difficult for application in small racing and commercial vessels. A diagram of such a system is presented in Figure 2.10.

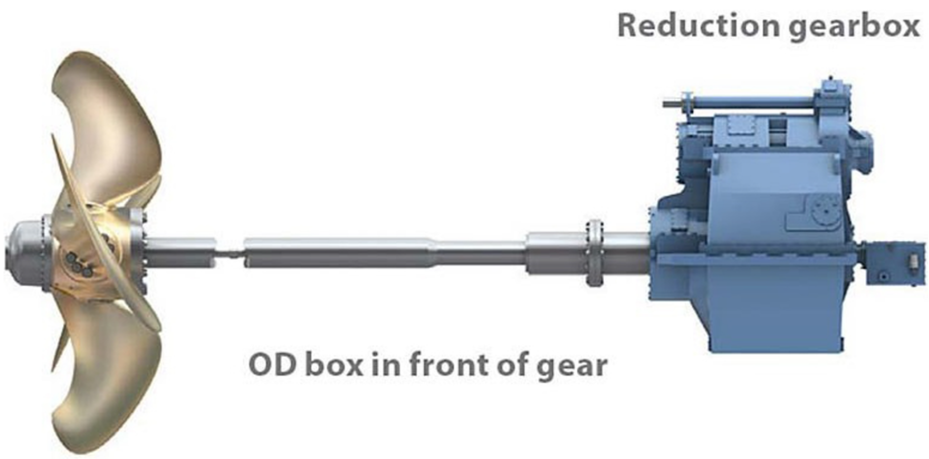

Figure 2.10: The Kongsberg Kamewa Controllable Pitch Propeller system diagram, taken from [30]

Contra-Rotating Propellers

The Contra-Rotating Propellers (CRP) system was first implemented in the aeronautical sector during the rapid development of wartime aviation and used in the iconic Spitfire Mk XIV depicted in figure 2.11. A set of contra-rotating propellers consists of two propellers mounted on coaxial shafts and rotating in opposite directions.

Figure 2.11: Spitfire XIV prototype JF321 with contra-rotating propellers, taken from [31].

The power and thrust are divided between the two propellers. The second propeller rotates in the opposite direction and captures the rotational energy of the forward propeller, thus increasing the overall efficiency. The following section provides an overview of the theory behind the design of a CRP system.

2.3.2 Contra-Rotating Propeller Overview

The chosen propulsion system is the CRP due to its capability to provide higher efficiencies and the possibility of distributing the power between two equally sized electric motors, this helps with reducing each motor's size. The added complexity of a contra-rotating system is avoided due to the possibility of coupling each electric motor to one of the propellers keeping the overall bill of materials to a minimum. The vertical strut connecting the pod to the vessel will also serve as the rudder.

The design of a CRP system is based on methods developed for single-screw propellers, be it the lifting line theory, blade element theory, or computational fluid dynamics. The design of the upstream propeller is generally done as if it were a single propeller. In contrast, the downstream propeller is designed considering the induced velocities generated by the upstream blades. The propeller system is mounted at the end of the aft strut, having a considerable distance from the hull. Thus the interaction of the hull on the wakefield may be neglected.

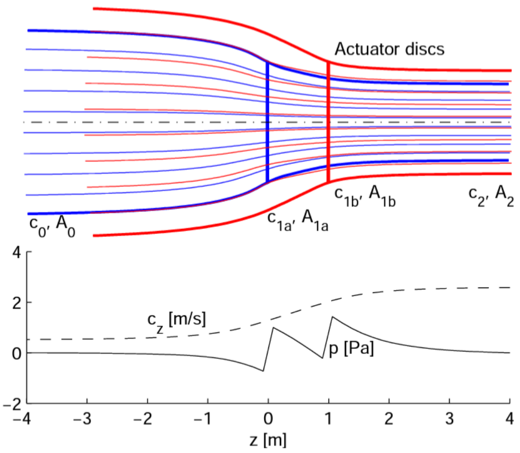

Figure 2.12: Representation of a CRP system using the actuator disc theory, taken from [32].

In this work to design the propellers, a modified version of the open-source software from Dartmouth College, *Openprop* is used. *Openprop* consists of a collection of *Matlab* scripts that will be explained in detail in section 4.2.

The inputs necessary for the process are the vessel's resistance or the required thrust, the desired rotational speed of the propellers, the number of blades, and their geometry. As each propeller is mounted to an electric motor, a thrust distribution of 50 : 50 for the forward and aft propellers has been studied. Only one electric motor design has to be made with this configuration, simplifying the project.

Figure 2.13: Contra-rotating propeller of the SR03 prototype.

A GA is used to optimize the propeller chord, thickness, and diameter by considering different optimization goals. This approach is detailed in Chapter 3. The objective of this design was to obtain an $80\,\%$ efficiency for the cruise speed of $20\,\mathrm{kn}$ while not having a combined torque of over $200\,\mathrm{Nm}$ at the takeoff condition.

2.3.3 Propeller Materials and Manufacturing Considerations

The requirements of a propeller material are many and vary with the size of the propeller and the type of vessel. It must be capable of being cast into a complex shape held to close tolerances; it must be strong and tough and resist corrosion and erosion. During its lifetime, almost every propeller is damaged in one way or another and requires to be repaired. Therefore, good weldability without adverse side effects is desirable for a propeller material.

The manufacturing process chosen for the CRP system is 5-axis computer numerical control manufacturing. This process was chosen due to the low number of examples being produced, namely one of each propeller, the possibility of achieving tight tolerances of the blade geometry, and the availability of machine shops sponsoring the project that already have experience machining previous propellers, such as the ones depicted in figure 2.13.

There is a wide variety of stainless steels, but one of the most common for propellers is $13\,\%$ chromium martensitic steel which depends on its properties on heat treatment. The austenitic $18\,\%$ chromium $8\,\%$ nickel steel has also been used in service, but more usually for freshwater applications. The duplex ferritic austenitic stainless steel has been developed more recently and the experience of this steel is limited. All these steels have high elastic modulus. The martensitic and duplex steels both have high proof stress and tensile strength, but the austenitic has lower strength; however, it has very high ductility and impact strength [33].

Table 2.4 lists the mechanical properties of ship propellers' most commonly used metal alloys.

Table 2.4: Properties of common materials used in ship propellers, taken from [33].

Materials\Characteristics	**0.2 % Proof Stress** $[\mathrm{MPa}]$	**Tensile Strength** $[\mathrm{MPa}]$	**Elongation** $[\%]$	**Modulus of elasticity** $[\mathrm{GPa}]$	**Izod Impact Value** $[\mathrm{J\,cm^{-2}}]$	**Brinell Hardness Number**	**Specific gravity**
Manganese Bronze	200	510	28	107	30	145	8.2
Nikalium	270	680	27	124	34	175	7.6
Novoston	305	685	30	117	50	185	7.4
Superston Seventy	345	725	27	117	50	190	7.4
Sonoston	285	565	25	77	50	150	7.1
13 % Chromium Stainless Steel	450	680	20	200	39	220	7.8
Austenitic Stainless Steel	265	565	45	195	115	130	8.0
Low Carbon Steel	250	450	26	200	42	130	7.9
Grey Cast Iron	-	235	-	105	-	200	7.1
Austenitic SG Cast Iron	235	435	42	105	47	150	7.1

Since TSB has a stainless steel sponsorship, 316L stainless steel which is an austenitic stainless steel, was chosen for the primary material of the propellers. While also providing an adequate balance between tensile strength and impact resistance.

3

MPS Design Parameters

MPS Design Parameters

In this chapter, the design parameters of the MPS are covered, for both the electric machine and propeller. In order to start the design, first the design constraints and the vessel resistance need to be specified. Other parts of the boat's system considered relevant for designing the MPS will also be addressed. Design parameters and constraints are summarised which is the objective of the design process.

3.1 Design Parameters

SG01 was designed to be an $8\,\mathrm{m}$ planning hull vessel with a planning speed of around $10\,\mathrm{kn}$ in order to reduce resistance before take-off. As the competition focuses heavily on endurance racing, the efficiency and robustness of the propulsion are crucial. The decision to have two direct-drive propellers reduces the number of failure points, and by eliminating a gearbox, efficiency can be maximised.

Following this, the main design challenge was to define a compact motor solution for the two electric motors constrained by the torque requirements of the propellers designed to produce the necessary thrust to propel the boat forward.

3.1.1 Vessel Resistance Overview

An integral part of the design process of both the PMSM and CRP is the determination of the vessel's resistance. The resistance is what dictates the thrust required by the propellers and, thus, the torque required by the motors.

As the boat possesses hydrofoils, the resistance characteristics were divided between 2 modes, the displacement and the flying mode, as described by the following expression:

$$D_{vessel} = \begin{cases} D_{hull} + D_{FW} + D_{RW} + 3 \cdot D_{strut} + D_{torpedo}, & \text{if } V_{vessel} < V_{takeoff} \\ D_{FW} + D_{RW} + 3 \cdot D_{strut} + D_{torpedo}, & \text{if } V_{vessel} \geq V_{takeoff}, \end{cases} \tag{3.1}$$

where D_{hull} is the hull resistance, D_{FW} and D_{RW} are the drag of the front and aft hydrofoils, D_{strut} is the drag of each of the struts, $D_{torpedo}$ is the drag of the torpedo containing the electric motors. Each of the components will be broken down into their subcomponents in this subchapter.

The hull resistance, D_{hull}, was determined with the use of Computer Fluid Dynamics (CFD) Reynolds Averaged Navier-Stokes (RANS) solver kindly provided by BlueOasis, a Portuguese-based business focused on the use of computational tools to aid the design of boats, yachts and other marine vessels.

With the use of ReFRESCO[1], simulations were performed at various speeds in order to determine the planning speed of the hull and the resistance profile. Figure 3.1 depicts a rendering of one of the simulations.

Figure 3.1: Rendered image of the free-surface simulation of SG01.

The results were compiled in Table 3.1. As speed increases the resistance force does not increase in a quadratic manner due to the effects of the planning hull, furthermore, the trim of the boat (also described as pitch) increases with speed. This relation must be taken into account for the take-off speed estimation as it influences the hydrofoils' angle of attack.

Table 3.1: Simulation results from CFD for SG01.

Speed $[\mathrm{kn}]$	**Speed** $[\mathrm{m\,s^{-1}}]$	**Force** $[\mathrm{N}]$	$\mathbf{F}$	**Force Total X** $[\mathrm{N}]$	**Trim** $[\mathrm{radian}]$	**Trim** $[^\circ]$	**Sinkage CG** $[\mathrm{m}]$
3	1,543	101	0,201	202	0,005	0,281	0,272
5	2,572	358	0,335	716	0,008	0,430	0,282
8	4,115	948	0,536	1896	0,036	2,068	0,307
10	5,144	1247	0,670	2494	0,059	3,358	0,277
12	6,173	1450	0,805	2900	0,055	3,151	-0,003
15	7,716	1524	1,006	3048	0,055	3,151	-0,006
20	10,288	2395	1,341	4790	0,060	3,438	-0,120

A curve fitting was performed in order to estimate resistance values between the simulated points. A 6-degree polynomial fitted the data reasonably well, with an r^2 of $0,9998$, as shown in Figure 3.2. The polynomial is not used to extrapolate the data as it does not follow any physical law and since the vessel is expected to fly above the surface at that speed only interpolated values are used.

[1] ReFRESCO is a multi-phase viscous flow solver focused on maritime applications. Under active development by MARIN experts and multiple partners around the world, ReFRESCO is constantly evolving to better suit the evolving needs of the maritime world [34].

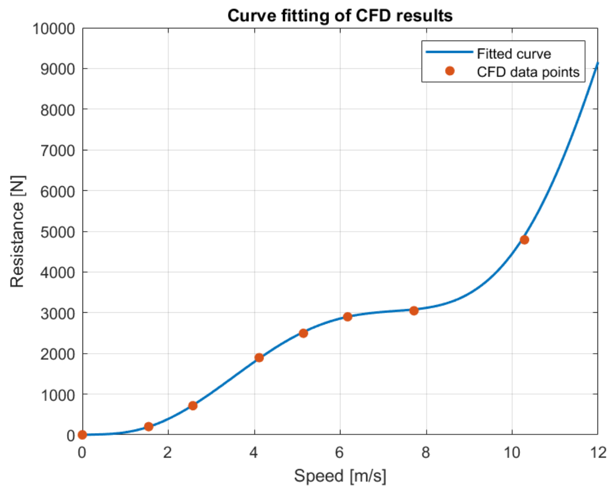

Figure 3.2: Fitted curve for CFD data points for SG01's hull resistance.

For the hydrofoil drag estimation, a custom Matlab code was developed with data from Xfoil[2], empirical equations from Hoerner's Book [36], and theory of the dynamics of flight in order to determine the angle of attack of the hydrofoils.

To better understand the problem at hand Figure 3.3 presents a force diagram of SG01. The front hydrofoil is the main lift generator and the rear hydrofoil serves as a horizontal stabilizer in the configuration.

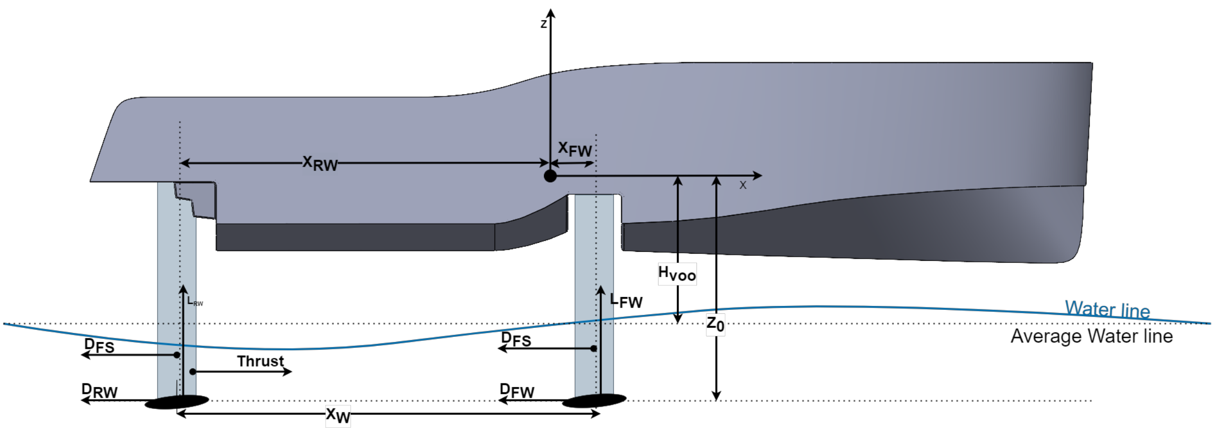

Figure 3.3: Diagram of relevant forces acting on SG01.

A model of the hydrofoil configuration was replicated in XFLR5[3] and the aerodynamical derivatives were extracted and saved to an Excel file, which is then fed into Matlab.

There are two possible states for the boats: flying and non-flying. A simple take-off speed is deter-

[2]Xfoil is an interactive program for the design and analysis of subsonic isolated airfoils developed at MIT [35].
[3]XFLR5 is an analysis tool for airfoils, wings and planes. It utilises Xfoil's direct and inverse analysis capabilities and wing design and analysis based on the lifting line theory, the vortex lattice method, and a 3D panel method [37].

mined at which the hydrofoils generate enough lift to get the hull airborne. For the airborne state, the following stability matrix calculation is performed. This expression is derived from the balance of forces and moments around the centre of mass, assuming that the thrust, drag forces and moments cancel each other out,

$$\begin{bmatrix} 1 & 1 \\ -X_{FW} & X_{RW} \end{bmatrix} = \begin{bmatrix} L_{FW} \\ L_{RW} \end{bmatrix} \cdot \begin{bmatrix} m \cdot g \\ -cm_{FW} \cdot q \cdot S_{FW} \cdot MAC_{FW} \end{bmatrix}, \tag{3.2}$$

where X_{FW} and X_{RW} are the distances from the front and aft hydrofoil to the centre of mass as shown in Figure 3.3. L_{FW} and L_{RW} are the lift forces produced by the front and aft hydrofoils respectively. m is the mass of the vessel, g is the gravitational constant, cm_{FW} is the moment coefficient of the front hydrofoil, S_{FW} is the planform area of the front hydrofoil, MAC_{FW} is the mean aerodynamic chord of the front hydrofoil, and q is the dynamic pressure given by

$$q = \frac{\rho v^2}{2}, \tag{3.3}$$

where ρ is the density of the water v is the velocity. Hydrofoil angles and pitch of the hull are determined using the calculated lift the detailed expression is given in annexe A.

For the non-foiling state the pitch of the vessel is known due to the CFD simulations, the influence of the hydrofoils on the pitch is neglected here in order to simplify calculations. By knowing the pitch of the boat at a given speed the lift of both hydrofoils can be determined.

For both states, the drag of the hydrofoils and vertical struts is determined using the angles and lifts calculated earlier.

The overall drag of a hydrofoil can be divided into the following components:

$$D_{hydrofoil} = D_{ind} + D_{form} + D_{fric} + D_{int} + D_{wave}, \tag{3.4}$$

where D_{ind} is the induced drag, D_{form} the form drag, D_{fric} the friction drag, D_{int} the interference drag and D_{wave} the wave drag. These components do not all follow the same evolution with velocity. As velocity increases the induced drag component decreases and the rest increases as depicted in Figure 3.4.

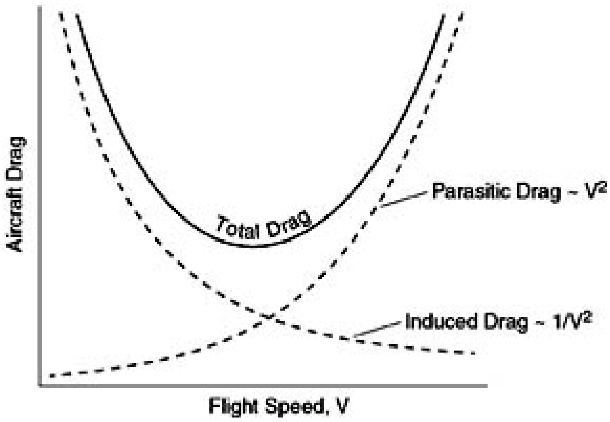

Figure 3.4: Representation of total drag of hydrofoil system versus velocity, taken from [38]

The induced drag, D_{ind}, is the drag due to lift, as the hydrofoil generates a force perpendicular to the cord line the vector can be divided into two components, lift and induced drag. The induced drag coefficient is given by the following expression [39]:

$$C_{D_{ind}} = \frac{CL_{3D}^2}{\pi e AR}. \tag{3.5}$$

In Equation 3.5, e represents the *Oswald* efficiency, for an elliptical wing the efficiency is 1 according to the Lifting Line Theory. Aspect Ratio (AR) is the aspect ratio of the wing given by the ratio of the span to the root chord length. CL_{3D}^2 is the 3D lift coefficient of the hydrofoil under study.

The form drag, D_{form}, is obtained through Xfoil, a matrix of data was collected on the profile of the front hydrofoil and with the curve fitting tool a 3D interpolation was obtained as seen in Figure 3.5.

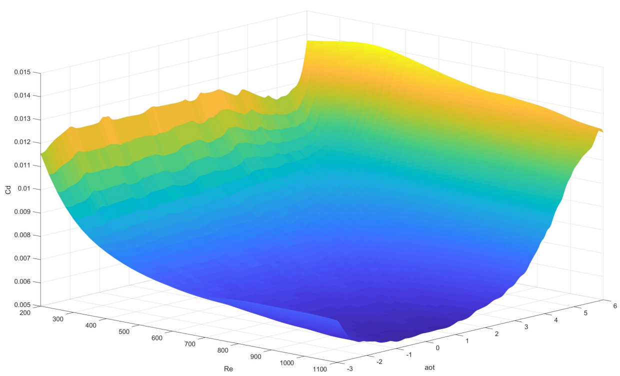

Figure 3.5: Coefficient of form drag in function of Re and AoA

The skin friction drag, D_{fric}, component was determined with the simplified skin friction coefficient of a flat plate using a simple transition model at $Re_{crit} = 5 \cdot 10^5$, Re_{crit} being an approximation of the

Reynolds number at which transition from laminar to turbulent flow occurs [40]. Equation 3.6 determines the position of the transition:

$$X_{crit} = \frac{Re_{crit}\nu}{\rho v}, \tag{3.6}$$

where X_{crit} is the distance from the leading edge to the transition point, ν is the dynamic viscosity of the water. Equation 3.7 represents the skin friction coefficient of the laminar part and Equation 3.8 the turbulent drag coefficients of one side of a flat plate [40, 41]:

$$CD_{lam} = \frac{1,328}{\sqrt{Re_x}}, \tag{3.7}$$

$$CD_{turb} = \frac{0,455}{log_{10}(Re^{2,58})}. \tag{3.8}$$

The interference drag, D_{int}, is given by Hoerner as the added drag generated by the interference between the horizontal hydrofoil and the vertical strut [36]:

$$D_{int} = q \cdot CD_{int}\frac{T_f T_S}{2}, \tag{3.9}$$

where T_f and T_s are the frontal areas of the hydrofoil and the strut respectively. The coefficient of the interference drag can be estimated by:

$$CD_{int} = 17 \cdot t^2 - 0.05, \tag{3.10}$$

where t represents the average thickness of the hydrofoil and the strut, respectively.

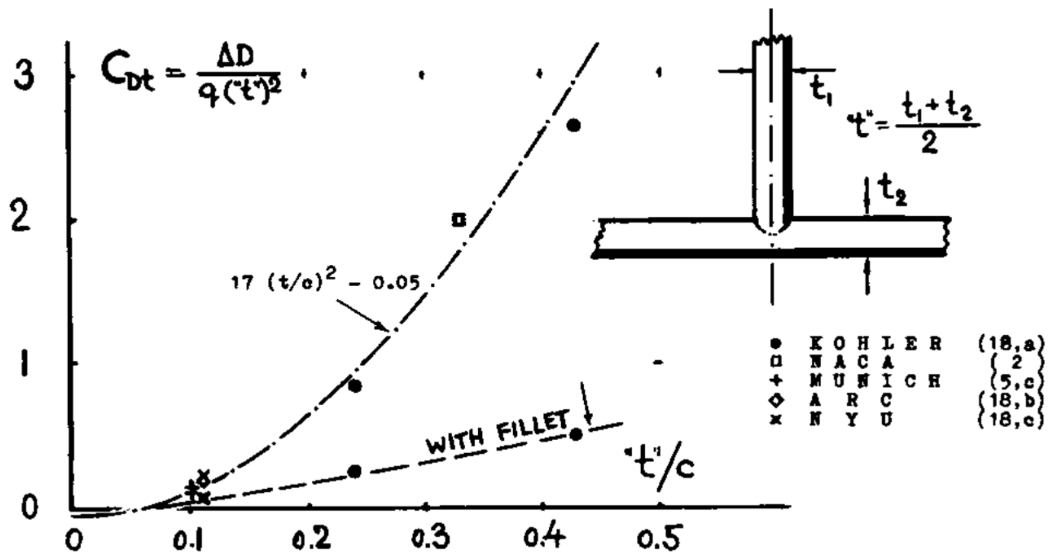

Figure 3.6: Interference drag coefficient of wing and strut section; with and without fillets, taken from [36].

Wave drag, D_{Wave}, is a result of the free surface interaction with the horizontal hydrofoils, as the wing generates lift it deforms the surface and increases drag. The relation is formalised with the use of the Froude number in the following equation for the coefficient of wave drag taken from Hoerner's Fluid Dynamic Drag [41],

$$CD_{wave} = \frac{CL_{ref}^2}{2F^2}, \tag{3.11}$$

this coefficient is used in the wave drag equation:

$$D_{wave} = q \cdot CD_{wave} \cdot h \cdot b. \tag{3.12}$$

In Equation 3.12 the distance to the free surface h and the span of the hydrofoil are given in meters. The lift used for the calculation, CL_{ref}, is the lift produced by the hydrofoil producing the surface wave. The Froude number, F, expressed in the following equation:

$$F = \frac{v}{\sqrt{g \cdot h}}, \tag{3.13}$$

is a dimensionless number which takes into account the speed of the object and its distance to the free surface, it represents the inertia of the moving fluid relative to the influence of the pressure gradient imposed on it.

For the vertical struts, some components of the drag equation are the same as for the hydrofoils. Air resistance is neglected for the portion that is above the surface of the water. The full drag expression is the following:

$$D_{strut} = D_{form} + D_{fric} + D_{spray}. \tag{3.14}$$

The addition of the spray drag is due to the surface-piercing portion of the strut, as it connects to the rest of the boat. The water tends to rise up the surface of the strut and add to the overall drag component, this correlation is defined as:

$$D_{spray} = q \cdot CD_{Spray} \cdot T_S^2, \tag{3.15}$$

where CD_{Spray} equals to 0.24 [41]. The last component that needs to be accounted for is the drag of torpedo-shaped encasing the electric motors given by:

$$D_{torpedo} = q \cdot A \cdot CD_{torpedo}. \tag{3.16}$$

A torpedo coefficient of drag of 0.2 was selected as an estimation based on Figure 3.7 and given a length ratio of $l/d = 800/120 = 6.66$ [42].

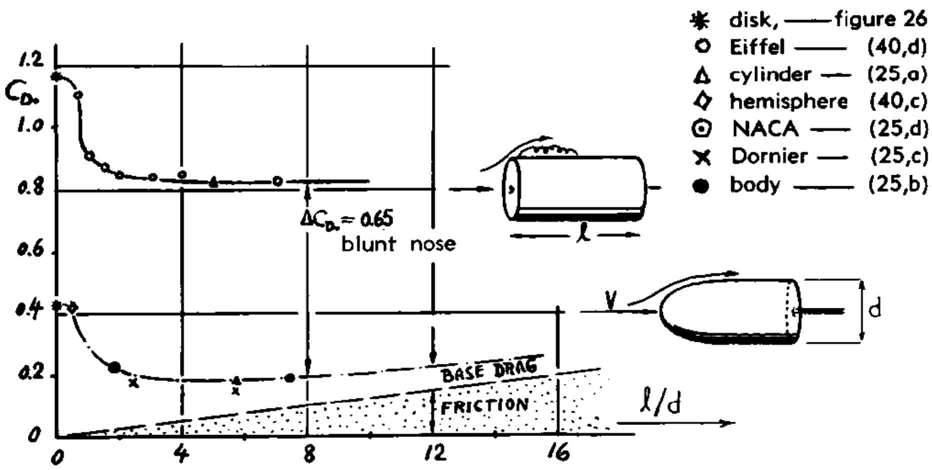

Figure 3.7: Drag coefficients of cylindrical bodies in axial flow, with blunt shape and with rounded or streamlined head forms - as a function of length ratio l/d, taken from [42]

To streamline the calculations a Matlab routine was developed using Equations 3.1 to 3.18. With speed as an input, the geometry and physical constants defined in the code, the routine determines the lift required at the given speed using Equation 3.2. The lift calculated from the matrix operation is converted to the 3D lift coefficient and the following expression approximates the Two Dimensional (2D) lift coefficient of the hydrofoil:

$$CL_{2D} = CL_{3D} * \frac{AR + 2}{AR}, \tag{3.17}$$

this expression is obtained from the lifting line theory, as the AR approaches infinity the 3D coefficient of lift will approach the 2D coefficient. Although a more accurate expression is possible with the Helmbold Equation, the simplified Equation is valid for an AR above four [43].

With the 2D lift coefficient determined, a subroutine is called to determine the Angle of Attack (AoA) of the hydrofoil. This subroutine calls Xfoil from Matlab, loads the correct airfoil geometry and introduces the calculated lift coefficient, receiving as an output the angle of attack of the wing. Since the front hydrofoil is fixed relative to the vessel at a pre-determined angle, the relative AoA to the incoming flow is given by the pitch of the vessel.

The same is repeated for the aft hydrofoil, but this hydrofoil is not fixed so the mechanical AoA is determined by the expression:

$$\alpha_{tailmech} = \alpha_{tail} + \alpha_{wing} * (1 - \epsilon_\alpha) + \epsilon_0 - i_T - Pitch, \tag{3.18}$$

where the expression $\alpha_{wing} * (1 - \epsilon_\alpha)$ gives the downwash produced by the front hydrofoil, while ϵ_0 is the Induced AoA and i_T is the incidence angle of the aft foil, which is zero. α_{tail} is the calculated AoA of the rear wing [43].

The calculated lift coefficients, AoA and geometry data are fed into the drag calculation subroutine which uses the previously discussed equations to determine the drag of the hydrofoil system at any given speed.

The resulting lift and drag curve profiles for the vessel are presented in Figure 3.8.

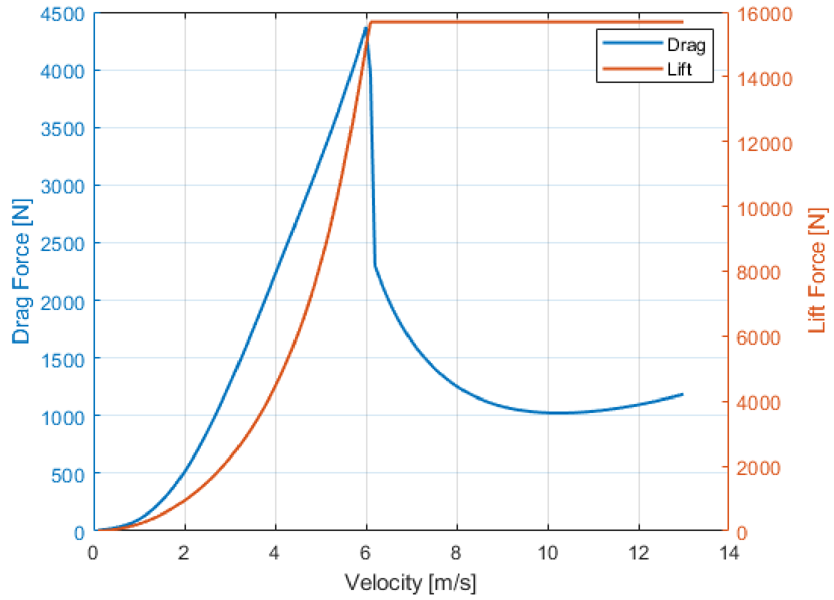

Figure 3.8: Lift and drag profile for SG01.

3.1.2 CRP Design Parameters

The requirements for the CRP were decided by evaluating the most important characteristics needed for a performance hydrofoiling vessel. To achieve the longest possible time hydrofoiling at cruise speed, efficiency needs to be maximised to reduce energy consumption. Another important characteristic is the time to take off since any wasted time not foiling wastes precious energy needed to complete the endurance race. With these two key characteristics in mind, the main design challenge was to define a capable contra-rotating propeller, with the following specific goals taken into account:

- To maximise the efficiency;
- To minimise the torque requirement at take-off.

The design constraints are given by the mechanical resistance of the propeller blades and the cavitation inception, as ride comfort was an important aspect to consider. Analysing the result of the drag profile of the vessel and different electric boats on the market, allowed the definition of the requirements for the CRP prototype (Table 3.2).

Table 3.2: Requirements for the CRP prototype.

Parameter	Value
Cruise speed	$20\,\mathrm{kn}$
Take-off speed	$12\,\mathrm{kn}$
Thrust at cruise speed	$1300\,\mathrm{N}$
Thrust at take-off speed	$4400\,\mathrm{N}$
RPM at cruise speed	2200-2400 $\mathrm{r\,min^{-1}}$
RPM at take-off speed	2200-2400 $\mathrm{r\,min^{-1}}$
Diameter range	230-280 mm
Hub diameter	$<$130 mm
Torque at take-off speed	$<200\,\mathrm{N\,m}$
Efficiency at cruise speed	$>$76 %

3.1.3 Motor Design Parameters

To power the propellers an adequate motor must be designed and thus the guiding principles of the propeller design parameters translate directly to the motor. While the propeller design is dependent on the resistance of the vessel, the motor is dependent on the characteristics of the propeller creating a design loop that will be iterated as the size of the motor will influence the hub size of the propeller. Some characteristics can already be estimated for a first iteration which will then be improved upon once the first iteration of the propeller system is made. Using as the guiding principles the following:

- To maximise the efficiency at cruise speed;
- To minimise, as much as possible, the weight of the motor without compromising the hydrodynamic characteristics of the torpedo shape.

Table 3.3 summarises the general requirements. No commercially available motor had the characteristics that would satisfy the requirements to power the CRP system.

Table 3.3: Requirements for the motor prototype.

Parameter	Value
Maximum power	$50\,\mathrm{kW}$
Maximum torque	$100\,\mathrm{N\,m}$
Maximum weight	$20\,\mathrm{kg}$
Nominal speed	$2300\,\mathrm{r/min}$
Maximum voltage	400 V
Diameter range	100-120 mm
Phases	3

Constraints

The optimisation is constrained in order to achieve viable solutions. The considered constraints are geometrical, thermal, electrical, and magnetic and are presented in Table 3.4. Geometrical constraints ensure that the geometry is realistic and viable; thermal constraints ensure that the thermal limits of the materials in the motor are respected; magnetic constraints limit the use of the ferromagnetic material to its linear zone; electrical constraints ensure that the solution motor can be connected to a realistic inverter.

Table 3.4: Electric motor design constraints.

Constraint type	Constraint	Range	Notes
Geometrical	Stator outer radius	$<60\,\mathrm{mm}$	
	Motor stack length	$=300\,\mathrm{mm}$	
Thermal	Max. temperature	$<120\,°\mathrm{C}$	Because only the stator surface temperature is considered in the optimization model, the PM maximum working temperature is considered a constraint. Corresponds to the maximum temperature at which the considered PM are not permanently demagnetized.
Electrical	Input Apparent Power	$<90\,\mathrm{kV\,A}$	
Magnetic	Magnetic flux density	$1.6\,\mathrm{T}$	
	Demagnetization		Less than 10% of demagnetized PM area.

4

MPS Detailed Design Methodology

MPS Detailed Design Methodology

This chapter covers the computational methodologies used to design the MPS, both the electric machine and propeller. For the electric motor design, an overview of the Matlab routine using the NSGA-II evolutionary algorithm and governing equations coupled to the COMSOL Multiphysics model is given. For the CRP, a detailed description is presented for the governing equations and constraints of the lifting line model applied to a contra-rotating system. The mechanical, electromagnetic and fluid-dynamics analyses and the GA used to optimise both components are presented.

4.1 Genetic Algorithm -NSGA-II

In order to arrive at an optimal solution without manually testing for each possible solution an optimisation algorithm is used. In multivariable problems, the use of nonlinear techniques is a very convenient and economical way to investigate the effects of the tested variables. One of the most famous meta-heuristic multi-objective methods that are widely used for multiobjective optimization of energy systems is the nondominated sorting genetic algorithm known as NSGA-II [44]. In this algorithm, solutions are categorized based on the Pareto concept and sorted into nondominated layers [45].

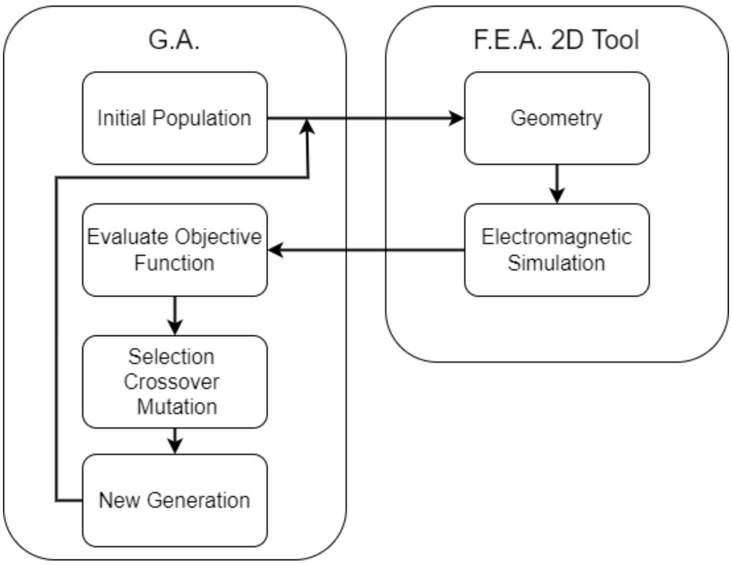

Figure 4.1: Design algorithm process for the electric motor.

Electromagnetic, thermal and mechanical phenomena are strongly interdependent by non-linear relations. The NSGA-II sorting algorithm is strongly suited for this type of problem. The optimisation process is shown in Figure 4.1. The GA works together with a FEA tool to produce the optimum solutions in case of the PMSM case.

The NSGA-II is a multiobjective evolutionary algorithm that takes cues from natural selection, as in evolution. The initial population is randomly created from a constrained space of variables. This set of individuals is evaluated based on an objective function and those selected are permitted to advance to the next generation. These individuals are called parents and are used to create children for the next generation. These children can suffer the following changes to their genome (input variables): i) mutation (random changes to the individual genome), ii) crossover (combination of the genome of two parents, normally the ones with higher ability to continue to the next generation). The main idea of the Pareto NSGA-II is to calculate the Pareto front that corresponds to a set of optimal solutions, so-called nondominated solutions, or also Pareto set [46].

The NSGA-II algorithm has the following advantages compared to other algorithms:

- It can search in a wide range;
- It can handle problems that start with non-feasible solutions;
- Provides a set of good quality solutions;
- It is parameterless.

However, it has some disadvantages such as: if there is a crowded comparison convergence might be restricted and it is a non-dominated sorting of 2N size. The algorithm chosen was developed by previous works with satisfactory results regarding electric motor optimisation [12, 13].

The objective function consists of two output values that are given to the algorithm. These values are going to be minimised by altering the design parameters. In the case of the CRP, the objectives are the negative of the CRP efficiency and the torque required by the system at take-off condition, since the function needs to be minimised. In the case of the PMSM, the values are the negative of the efficiency at cruise condition and the weight of the motor.

4.2 Propeller Design Methodology

The design methodology described in this section leans heavily on the use of OpenProp [3] and propeller design theory [47].

The propeller blade is defined about a line normal to the shaft axis called the propeller reference line. Together with the airfoil shape, pitch, rake and skew the blade of the propeller is defined [48]. In the OpenProp environment, the propeller geometry can be defined by vectors containing the necessary geometry data.

OpenProp is based on the moderately loaded lifting line theory, in which the propeller blade is represented by a lifting line with trailing vorticity aligned to the disturbed flow at the lifting line. The induced velocities are computed using a vortex lattice, with helical trailing vortex filaments shed into the wake at discrete stations along the blade. The blade itself is modelled as discrete sections, having 2D section properties at each radius. Loads on the blade are computed by integrating the load on each section of the blade over the spanwise radial direction [3]. The goal of the propeller optimisation within OpenProp is to determine the optimum circulation distribution along the span of the blade which yields the best performance given the input conditions returning the optimal pitch distribution for the propeller.

The propeller in operation generates a wakefield, this wakefield perturbs the boat's performance given that it interacts with other boat surfaces, like the hull, rudder and hydrofoils. The propeller wake also influences the propeller performance itself, this influence is measured via induced velocities. Induced velocities can be interpreted as a measure of kinetic energy dissipated and not used to generate thrust, hence low induced velocities are desirable. Figure 4.2 depicts an example of induced tangential, u_t, and axial, u_a, velocity profiles shown in red generated by a propeller blade, where the inflow velocity, V_a, is $1\,\mathrm{m\,s^{-1}}$ in solid blue and the tangential velocity, V_t, is zero represented in dashed blue.

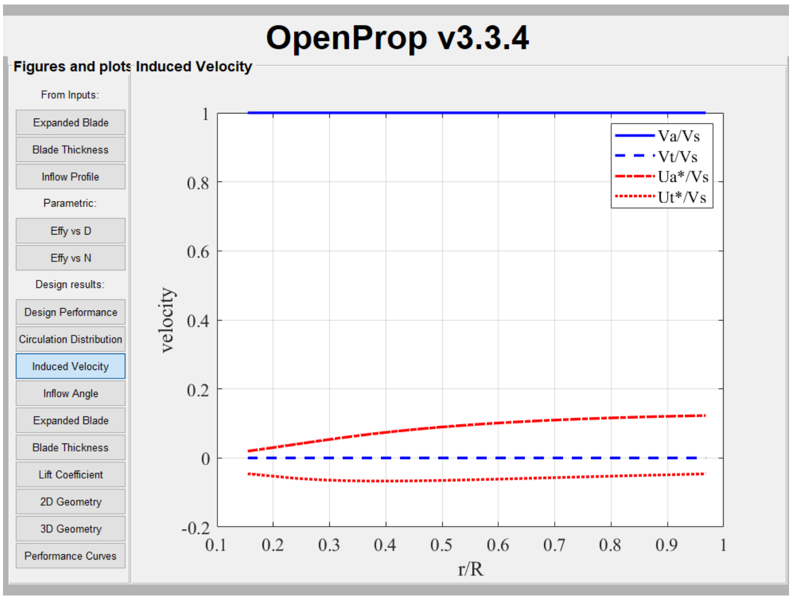

Figure 4.2: Induced velocities example from OpenProp.

In Figure 4.3 the blue line is the pitch angle of the blade sections without taking into consideration the induced velocities, and the red line is the pitch angle taking into consideration the induced velocities. The angles β and β_i are represented in Figure 4.5, note the influence of the induced velocities (u_a and u_t) obtained from Figure 4.2.

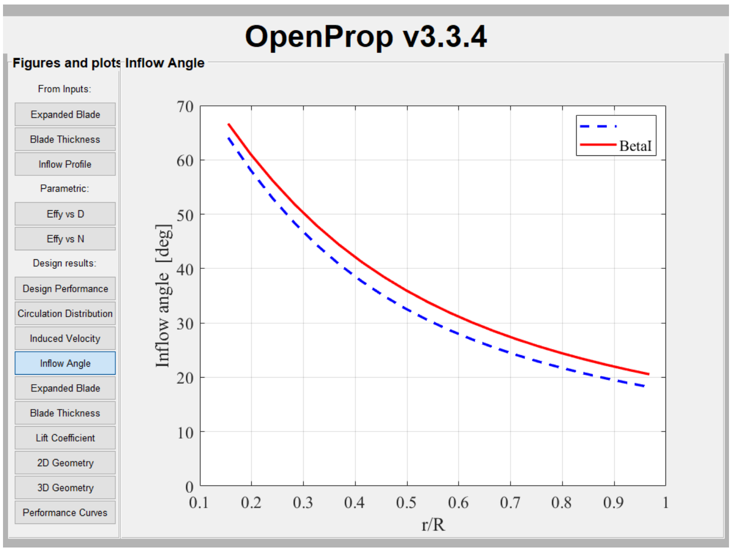

Figure 4.3: Inflow angles example from OpenProp.

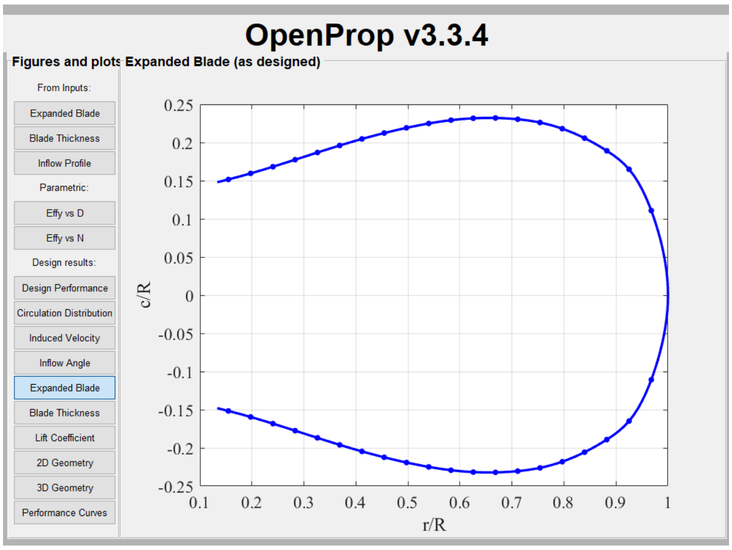

Figure 4.4: Expanded blade contour.

The expanded blade contour is a useful representation of the blade geometry, in other terms the chord is plotted against radius. An example is shown in Figure 4.4.

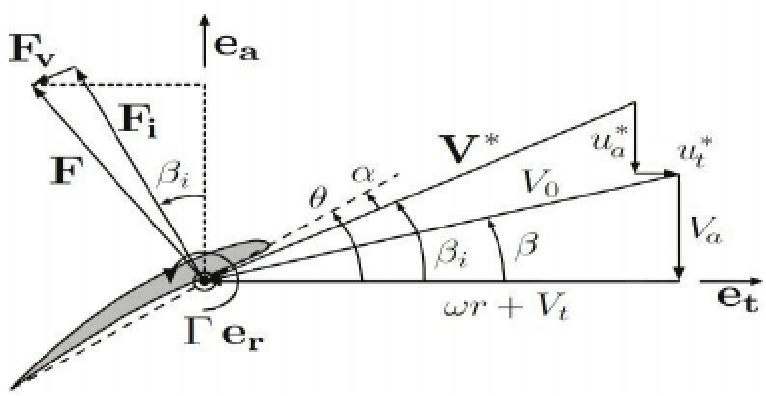

Figure 4.5: Blade section angles and force diagram, adapted from [3]

From Figure 4.5 the relation between the axial and tangential inflow velocities, V_a and V_t and the induced axial, u_a^*, and tangential, u_t^*, velocities is evident. Also shown in Figure 4.5 is the angular velocity of the propeller shaft, ω, such that the apparent tangential inflow to the blade section at radius r is $r\omega$. V_t is assumed to be zero. The total relation is expressed by:

$$V^* = \sqrt{(V_a + u_a^*)^2 + (r\omega - u_t^*)^2}, \tag{4.1}$$

and the pitch angle is given by:

$$\beta_i = tan^{-1}[\frac{V_a + u_a^*}{r\omega - u_t^*}]. \tag{4.2}$$

Also represented in figure 4.5 is the circulation, Γ, the resulting (inviscid) Kutta-Joukowski lift force $F_i = \rho V^* \cdot \Gamma$, the viscous drag force, F_v, aligned with V^* and the resulting force per unit radius. The total force can then be decomposed into axial F_a and tangential F_t components:

$$F_a = F_i cos(\beta_i) - F_v sin(\beta_i), \tag{4.3}$$

$$F_t = F_i sin(\beta_i) + F_v cos(\beta_i), \tag{4.4}$$

where the magnitudes of the inviscid and viscous forces per unit radius are given by Equations 4.5 and 4.6:

$$F_i = \rho V^* \Gamma, \tag{4.5}$$

$$F_v = \frac{1}{2}\rho (V^*)^2 C_D C, \tag{4.6}$$

where C_D is the section profile drag coefficient, which is kept constant per default and C is the chord length of the profile at a given radius.

Assuming the Z blades are identical, the total thrust and torque are given by:

$$T = Z \int_{r_h}^{R} F_a dr = \rho Z \int_{r_h}^{R} [V^* \Gamma cos(\beta_i) - \frac{1}{2}\rho (V^*)^2 C_D C sin(\beta_i)] dr, \tag{4.7}$$

$$Q = Z \int_{r_h}^{R} r\hat{e}_r \times F_t dr = \rho Z \int_{r_h}^{R} [V^* \Gamma sin(\beta_i) + \frac{1}{2}\rho (V^*)^2 C_D C cos(\beta_i)] r dr. \tag{4.8}$$

The efficiency of the system is calculated by the ratio of useful energy produced, $T \cdot V_{\text{inf}}$, and the necessary input power $Q \cdot \omega$:

$$\eta = \frac{T V_{\text{inf}}}{Q \omega}. \tag{4.9}$$

In order to analyse the performance of both propellers the values of thrust and torque need to be adimensionalised. The thrust coefficient is given by the following equation:

$$K_T = \frac{T}{\rho \cdot n^2 \cdot D^4}, \tag{4.10}$$

where T is the generated thrust given in newtons, D is the diameter of the propeller in meters and n is the rotations speed given in rotations per second. The torque coefficient is expressed by:

$$K_Q = \frac{Q}{\rho \cdot n^2 \cdot D^5}, \tag{4.11}$$

which is adimensionalised similarly to the thrust coefficient, only the diameter is raised to the power of five. These adimensionalised values are given in function of the advance ratio of the propeller, a parameter relating the speed of the advance of the ship to the rate of rotation given by:

$$J_s = \frac{V}{n \cdot D}. \tag{4.12}$$

The propeller efficiency can thus be expressed as a function of the thrust and torque coefficients and the advance ratio, expressed by:

$$\eta = \frac{J_s \cdot K_T}{2\pi \cdot K_Q}. \tag{4.13}$$

OpenProp uses a standard propeller vortex lattice model to compute the axial and tangential velocities, u_a^* and u_t^*. By running a first iteration of the forward propeller it is possible to extract these mutually induced velocities, and then compute the global efficiency of the CRP system, with the updated velocity triangle. This approach is based on the Master Thesis of Eyal Kravitz but simplifies it by only simulating the effects of the forward propeller on the aft propeller and not in the opposite direction [49]. This method is less computationally intensive but also less accurate. The flow chart in Figure 4.6 gives an overview of the major computational steps involved in the OpenProp routine.

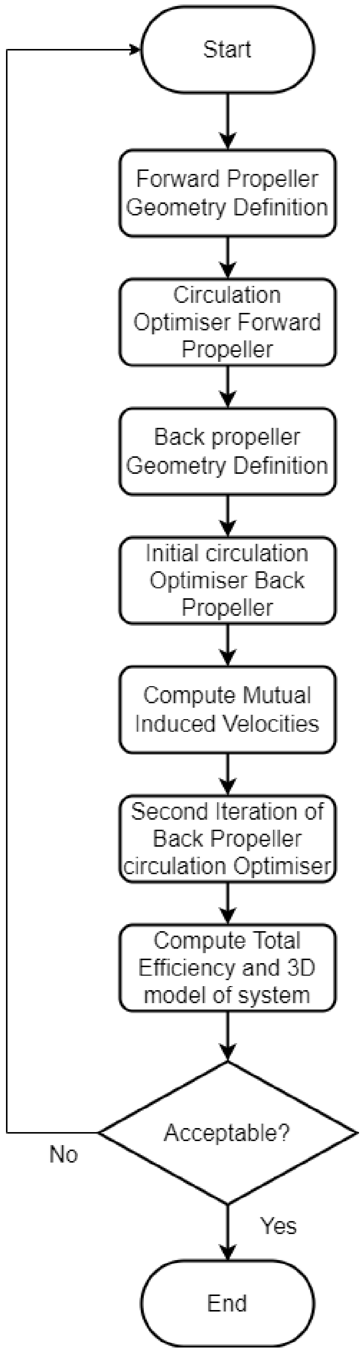

Figure 4.6: OpenProp CRP routine overview.

Cavitation Analysis

Cavitation occurs when the local pressure on the blade surface is below the liquid's vapour pressure, as a consequence vapour bubbles are formed, these bubbles influence the hydrodynamic properties of the propeller, and when they collapse, a small shock wave appears. After a long time exposed to cavitation, the propeller surface is damaged, cavitation also influences propeller noise and vibration.

Overall, cavitation is highly undesirable, except in cases like super-cavitation propellers where the effects of cavitation are used to aid propeller performance. This type of propeller is usually found in racing boats, where high thrust and acceleration are required, but the lifetime of the propeller is small and the damage from the shock waves can be neglected. A visual representation of a cavitating is presented in Figure 4.7.

Figure 4.7: Visualisation of sheet, tip and hub cavitation, taken from [50].

As stated before cavitation occurs when the local pressure on the blade surface is below the liquid's vapour pressure. However, in fluid mechanics, it is common practice to work with non-dimensional numbers and when studying cavitation the most important non-dimensional coefficients are the cavitation number, σ, Equation 4.14, and the pressure coefficient, CP, Equation 4.15 [48]:

$$\sigma = \frac{P\infty - P_v}{0.5 * \rho * V^2}, \tag{4.14}$$

$$CP = \frac{P - P\infty}{0.5 * \rho * V^2}, \tag{4.15}$$

where P_∞ is the static pressure in the free stream, P_v is the liquid vapour and P is the local pressure on the blade. P_∞ depends on the depth of the propeller, water temperature and salinity. The propeller depth is inferior when the boat is on hydrofoils, and this should be the reference depth for the propeller cavitation study, given that this is the critical point. Off-design analysis needs to take this change into account since in the takeoff condition the propeller is submerged at a greater depth than at cruise speed.

These coefficients enable the prediction of the occurrence of cavitation on the blade surface, computing $\frac{-CP}{\sigma}$ we obtain the following equality $\frac{P\infty - P}{P\infty - Pv}$. If the local blade pressure equals the liquid vapour pressure the equality evaluates to 1, and cavitation occurs, for values smaller than one cavitation doesn't occur.

Structural Analysis

OpenProp includes a routine for stress analysis, this function is responsible for performing the structural analysis and displaying the results to the user. It takes as input the results of the propeller analysis and determines the blade geometry, section centroid and moments of inertia to calculate the stress on the entire blade. Thus the maximum stress is found and can be compared to the maximum allowed stress given by the material property.

4.3 PMSM Design Methodology

For the design of the PMSM a FEA software is used in conjunction with Matlab routines to test the different designs generated by the GA in the Matlab environment. The geometry generated follows the topology represented in Figure 4.8.

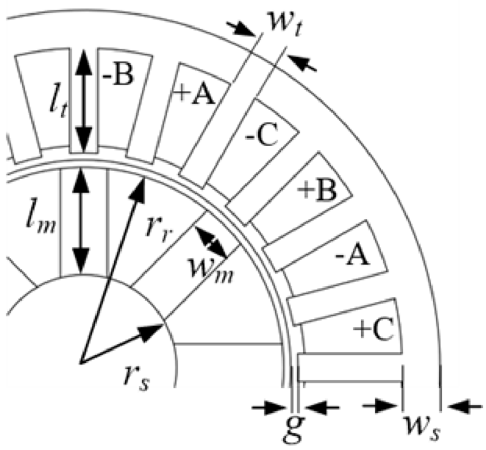

Figure 4.8: Visual representation of the motor design variables, taken from [14]

Hybrid Model

The used model is a hybrid-model, using both analytical equations and the Finite Element Method (FEM) (2D FEM model + analytical models) to simulate a PMSM. This model was used to design motors for a 4-motor competition electric vehicle's powertrain in [13]. First, a nominal point is chosen, determining the torque and rotational speed for the synchronous machine. The voltage limit is set by the voltage of the system architecture and the current limit is set by the maximum power required for the application, defined during the concept stage of the project.

The analytical model is based on the synchronous $d-q$ reference frame of a PMSM's equivalent circuit shown in Figure 4.9 [51]. This model considers the iron losses through an equivalent resistance.

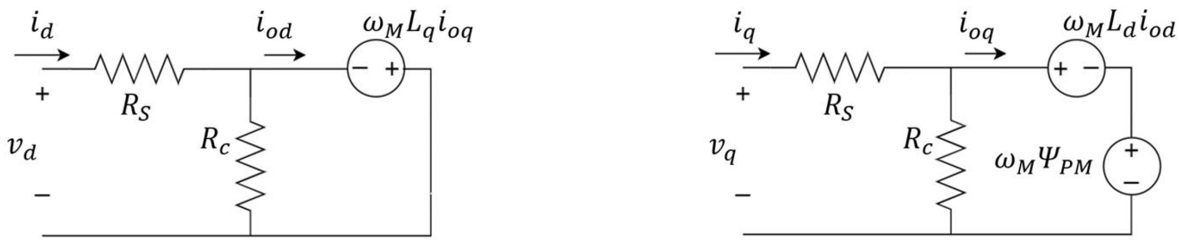

Figure 4.9: Synchronous machine equivalent circuit considering core-losses on a d-q reference frame, taken from [14].

In Figure 4.9, v_d, v_q, i_d and i_q are the $d-q$ axis stator voltages and currents, i_{od} and i_{oq} are the torque generating currents, R_s is the phase winding resistance, R_c is the equivalent core-loss resistance, L_d and L_q are the $d-q$ inductances, w_M is the rotor angular speed.

To estimate the parameters of the equivalent circuit three stationary FEM simulations are performed to determine the magnetic flux through the PMs, Ψ_{PM}. The inductances given in the $d-q$ reference frame L_d and L_q and the equivalent core-loss resistance, R_c are also estimated in the stationary simulation. The analytical expressions are used to determine the currents along the d and q axis with the target torque T_{target}, the rotation speed ω_{target} and the values obtained in the stationary simulation. Equations 4.16-4.18 are obtained from the equivalent circuit [14]:

$$v_d = R_c \cdot i_{od} - \omega \cdot i_{oq} \cdot L_q, \tag{4.16}$$

$$v_q = R_c \cdot i_{oq} - \omega(i_{od} \cdot L_d + \Psi_{PM}), \tag{4.17}$$

$$T = \frac{3n_{pp}}{2}[(L_d - L_q)i_{od} \cdot i_{oq} + \Psi_{PM} i_{oq}]. \tag{4.18}$$

After ensuring that the currents and voltages are within the designated limits, a simulation using FEM is performed for each operating point to determine the magnetic flux, B, and motor temperature. The optimisation algorithm then checks if the magnetic flux, Ψ_{PM}, temperature within the motor, and the demagnetization percentage of the magnets are within the desired limits. Any non-compliant individual is discarded. Next, the losses in the winding and stator are added to calculate the overall efficiency of the motor. By determining the weight of copper, iron, and PM, the total weight is calculated.

Material Properties

The selection of materials for each specific motor domain is based on its location within the motor. In this case, NO15 non-oriented electrical steel was chosen for both the rotor and stator domains whose characteristics are listed in Table 2.1. Standard copper was chosen for the coils. $NdFeB$ was defined as the appropriate material for the domain of the PMs, as detailed in Table 2.2. Finally, the remaining domains such as the shaft domain and air-gap domain were selected as air.

Boundary Conditions

The boundary conditions for the 2D FEA simulation are defined for each domain according to the following:

1. The magnetic insulation is set for the outer diameter of the stator;
2. Stator and rotor core are selected with a constitutive relation defined by its B-H curve;
3. PM with a constitutive relation defined by the remanent magnetic flux density, perpendicular to the magnet radial axis, with $1.6\,\mathrm{T}$ and with the same magnetic poles facing two consecutive magnets;
4. The coils domains are selected having a sinusoidal external current density with an amplitude of $30\,\mathrm{A\,mm^{-2}}$, with a phase difference of one-third the period between each phase and with a frequency of $164\,\mathrm{Hz}$.

The current density was defined taking into consideration that $10\,\mathrm{A\,mm^{-2}}$ is the boundary between a highly efficient heat removal fan cooling system and a non-efficient heat removal liquid cooling system (that can increase to $30\,\mathrm{A\,mm^{-2}}$ for high-efficient systems). A thermal analysis was conducted to verify the cooling solution efficacy in Chapter 5 and the theoretical background is reviewed in Section 4.3.2.

4.3.1 Time-Dependent Simulation

The selected geometries from the optimisation were simulated with a 2D time-dependent simulation for the optimised load angle at the nominal frequency determined by the nominal rotational speed. The time-dependent simulation allows for a more precise result of the losses, including the PM losses and torque ripple. Total core losses, P_{core}, are obtained from the sum of the losses in each element index, i, density, ρ, and area, A_i, as shown by the following equation:

$$P_{core} = \sum_i \rho A_i L_i \cdot p_i. \tag{4.19}$$

In conductive materials with induced currents, such as PMs, Joule losses are computed from:

$$P_{PM} = \int_V \frac{|\mathbf{J}|^2}{\sigma} dV, \tag{4.20}$$

where V is the PM's volume, σ the conductivity, and $\mathbf{J}$ is the induced current density variation in time in the PM's. The winding losses are calculated with Equation 4.21, the same way as in the steady-state simulation:

$$P_{Cu} = \frac{3}{2} R_s (i_d^2 + i_q^2). \tag{4.21}$$

The efficiency was computed considering winding losses, as in the previous section, and core and induced current losses with these presented methods. By analysing a set of points other than the nominal an efficiency map can be constructed.

4.3.2 Thermal Analysis

The thermal phenomenon is critical to determine if the machine is adequately cooled and does not overheat. The insulation of the copper windings and the magnets present the main thermal constraints for an electric machine. For the chosen geometry a 3D steady-state thermal simulation is performed using the losses obtained from the time-dependent analysis. The thermal properties of the materials are shown in Table 4.1.

Table 4.1: Thermal properties of materials used in the thermal simulation.

Materials\Characteristics	Thermal Conductivity [$\mathrm{W\,m^{-1}\,K^{-1}}$]	Heat Capacity [$\mathrm{J\,kg^{-1}\,K^{-1}}$]	Density [$\mathrm{kg\,m^{-3}}$]	Source
Stainless Steel	16.3	0.5	8000	[27]
Copper	398	0.385	8930	[52]
PM	9	460.54	7700	[22]
Silicon Steel	23	600	7650	[17]
Insulation Paper	0.046	1200	830	[53, 54]
Filling resin	0.11	1050	1200	[55]

The copper windings are constituted by a certain number of wires that are distributed by the slots, but they do not occupy the whole space. Modelling each strand is very time-consuming so a simplified aggregate model is used, this method is described in more detail in in [55, 56]. An effective heat transfer coefficient and heat capacity are calculated with the average distribution of copper, insulation paper, impregnation resin and air that occupy the slot space. The winding's effective thermal conductivity is calculated by:

$$k_{eff} = k_{cu} \frac{A_{cu}}{A_{total}} + k_{paper} \frac{A_{paper}}{A_{total}} + k_{resin} \frac{A_{resin}}{A_{total}} + k_{air} \frac{A_{air}}{A_{total}}, \tag{4.22}$$

the effective heat capacity is calculated analogously. For the air gap, a laminar flow model was used, a no-slip condition with a sliding wall boundary was applied to the rotor wall, and the stator wall was considered fixed. On the outer wall of the stator, a convective heat flux boundary condition was applied, the heat flux is calculated by:

$$q_0 = h(T_{ext} - T), \tag{4.23}$$

where T_{ext} is the external water temperature, T is the boundary surface temperature and h is the convective heat coefficient which is determined by:

$$h = \begin{cases} 2\dfrac{k0.3387Pr^{1/3}Re_L^{1/2}}{L(1+(\frac{0.0468}{P_r})^{2/3})^{1/4}} & Re_L \leq 5 \cdot 10^5 \\ 2\dfrac{k}{L}Pr^{1/3}(0.037Re_L^{4/5} - 871) & Re_L > 5 \cdot 10^5 \end{cases}, \tag{4.24}$$

where k is the thermal conductivity coefficient of the boundary material, L is the length of the motor along the streamwise direction, Pr is the Prandtl number given by the ratio of momentum diffusivity to thermal diffusivity of the water and Re_L is the Reynolds number calculated at length L [57].

Heat sources are defined at the positions of the stator, windings, PMs and rotor. The respective heat rates are given by the losses calculated previously.

5

MPS Detailed Design

MPS Detailed Design

This chapter details the optimisation results obtained for both the PMSM and the CRP. Modifications to the design approach made during the optimisation are also touched upon. Thermal and fluid simulations are presented as a verification study to confirm the design validity. Finally, the 3D model of the complete system is presented and additional design choices are presented.

5.1 Detailed Motor Design

The optimization vector $x = [J_o, r_r, r_s, w_m, l_m, w_t, l_t, g, w_s]$ is made up of geometric decision variables, that defines the motor's geometry, and an electrical variable, the amplitude of the torque producing current density. The constraints of these variables are presented in Table 5.1 and visually represented in Figure 4.8.

Table 5.1: Design variables for the electric motor.

Type	Variable	Description	Range
Geometric	r_r	Rotor radius	20-30 mm
	w_s	Stator outer ring width	5-30 mm
	w_m	Magnet width	5-7 mm
	l_m	Magnet length	5-30 mm
	w_t	Teeth width	5-20 mm
	l_t	Teeth length	1-30 mm
	g	Airgap size	0.5-1.5 mm
	r_s	Shaft radius	10-60 mm
Electrical	j_o	Amplitude of torque producing current density	5-30 $\mathrm{A\,mm^{-1}}$

The objective function is to maximize the efficiency of the motor and minimize its weight so that it satisfies the required operating points. The required operating points are the nominal operation point, $36\,\mathrm{N\,m}$ at $2260\,\mathrm{RPM}$, and the take-off torque, $100\,\mathrm{N\,m}$ at $2300\,\mathrm{RPM}$. The weight, $W(x)$, is taken as the sum of the weight of the magnetic core, W_{core}, the permanent magnets, W_{PM} and the of the copper windings W_{Cu}. The objective efficiency $\eta(x)$ considers the useful output power at the nominal operating point, $T_n(x)\omega_n$, and considers only the copper loss, P_{Cu}, and core loss in the stator, P_{stator}, as losses for that operating point.

5.1.1 First Iteration

The resulting pareto curve of the first optimisation run is shown in Figure 5.1. The geometries generated at the last generation simulated indicated that the solution would converge onto a narrow range of geometries.

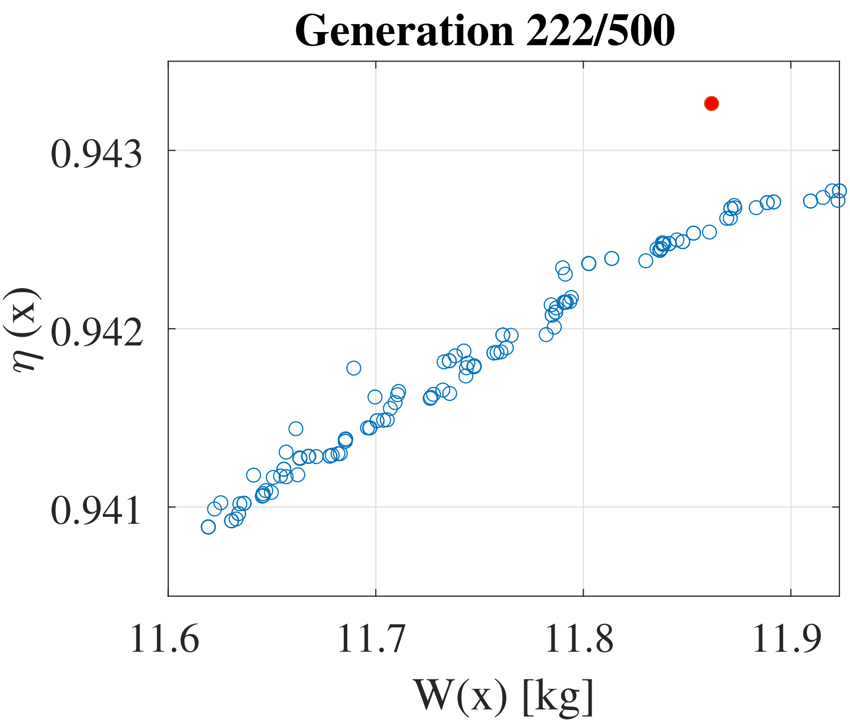

Figure 5.1: Pareto curve from the first optimisation. Population size 150, at generation 222, selected solution in red.

The efficiency of the obtained solutions was low in comparison to the expected result of efficiencies greater than $96\,\%$. The results obtained from the first optimisation batch were therefore not satisfactory. Since weight is a lower priority than efficiency further optimisations were performed to increase efficiency at the cost of weight. For example, between two individuals, one with $12\,\mathrm{kg}$ and $94\,\%$ efficiency and another with $16\,\mathrm{kg}$ and $96\,\%$ efficiency, the one with higher efficiency is more desirable since a difference of $4\,\mathrm{kg}$ is insignificant concerning the overall weight of the vessel. However, a difference of $2\,\%$ can improve the overall efficiency and energy consumption of the vessel. The obtained geometry is shown in Figure 5.2.

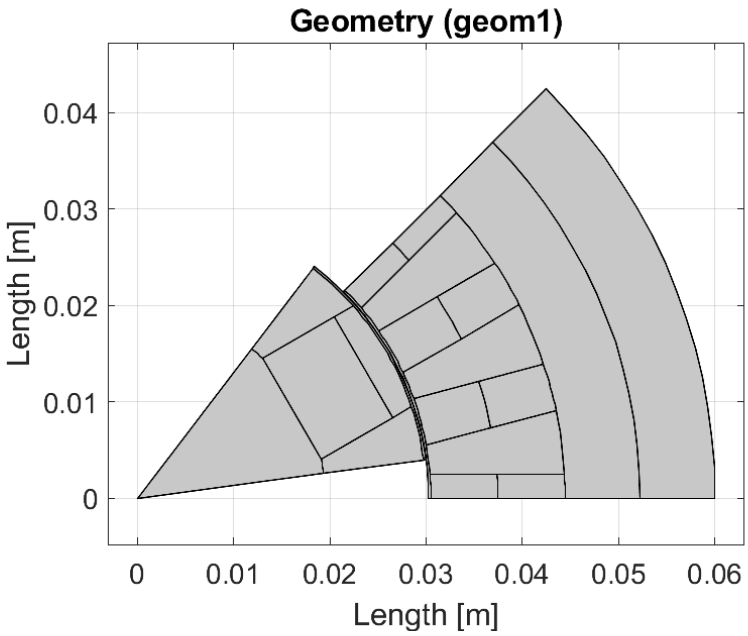

Figure 5.2: Geometry of solution 148 of the population at generation 222.

A time-dependent simulation was performed as a verification step. This revealed that the motor had some torque ripple issues as the torque in one rotation would vary up to $20\,\mathrm{Nm}$ as seen in Figure 5.3.

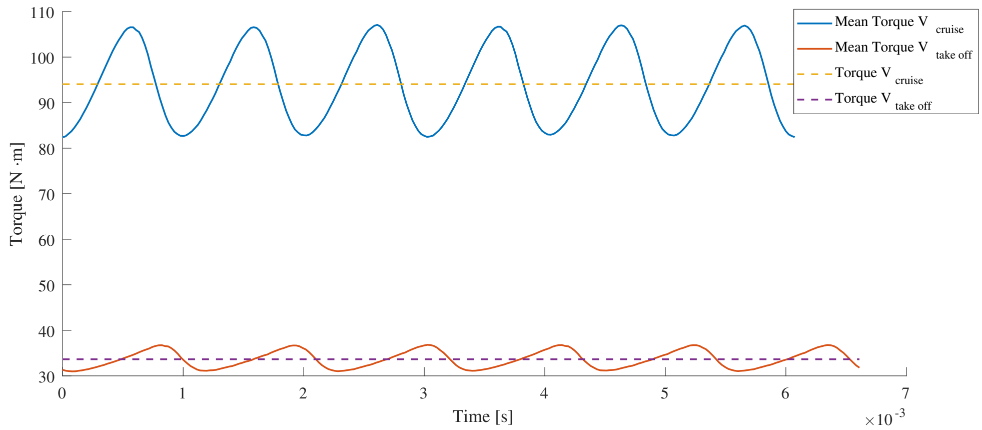

Figure 5.3: Time-dependent torque result of solution 148.

With a torque ripple that high the motor would have major vibration issues and a high risk of mechanical failure. The issue could be mitigated by a more detailed rotor geometry, by smoothing out the flux distribution, but this study was left for the final motor design simulation.

5.1.2 Final Motor Iteration

For the final iteration, the values of torque and rotation speed were updated to the results of the CRP optimisation results. The required operating points were adjusted to $26.5\,\mathrm{N\,m}$ at $2262\,\mathrm{RPM}$ for the cruise condition and $90.5\,\mathrm{N\,m}$ at $2365\,\mathrm{RPM}$ for the take-off condition. The resulting pareto curve is given in Figure 5.4. The PM width was constrained to values between $5\,\mathrm{mm}$ and $7\,\mathrm{mm}$ to obtain a result with better efficiency and less torque ripple.

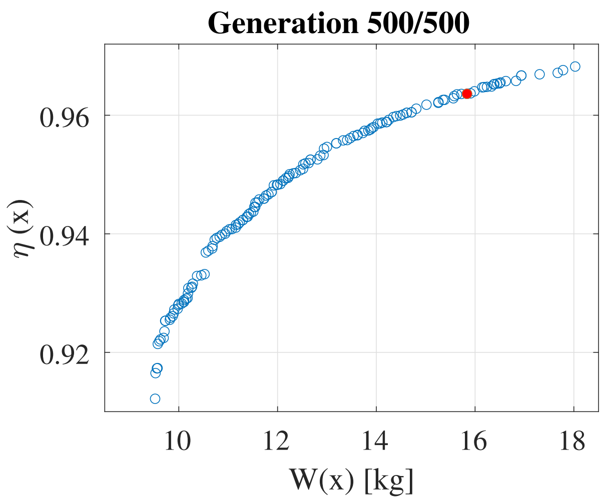

Figure 5.4: Pareto curve from the first optimisation. Population size 150, at generation 500. Selected Solution in red.

The selected solution is individual 132/150, the geometrical and electrical variables are presented in Table 5.2.

Table 5.2: Variable and objective results for individual 132/150.

Decision variables								
j_0	r_r	r_s	w_m	l_m	w_t	l_t	g	w_s
$10.37\,\mathrm{mm}$	$30\,\mathrm{mm}$	$14\,\mathrm{mm}$	$7\,\mathrm{mm}$	$14.6\,\mathrm{mm}$	$6\,\mathrm{mm}$	$17\,\mathrm{mm}$	$1.4\,\mathrm{mm}$	$5\,\mathrm{mm}$
Objectives			**Other**					
η_1	η_2	W	L_{core}					
$96.4\,\%$	$90.8\,\%$	$16.99\,\mathrm{kg}$	$289\,\mathrm{mm}$					

The diameter of the motor decreased from $120\,\mathrm{mm}$ to $110\,\mathrm{mm}$, this helps to reduce the drag generated by the torpedo shape of the motor housing by reducing the frontal area. The resulting geometry is depicted in Figure 5.5.

The chosen optimisation solution fulfils the required constraints and operating points with reasonable efficiency and weight and a good thermal safety margin. However, the question of high torque ripple due to the high reluctance variation along the airgap, characteristic of the spoke-type permanent magnet arrangement in the rotor, remains. A parametric study of the rotor shape was performed to reduce the torque ripple. Additionally, the gap length is decreased to 1 mm, as it increases the torque per ampere and the efficiency. The geometry of these changes can be observed in Figure 5.6.

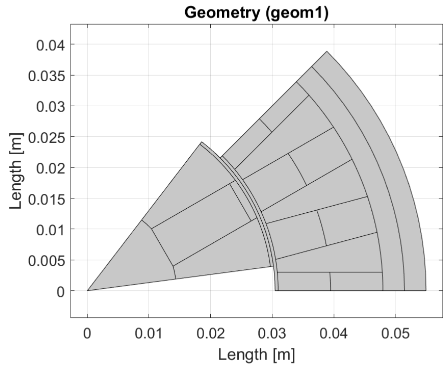

Figure 5.5: Geometry of solution 132 of the population at generation 500.

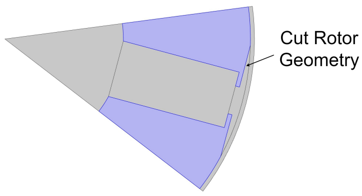

Figure 5.6: Optimised cut rotor geometry.

The parametric study included different cut angles of the rotor geometry. The goal was to find the optimum cut angle to try to help even out the torque production over one rotation. The obtained result comparison is presented in Figure 5.7.

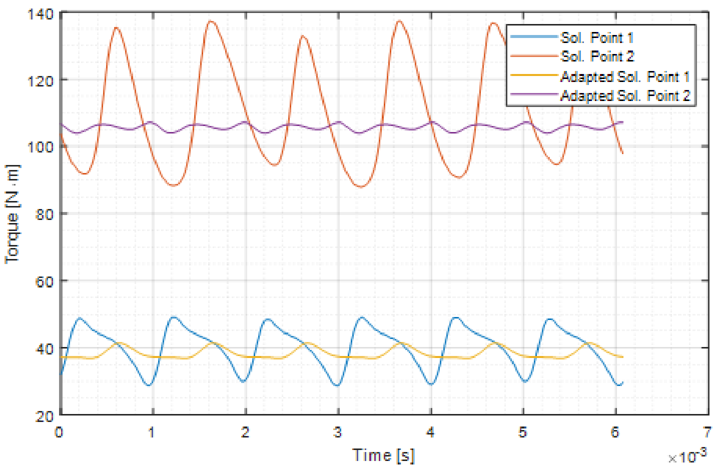

Figure 5.7: Torque ripple before and after the adapted solution.

The blue and red lines represent the torque fluctuation of the original solution over the given period. The yellow and purple lines represent the torque ripple of the adapted solution. The torque ripple is reduced by $93.3\,\%$ at the takeoff condition and by $75\,\%$ at the cruise condition. The final torque ripple values are $2.8\,\%$ and $13.2\,\%$ of the nominal torque at takeoff and cruise conditions respectively. The cruise torque ripple is still quite high but functional. To further torque ripple mitigation control-based torque ripple mitigation algorithms can be applied during operation [58]. The efficiency, input voltage and input current of the adapted geometry is presented in Table 5.3.

Table 5.3: Performance of adapted solution.

	Cruise state	**Takeoff state**
Torque $[\mathrm{N\,m}]$	38.4	105.7
Efficiency $[\%]$	96.4	91.0
Input current $[A_{RMS} \cdot turn]$	223	659
Input voltage (Phase-Neutral)$[V_{RMS} \cdot turn^{-1}]$	16.77	16.85

5.1.3 Efficiency Map

As the motors will operate in more conditions apart from the design points the performance across the whole range of operation must be analysed. To obtain a good picture of the motor performance an efficiency map is often used. The losses are estimated using the 2D time-dependent simulations performed in Comsol for various operating points and thus the efficiency can be calculated and interpolated between points. Figure 5.8 presents the predicted efficiency map for the motor.

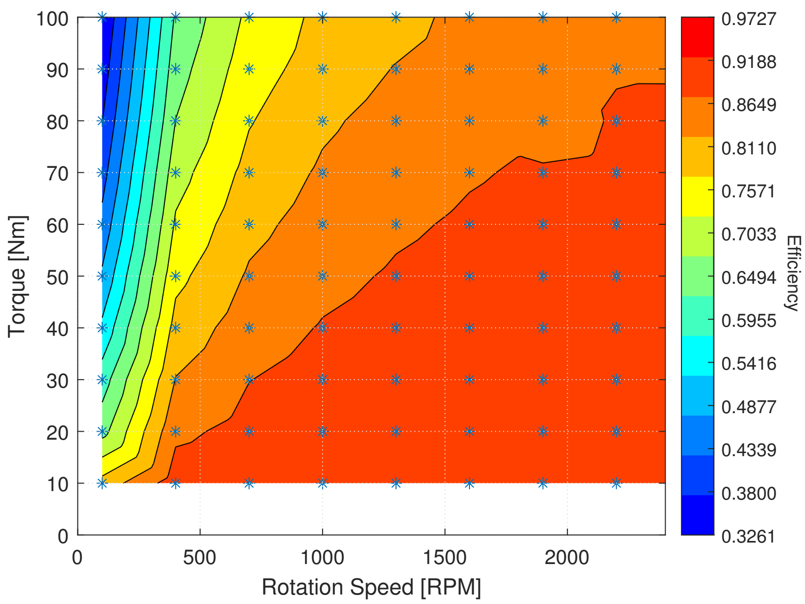

Figure 5.8: Predicted efficiency map of the motor,
the points represent the simulated data from which the map is interpolated.

5.1.4 Choosing Winding Characteristics

The windings' wire diameter and number of turns are determined by the maximum current and voltage the selected inverter can output. The inverter must be selected such that the output frequency is compatible with the desired motor speed, the apparent power is satisfied, and the number of turns is viable. The inverter maximum output current, I_{inv}, the inverter output voltage, V_{inv}, the motor's maximum current-turns (Root Mean Square (RMS)) I_{motor}, and phase to phase voltage per turn, (RMS) V_{motor}, and the number of turns, N, must satisfy the following conditions:

$$I_{inv} > \frac{I_{motor}}{N}, \tag{5.1}$$

$$V_{inv} > \sqrt{3}V_{motor}. \tag{5.2}$$

The maximum cross-section of the wire, A_{wire}, is dependent on the available area in the slot, A_{slot}, and the filling factor, f_w, taken as 0.4 in the presented optimisation:

$$A_{wire} < \frac{A_{slot} f_w}{N}, \tag{5.3}$$

from the wire's cross-section, its diameter can be determined. No specific inverter was selected as it is determined by factors outside the scope of this work. The range of the expected number of turns is between 21 and 24 and thus the expected area of the wire, A_{wire}, is between $2.96\,\mathrm{mm}^2$ and $2.59\,\mathrm{mm}^2$, which translates to a wire gauge of $14\,\mathrm{AWG}$ [59].

5.1.5 Thermal Simulation

To verify that the motors do not overheat a 3D steady-state thermal simulation at the takeoff condition was performed. The method described in Section 4.3.2 and the losses calculated in the time-dependent 2D simulation were used as inputs for the thermal simulation. The highest contribution is from the windings, generating $2538.1\,\mathrm{W}$ of heat.

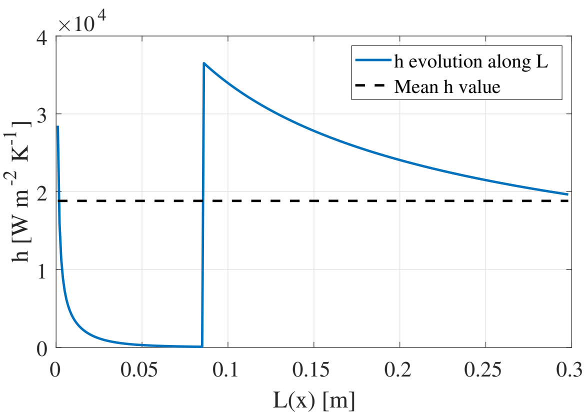

Figure 5.9: Heat transfer coefficient for the forced convection along the motor.

Figure 5.9 shows the heat transfer coefficient distribution and the average value. The values are over $1.8 \times 10^4\ \mathrm{W\,m^{-2}\,K^{-1}}$ which is on the higher end of the heat transfer coefficient in forced convection for water. The geometry for the simulation was the extruded profile from Figure 5.5 and patterned to complete the full motor geometry. The shaft extensions were omitted as well as its heat dissipation to simplify the simulation. The stator shell was also omitted to simplify the geometry, since the thermal conductivity of aluminium is very high this will not compromise the simulation results.

The simulation result is presented in Figure 5.10.

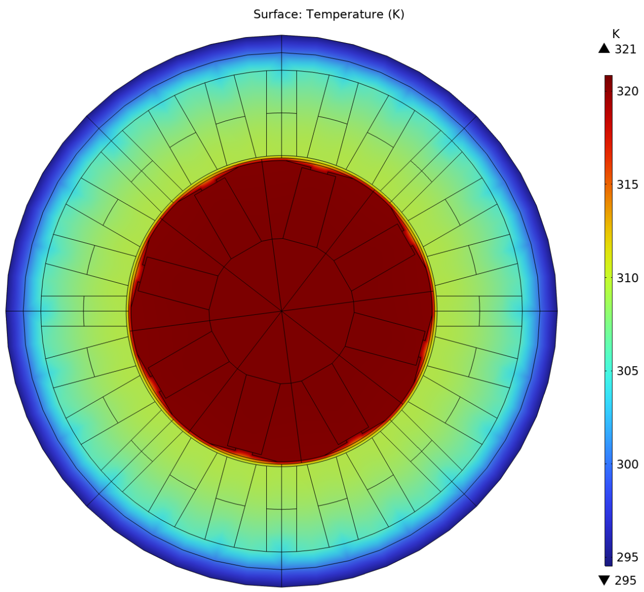

Figure 5.10: Temperature distribution inside the motor.

The simulation shows that the temperature inside the motor is most concentrated in the rotor since it is not directly in contact with the stator and thus has less cooling. The rotor temperature might be lower in reality than predicted from the simulation since the shaft is also in contact with the propeller and will provide some heat dissipation. The temperatures are well below the maximum for the PM and the insulation for the windings of $80\,^{\circ}\mathrm{C}$, making this solution very well-suited to cool the motors even at the takeoff condition since the motors have a large external surface area in contact with the seawater that provides an excellent heat removal rate.

5.2 Detailed CRP Design

The optimisation vector for the CRP system is comprised of the geometric decision variables that define the blade shape. The constraints of these variables are presented in Table 5.4. These constraints are based on the last optimisation run, as the first ones had more restrictive boundaries to test the program in a more controlled manner.

Table 5.4: Design variables for the CRP system.

Variable	Description	Range	Variable	Description	Range
$\mathbf{D_{forward}}$	Diameter of the front propeller	0.23 - 0.275 m	$\mathbf{D_{back}}$	Diameter of the back propeller	0.24 - 0.28 m
$\mathbf{C1_{forward}}$	1^{st} Chord to radius ratio of front propeller	0.14 - 0.26	$\mathbf{C1_{back}}$	1^{st} Chord to radius ratio of back propeller	0.14 - 0.26
$\mathbf{C2_{forward}}$	2^{nd} Chord to radius ratio of front propeller	0.145 - 0.265	$\mathbf{C2_{back}}$	2^{nd} Chord to radius ratio of back propeller	0.145 - 0.265
$\mathbf{C3_{forward}}$	3^{rd} Chord to radius ratio of front propeller	0.185 - 0.315	$\mathbf{C3_{back}}$	3^{rd} Chord to radius ratio of back propeller	0.185 - 0.315
$\mathbf{C4_{forward}}$	4^{th} Chord to radius ratio of front propeller	0.200 - 0.340	$\mathbf{C4_{back}}$	4^{th} Chord to radius ratio of back propeller	0.200 - 0.340
$\mathbf{C5_{forward}}$	5^{th} Chord to radius ratio of front propeller	0.220 - 0.380	$\mathbf{C5_{back}}$	5^{th} Chord to radius ratio of back propeller	0.220 - 0.380
$\mathbf{C6_{forward}}$	6^{th} Chord to radius ratio of front propeller	0.220 - 0.390	$\mathbf{C6_{back}}$	6^{th} Chord to radius ratio of back propeller	0.220 - 0.390
$\mathbf{C7_{forward}}$	7^{th} Chord to radius ratio of front propeller	0.220 - 0.390	$\mathbf{C7_{back}}$	7^{th} Chord to radius ratio of back propeller	0.220 - 0.390
$\mathbf{C8_{forward}}$	8^{th} Chord to radius ratio of front propeller	0.180 - 0.320	$\mathbf{C8_{back}}$	8^{th} Chord to radius ratio of back propeller	0.180 - 0.320
$\mathbf{C9_{forward}}$	9^{th} Chord to radius ratio of front propeller	0.120 - 0.260	$\mathbf{C9_{back}}$	9^{th} Chord to radius ratio of back propeller	0.120 - 0.260

The objective function is to maximise the efficiency of the propeller system and to minimise the torque required at take-off. The operating points were first comprised of a pair of velocity and resistance that were fixed, but in order to evaluate the changes in boat geometry the resistance routine detailed in section 4.2 was implemented into the optimisation routine. Making the operating point dependent only on the vessel velocity. The cruise speed was fixed at $20\,\mathrm{kn}$ and the take-off speed at $12\,\mathrm{kn}$.

To determine the operating point of each propeller the systematic series is used. The problem at hand is that of known thrust and diameter, so the rotation rate can be eliminated, the following equation is used according to [47]:

$$\frac{K_T}{J^2} = \frac{T}{\rho D^2 V_e^2}, \tag{5.4}$$

where D is the propeller diameter, T is the corrected propeller thrust calculated in Equation 5.6 and and V_e is the effective wake velocity given by:

$$V_e = (1 - w_T)V, \tag{5.5}$$

where w_T is the mean Taylor wake fraction, which is the average of the wakefield created by the flow around the hull. This will affect the effective inflow velocity of the propeller plane. The corrected thrust, T, comes from the change in the hull resistance due to the propeller action,

$$T = \frac{R}{1 - t}, \tag{5.6}$$

where R is the ship's resistance and $1 - t$ is the thrust deduction factor. Both the Taylor wake fraction and the thrust deduction factor are found either by experiment or estimation. Since the propeller is far away from the hull, $z_{prop} > 10 \cdot D_{prop}$, both values are assumed to be zero in this work.

Equation 5.4 gives the curve $K_T = k \cdot j^2$, this curve may be plotted in the open water diagram to find the ship's operating point as this curve represents the demand for thrust from the ship side. This operating point gives the rotation rate, torque and efficiency of the propeller at the given thrust. An example of the resulting curve is given in Figure 5.11.

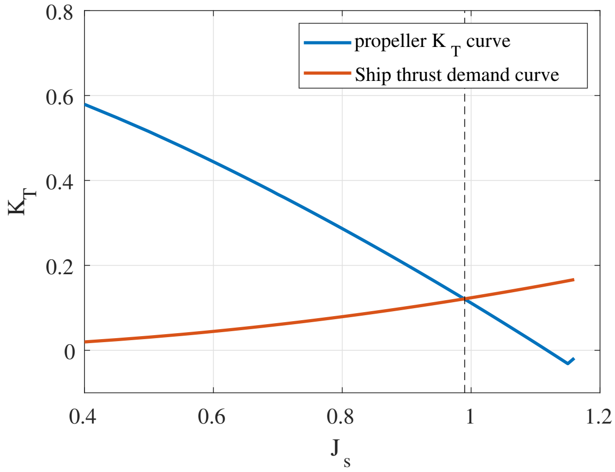

Figure 5.11: Thrust demand curve intersection with propeller K_T open water curve.

5.2.1 Iterations

Four final solutions were selected for final evaluation after more than 15 optimisation runs were performed. The data from the results for the takeoff condition are compiled in Table 5.5 and for the cruise condition in Table 5.6.

Table 5.5: Solution data for takeoff condition.

	Eff [%]	Thrust [N]	K_T	Torque [N m]	K_Q	RPM	J_s	Input Power [kW]
SOL 1	55.62	4368	0.5152	175.62	0.0799	2551.7	0.5420	46.93
SOL 2	54.94	4368	0.5227	172.66	0.0813	2625.3	0.5369	47.46
SOL 3	58.22	4368	0.4739	179.81	0.0713	2378.3	0.5504	44.75
SOL 4	58.20	4368	0.4724	179.52	0.0710	2382.1	0.5496	44.78

From the data of the takeoff condition results it is possible to see that reducing the target rotation rate has a positive impact on the CRP efficiency, increasing from $54.94\,\%$ to $58.22\,\%$. This lowers the power consumption by $2.71\,\mathrm{kW}$. This increase in efficiency comes at the cost of increasing the torque demand. The results stayed below $200\,\mathrm{N\,m}$, accomplishing the objective.

Table 5.6: Solution data for cruise condition.

	Eff [%]	Thrust [N]	K_T	Torque [N m]	K_Q	RPM	J_s	Input Power [kW]
SOL 1	81.22	995.18	0.1469	50.05	0.0296	2363.7	1.0137	12.39
SOL 2	80.70	995.18	0.1414	51.22	0.0282	2325.1	1.0124	12.47
SOL 3	81.69	995.18	0.1202	50.14	0.0231	2253.4	0.9857	11.90
SOL 4	81.76	995.18	0.1202	50.17	0.0231	2253.6	0.9875	11.85

For the cruise condition, the solutions generated do not vary as much, having only a difference of $0.36\,\mathrm{kW}$ in the input power. The two solutions that have lower takeoff efficiency are therefore discarded.

Solutions 3 and 4 are very similar in geometry, making the choice irrelevant. Solution 4 is presented in Figure 5.12, which was chosen as the final geometry as it was the solution with the best takeoff efficiency and did not impact the cruise efficiency significantly. The respective open water curve is presented in Figure 5.13.

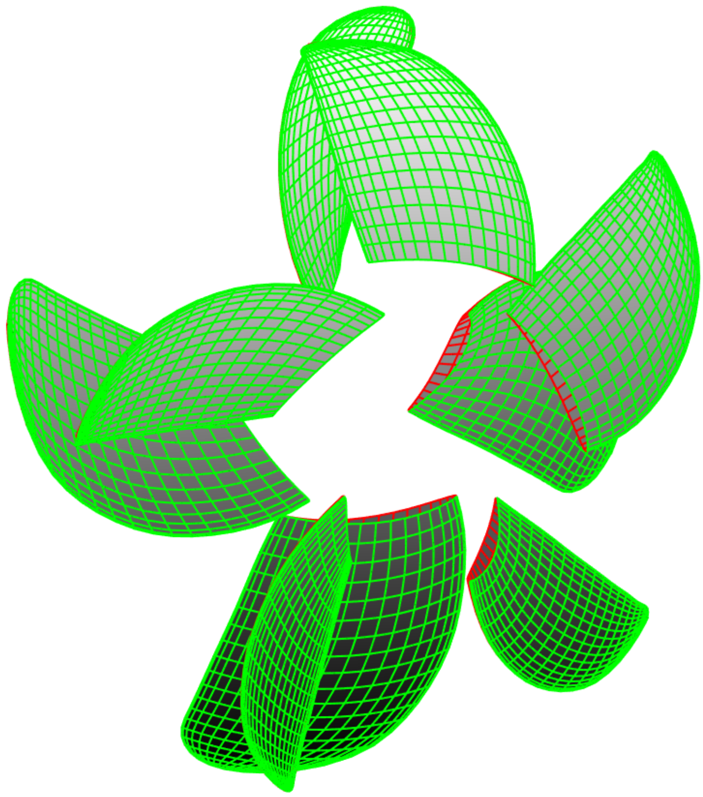

Figure 5.12: Propeller geometry output of solution 4 generated by OpenProp.

All geometries needed to be manually adjusted in order to produce a smooth propeller curve. This reveals that the OpenProp code is not very sensitive to chord variations that do not significantly change the blade area since altering the cord length to even out these irregularities did not alter the results significantly (less than $0.1\,\%$ of the efficiency). Each chord length along the radius is individually optimised which results in some unregular blade curves, due to the difficulty of convergence. A Class-Shape Function Transformation could be used to produce smooth chord distribution without the need to manually adjust the chord ratio after the optimisation process, but due to time constraints this was not implemented [60].

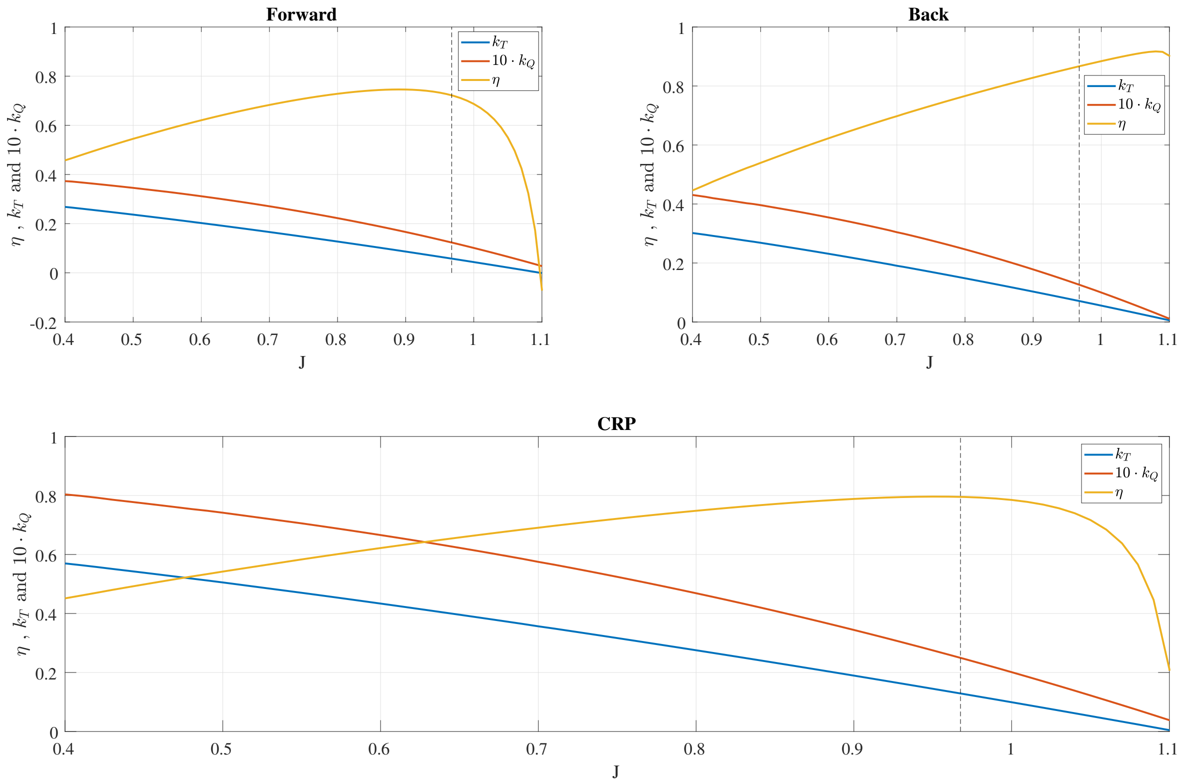

Figure 5.13: Propeller open-water graph of solution 4 generated by OpenProp. In the top left corner is the forward propeller, in the top right corner is the rear propeller and at the bottom is the combined graph for the CRP. Vertical dotted lines indicate the cruise advance coefficient.

Figure 5.13 shows that the efficiency of the front propeller is significantly lower than the rear propeller. Since the rear propeller receives the accelerated flow of the front propeller this increases the efficiency and therefore the overall efficiency.

The efficiency of the rear propeller does get close to $91\,\%$, but as the front propeller at the same J has an efficiency close to zero the whole system is compromised. So the complete CRP system gets to a maximum efficiency of $80\,\%$. Figure 5.13 also reveals that both propellers have an efficiency peak at different J values. Since each propeller is coupled to an individual motor the possibility arises to drive the propellers at different rotational speeds to try to further improve efficiency. This would require an extensive CFD analysis to predict the interaction of both propellers rotating at different speeds.

5.2.2 Cavitation Results

The constraints of the optimisation included that the minimum coefficient of pressure on the blade must be above -0.3 at the takeoff condition to guarantee that no cavitation is present at cruise speed. Attempts were made to eliminate cavitation at takeoff but no solutions were found that satisfied this condition. Future optimisation routines could include an objective to minimise cavitation occurrence at takeoff increasing the complexity of the optimisation scheme.

In Figure 5.14 the cavitation map of both propellers at takeoff condition are presented.

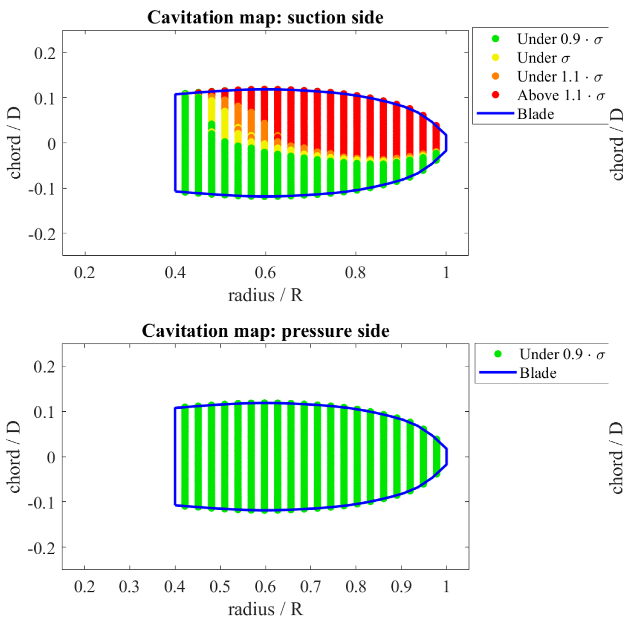

(a) Cavitation map of the front propeller at takeoff condition.

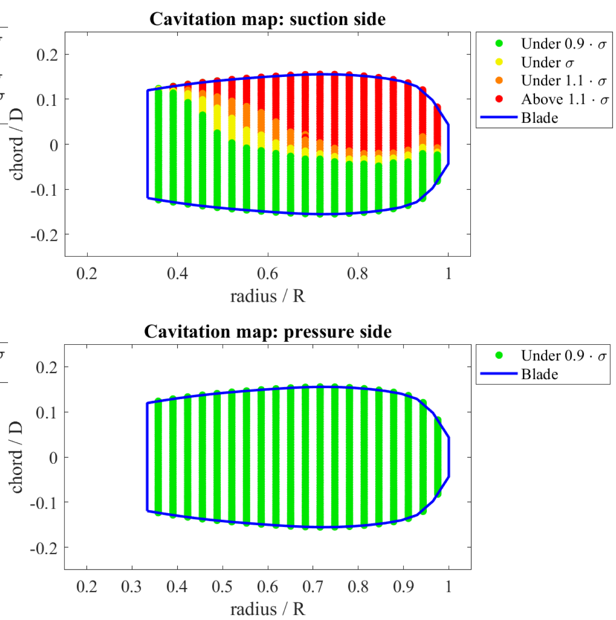

(b) Cavitation map of the rear propeller at takeoff condition.

Figure 5.14: Cavitation map of the propellers at takeoff condition.

For both propellers indications of sheet cavitation are present, given by the large area forming on the leading edge of the blade, where $\frac{-CP}{\sigma}$ is above 1.1. Due to the low advancement coefficient, $J = 0.5496$, at the takeoff the AoA of each blade is large and thus large suction peaks build up near the leading edge of the blades resulting in the blade back being covered with a sheet of bubbles. Further studies might be necessary to determine the influence of cavitation occurrence on performance.

The pitch distribution is deemed to be good as no face cavitation is detected in the performed study, as this type of cavitation occurs due to negative AoA developing on the blade. Root cavitation is also not present, but as the hub curvature is not taken into account in the study this could be another point of further study. The results of the cavitation analysis for both propellers at cruise conditions are presented in Figure 5.15.

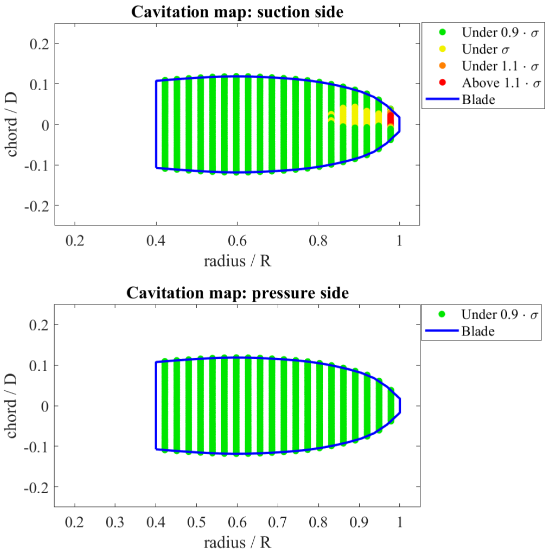

(a) Cavitation map of the front propeller at cruise condition.

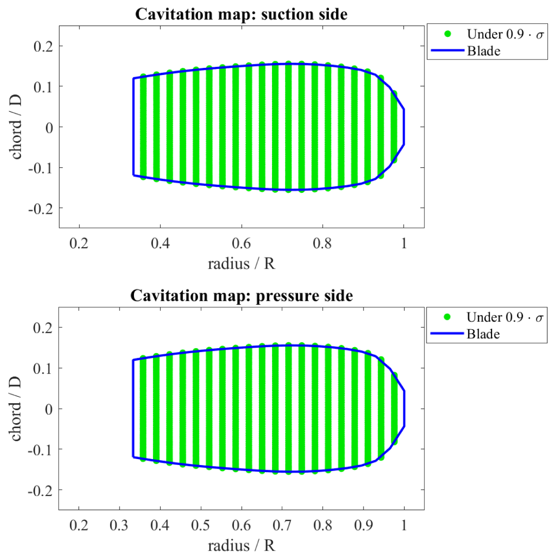

(b) Cavitation map of the rear propeller at cruise condition.

Figure 5.15: Cavitation map of the propellers at cruise condition.

In Figure 5.15a some cavitation might occur at the Tip of the front propeller. Tip vortex cavitation might negatively impact hydrodynamic noise and vibration [61].

5.2.3 Structural Analysis

To ensure good strength of the propeller blades the maximum allowed stress of the blade during optimisation was set at five times lower than the material yield strength ($265\,\mathrm{MPa}$) taken from Table 2.4. This leads to a factor of safety of 8.28.

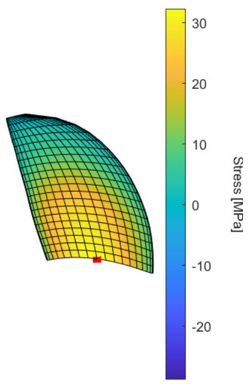

(a) Blade stress of the front propeller at takeoff condition.

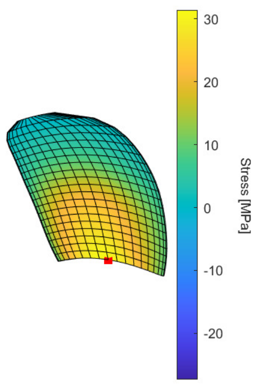

(b) Blade stress of the rear propeller at takeoff condition.

Figure 5.16: Blade stress of the propellers at take condition.

Both propellers met the requirement, the added thickness of the blades will impact the overall weight of the system, but it is negligible in comparison to the weight of the hub.

5.2.4 CFD Analysis

To validate the optimisation results of the propellers CFD calculations were performed using Star CCM+ [62]. To perform these simulations a domain needs to be established, Figure 5.17 contains the main dimensions of this domain. Each propeller has its subdomain making it possible to rotate each to simulate the operation of the CRP system. The torpedo body is included in the calculation to provide a more realistic flow pattern. The sliding mesh method is used to simulate the rotation of each propeller and the interfaces between the sliding faces are defined.

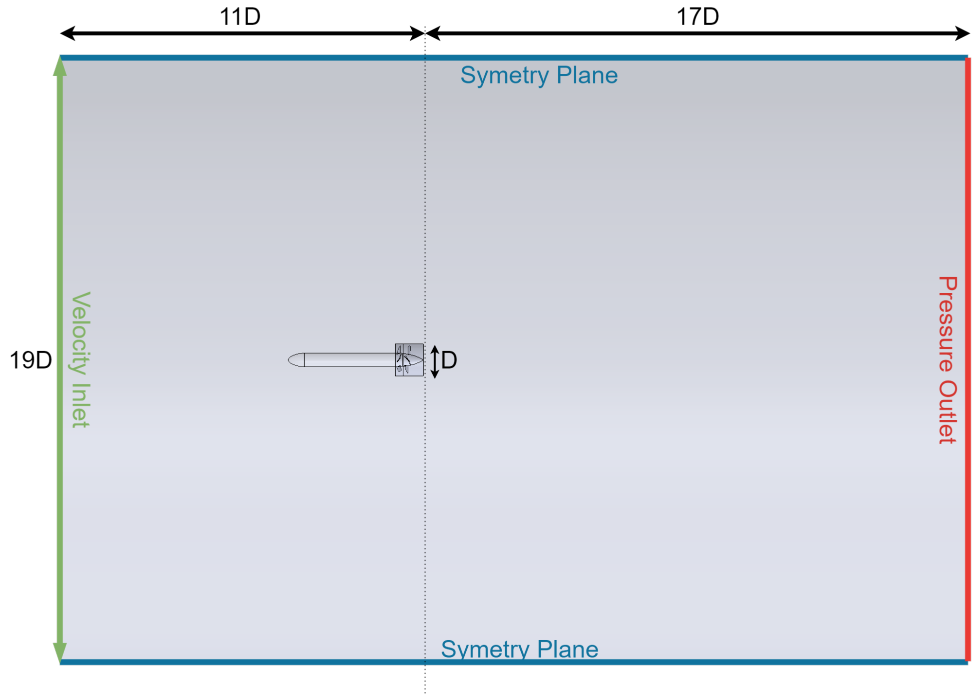

Figure 5.17: Computational domain and boundary conditions.

The mesh is generated for each domain with the appropriate boundary conditions applied. Figure 5.18 presents a section of the generated mesh with a close-up of the propeller area. The fluid domain is meshed with a trimmed cell surface-to-volume mesher, while both propeller domains are meshed with a polyhedral surface-to-volume mesher. The surface-to-volume approach is the most used method since it captures the geometry more accurately than the volume-to-surface approach. A wall function with $y+$ maintained $y+ < 5$ on the propeller and hub wall in the open-water simulations.

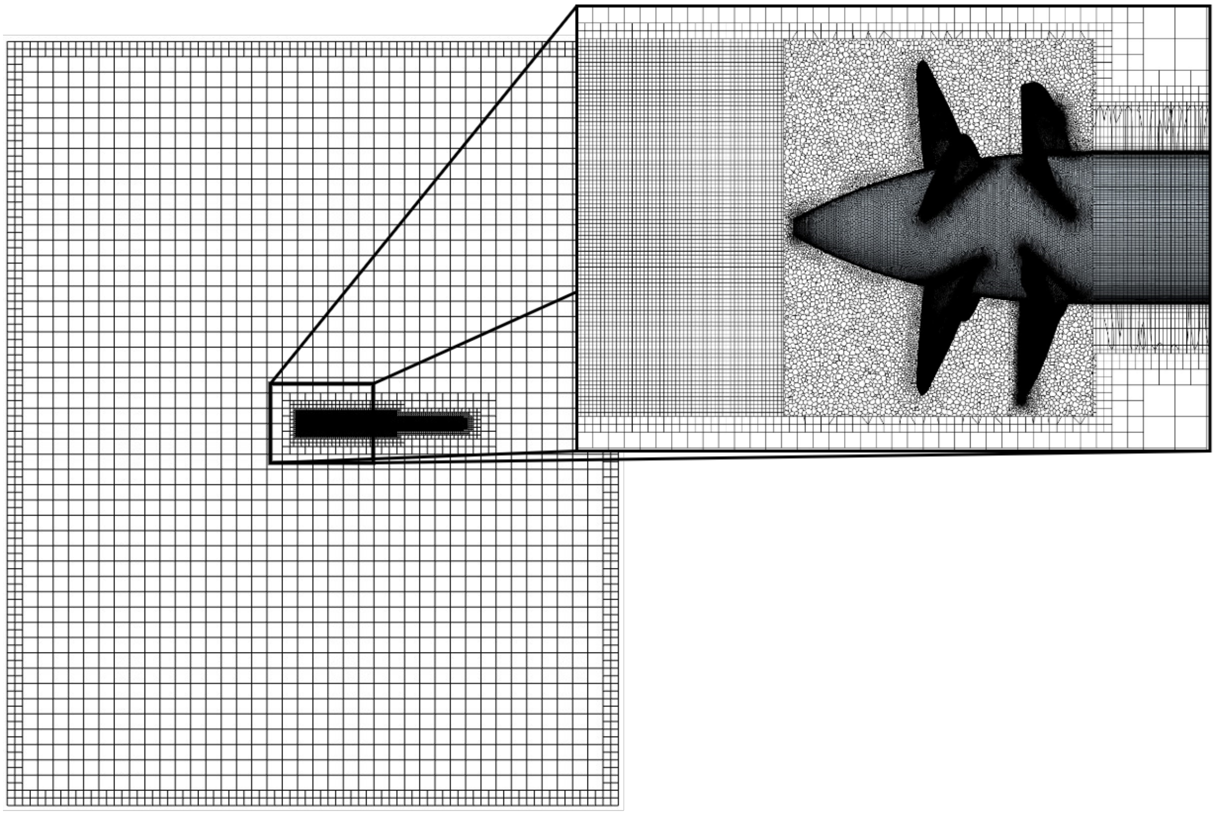

Figure 5.18: Propeller mesh with close up.

The solvers and models used are the following:

- Coupled Flow;
- Constant Density;
- Implicit Unsteady;
- k-ω SST Turbulence model.

The Integral values of the thrust and torque are calculated by solving the reaction force at the boundaries. The turbulent flow field around the propulsor is also solved and the drag force of the torpedo is evaluated.

The mesh details are presented in Table 5.7.

Table 5.7: Mesh size data and mesh quality data.

	Total Cell Count	Lowest Cell Quality	Highest Skewnes angle [°]	Lowest Least Squares Quality
Fluid Mesh	3.68 M	0.0167	83.88	0.0258
FP Mesh	10.82 M	3.9e-4	86.80	2.57e-3
RP Mesh	12.35 M	9.967e-4	87.7	8.716e-4

The worst quality cells are located in the region of the tip of the propellers and at the trailing edge near the tip. Further improvement of the cells was not possible due to time constraints, but the number of these cells is low, less than $1\,\%$ of the total number of cells.

Simulations were performed for a range of advance coefficients, maintaining a constant rotation speed and varying the inflow speed. To obtain a solution without divergence an under-relaxation factor ramp was used, starting at a value of 0.2 for the first 1000 iterations, growing linearly to 0.8 by 3500 iterations. A time step of $0.0003\,\mathrm{s}$ was used, resulting in an angular step of $4°$. A maximum internal iteration number of 30 was defined to ensure the lowest residuals possible while not compromising simulation time.

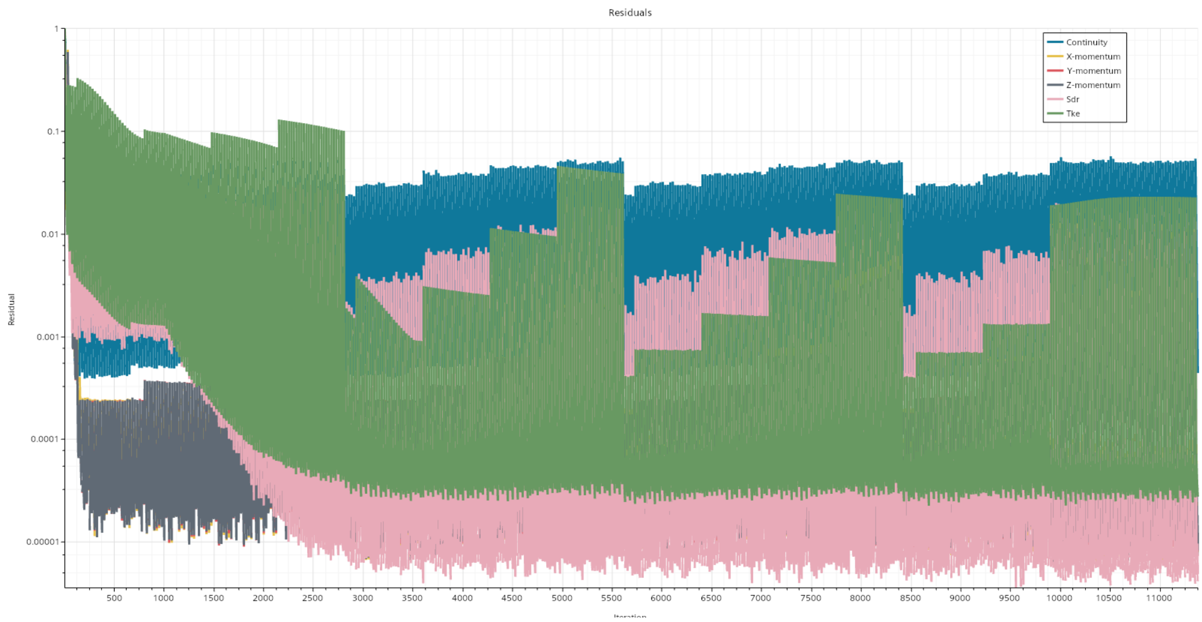

Figure 5.19: Residual evolution for simulation after 12000 iterations.

Residuals in an unsteady RANS simulation increase when a time step is performed and lower with internal iterations. The residuals presented in Figure 5.19 are representative of the evolution of the continuity, X, Y and Z momentum and the turbulence residuals given by the normalised RMS of the absolute error for the variables in each cell. The normalisation is performed by the maximum error value present in the first 5 iterations. The residuals obtained were quite high but due to time constraints, no further attempt to improve the simulation convergence was performed.

Nonetheless, integral quantities tend to a periodic solution with constant mean and amplitude after the first rotation of the propeller was performed as can be observed in Figure 5.20, after that the values oscillate around of a mean value. This mean value was then used for further calculations. Oscillations were within $2\,\%$ of the average value, this could be due to the high number of blades used in the design.

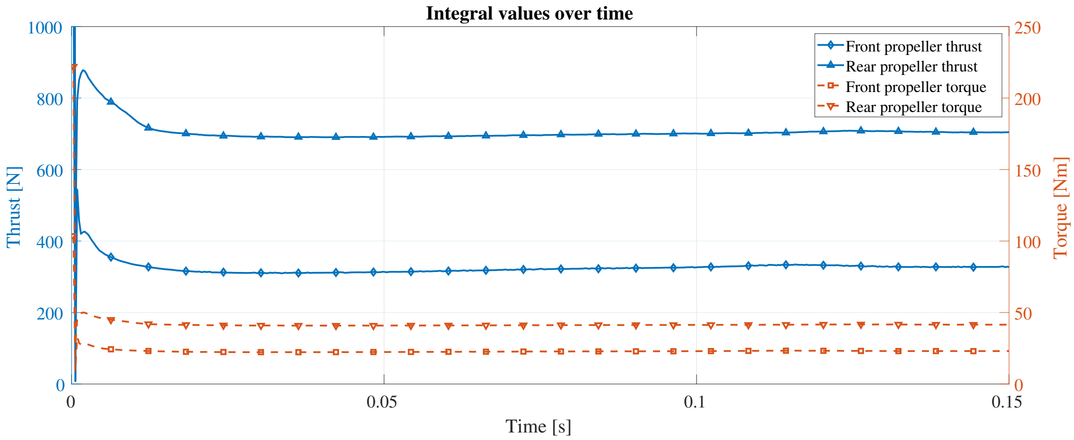

Figure 5.20: Integral values over time.

Figure 5.21 compiles the results of the CFD results with results from OpenProp.

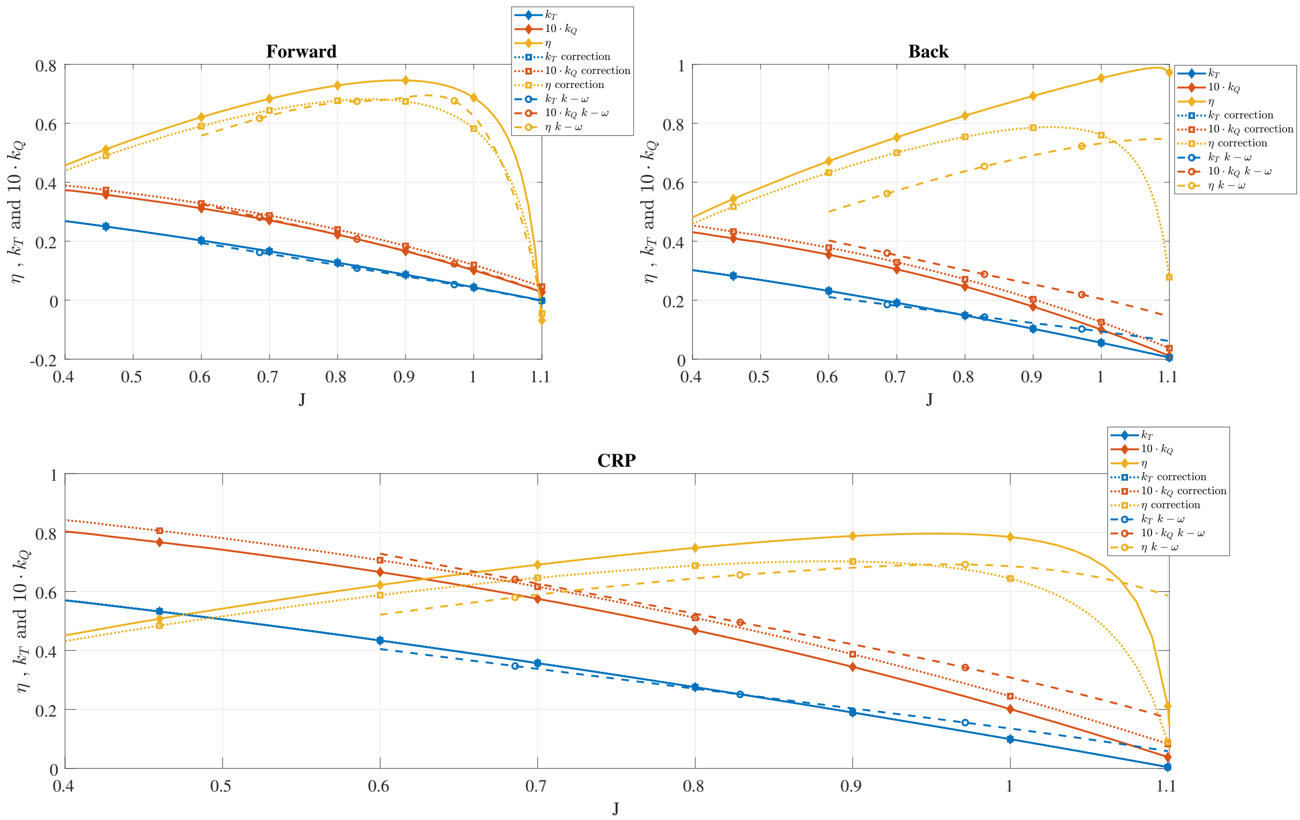

Figure 5.21: Results of mean propeller force coefficients comparison including CFD results in dashed lines with circle markers, and OpenProp results with and without drag coefficient correction.

The solid lines represent the results from OpenProp with a constant coefficient of drag of 0.0008, the dotted lines represent the OpenProp solution using the coefficient of drag calculated using a simplified function based on the geometry, the Reynolds number and the International Towing Tank Conference (ITTC) (1957) coefficient of friction line [63]. The results show a good match of K_T and K_Q of the front propeller for the original OpenProp and the CFD solution. With a maximum deviation of $2\,\%$ for the K_Q and $1.2\,\%$ for the K_T, this translates to a maximum deviation of $4\,\%$ in the efficiency. The OpenProp solution that uses the ITTC overestimates the drag and thus the torque, this results in a better correlation of the efficiency to the CFD results. The deviation of the efficiency, for the most part, is less than $1\,\%$ deviating more at the cruise advance coefficient.

For the rear propeller, the deviations are greater, around $17\,\%$ between the original OpenProp and the CFD solution. The slope of k_T obtained through CFD is different to the OpenProp solution, this could be explained by the way that the induced velocities are calculated since the approach used in this work neglects the mutual induced velocities. The slope of k_Q of the rear propeller is also different and diverges more at higher advance ratios.

Although the results of the CFD simulations do deviate quite a bit from the values predicted by the modified OpenProp code, the necessary thrust for the boat is produced and the torque increased by $10\,\mathrm{N\,m}$ at the cruise condition and $15\,\mathrm{N\,m}$ at the takeoff condition, which the motor can handle.

5.3 MPS Mechanical Design

The mechanical project of the MPS is an important part, as it takes the geometry obtained through the optimisation routines and applies mechanical and manufacturing constraints to arrive at a final design that is ready for production. The motors and propellers must be able to withstand $5000\,\mathrm{RPM}$ in case of overspeed fault and withstand at least $150\,\mathrm{N\,m}$ of peak torque generation. A mechanical failsafe was implemented in case the propellers collided with external objects, protecting the shaft and motors.

5.3.1 Rotor and Stator Assembly

To start, the analysis of the shaft and rotor was performed to ensure that the motor could handle the torque during operation. Further analysis regarding the magnet's mechanical behaviour was also done. The stator practically did not change during the process: the only alteration performed was some through holes were threaded rods passed through to mount the bearing casings. This was done because one of the motor requirements is to have the capacity to be disassembled for maintenance.

The final rotor geometry is presented in Figure 5.22.

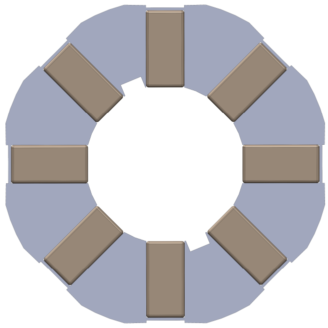

Figure 5.22: Final rotor geometry of the electric motors.

As the rotor spins the PMs experiences a centripetal force calculated by:

$$F = m \cdot a_c = m\frac{v^2}{r} = m\frac{(w \cdot r)^2}{r} = m \cdot w^2 \cdot r = 0.209 \cdot 5483.114 = 1145.97\,\mathrm{N}, \tag{5.7}$$

where F is the centripetal force, m, is the mass of the magnet, a_c is the centripetal acceleration of the magnet, r is the distance from the magnet's center of gravity to the center of rotation and w is the angular velocity. This force is applied to the magnet bridge, as seen in Figure 5.23. Considering the magnet bridge $a_{bridge} = 0.5\,\mathrm{mm}$ and the motor stack length of $290.15\,\mathrm{mm}$, the area perpendicular to the load case is defined by Equation 5.8 and the forces acting in that area are shown in Equation 5.7:

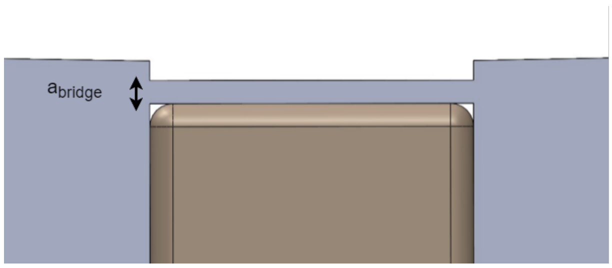

Figure 5.23: Magnet bridge of rotor.

$$A_{bridge} = 0.5\,\mathrm{mm} \cdot 290.15\,\mathrm{mm} = 145.075\,\mathrm{mm}^2. \tag{5.8}$$

The tensile stress is given by Equation 5.9:

$$\tau = \frac{F}{A} = \frac{1145.97}{145.075} = 7.8\,\mathrm{MPa}, \tag{5.9}$$

the stress induced in the magnet bridge produced by the magnet acceleration is $7.8\,\mathrm{MPa}$ which is lower than the $NO15$ yield stress of $370\,\mathrm{MPa}$ [17]. This results in a factor of safety of 47.4, assuring that no failure will occur.

To fit the rotor to the shaft a shrink fit is proposed. Shrink fit is a semi-permanent way of assembling concentric assemblies that can transmit large amounts of torque with the use of high-pressure contact areas at the interface of the components. By using a shrink fit the mechanical stresses on the rotor core and shaft are minimised and the assembly can be taken apart if necessary. Solid materials expand with temperature, this relation is given by the coefficient of linear thermal expansion. Since the PMs must not exceed their maximum demagnetisation temperature a combination of shaft cooling and rotor heating is required. Cooling the shaft with solid carbon dioxide ($-78\,^{\circ}\mathrm{C}$ at normal atmospheric pressure [64]) and heating the rotor to $60\,^{\circ}\mathrm{C}$ a temperature differential of $138\,^{\circ}\mathrm{C}$ is achieved. The maximum interference can be calculated by:

$$\Delta T = \frac{1}{\alpha_L}\frac{\delta}{d}, \tag{5.10}$$

where α_L is the coefficient of linear thermal expansion, ΔT is the temperature differential and δ is the interference between the shaft and rotor. This results in an interference of $\delta = 0.0447\,\mathrm{mm}$ which was rounded up to $0.05\,\mathrm{mm}$. Equation 5.11 determines the pressure of the shrinkage fit [65]:

$$P = \frac{\delta}{\frac{d}{E_r}(\frac{d_o^2+d^2}{d_o^2-d^2}+\nu_r)+\frac{d}{E_s}(\frac{d^2+d_i^2}{d^2-d_i^2}+\nu_s)}, \tag{5.11}$$

where:

- d is the nominal contact diameter;
- d_i is the internal shaft diameter;
- E_s is the elastic modulus of the shaft;
- E_r is the elastic modulus of the rotor;
- ν_s is the Poisson's ratio of the shaft;
- ν_r is the Poisson's ratio of the rotor;
- P is the interference pressure.

The maximum allowable torque for a given interference is given by:

$$T = F\frac{d}{2} = P \cdot A\frac{d}{2} = \frac{P \cdot d^2 \cdot \pi \cdot L \cdot \eta_s}{2}, \tag{5.12}$$

where L is the length of the contact, F is the maximum allowed tangential force and η_s is the coefficient of static friction. The resulting Torque is $7695.84\,\mathrm{N\,m}$ considering a coefficient of friction of 0.7 [66]. Considering that this method requires precise machining to further ensure a good connection between the shaft and the rotor two keys are used, using a calculation tool provided by GWJ Technology (available at [67]) that follows the norm DIN 6892[1].

[1]This standard establishes principles of design and calculation for parallel key connections whose parts are made of metallic materials. This standard applies primarily to parallel key connections used in machines [68]

To fit the stator into the motor housing the same shrink-fit method was applied, since the heated part is the outer motor casing, the heating can be much greater achieving higher interference. In Table 5.8 the interferences, temperature deltas and maximum allowable torque values are presented.

Table 5.8: Shrink fit interferences, temperature deltas and maximum allowable torque results.

	Interference δ [mm]	ΔT [°C]	Torque [N m]
Shaft/rotor interface	0.05	138	7695.84
Stator/Torpedo interface	0.4	140	71565.21

5.3.2 Splined Shaft

Mounting the propellers to the motor shafts is critical to the design process, as the fitment needs to be easy to disassemble but also withstand the demanding torque requirements. Splined shafts are used to mount propellers in most commercially available propellers. Using the standard DIN 5480[2], Figure 5.24 shows the obtained geometry for the front and rear propeller shafts.

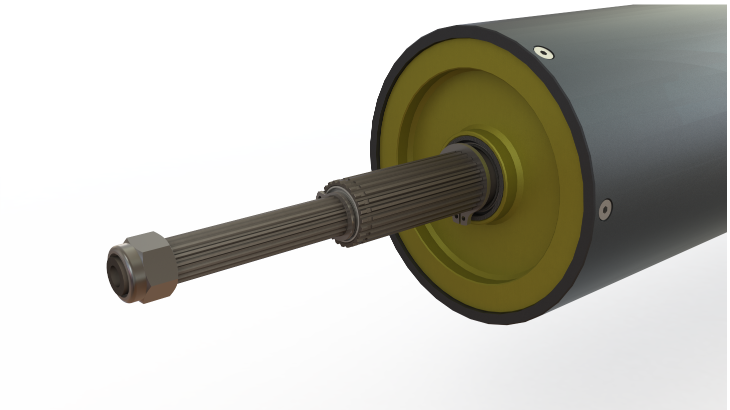

Figure 5.24: 3D render of the front and rear shaft splines.

Table 5.9 provides detailed information about the shaft geometry and the loads and safety factors, F_s. The calculations performed by the tool follow the procedure given in [70].

Table 5.9: Geometry data and factor of safety results for the Spline sizing.

	Reference Diameter [mm]	Modulus [mm]	Number of Teeth	F_s Shaft	F_s Hub	Nominal Torque Considered [N m]	Maximum Load Considered [N m]
Front Spline	25	1	24	6.06	15.27	120	200
Rear Spline	15	0.8	17	3.83	5.08	120	200

For added safety, a designed fail point is implemented into the propeller hub. The hub is comprised of two parts, the splined inner hub, made from brass, and the propeller as seen in Figure 5.25.

[2]This series of standards deals with involute splines and interacting involute splines in the ranges module 0.5 to 10, with the number of teeth ranging from 6 to 82 and a pressure angle of $30°$ [69].

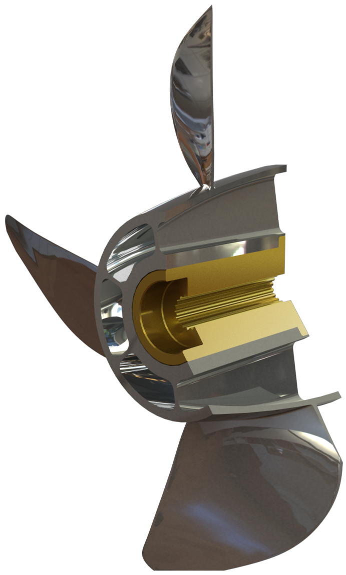

Figure 5.25: 3D render of the rear propeller hub.

The two parts are press fitted with an interference of $0.035\,\mathrm{mm}$ resulting in a transmission torque of $214.1\,\mathrm{N\,m}$. Detailed calculations are given in Annexe B.

5.3.3 Bearing Selection

For the bearing selection bearings from SKF were chosen since the team has a sponsorship that provides these bearings. Careful selection was made to ensure all rotational speeds were within the limits. For the axial load bearings the single-row tapered roller bearing 32005 X was chosen [71]. To stabilise the long shaft of the front motor that connects to the rear propeller a pair of single-row needle roller and cage assemblies were chosen [72]. For additional stability, a pair of stainless steel deep groove ball bearings with integral sealing W 61702-2RS1 were chosen to minimise oscillations between the two shafts [73]. Figure 5.26 presents the locations of the bearings in the assembly.

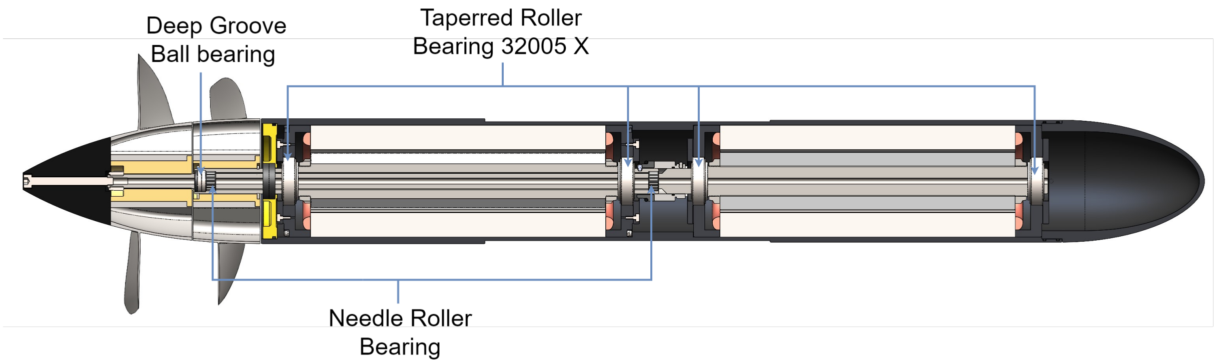

Figure 5.26: Locations of selected bearings.

Table 5.10 contains all bearings used for this project, detailing their maximum rotational speed, load-carrying capacity and dimensions.

Table 5.10: Bearing selection size data and load limits.

	ID [mm]	**OD** [mm]	**Width** [mm]	**Limit Speed** [$\mathrm{r\,min^{-1}}$]	**Basic Dynamic Loading Rating** [kN]
Taperred Roller Bearing 32005 X	25	47	15	14000	33.2
Deep Groove Roller Bearing W 61702-2RS1	15	21	4	19000	0.527
Needle Roller Bearing K 15X19X10	15	19	10	28000	7.21

5.3.4 Sealing

To ensure no water gets into the assembly a careful selection of sealing components needs to be made. For static connections such as the front and rear covers of the torpedo casing o-rings were selected using the Parker tool [74]. For rotational connections SKF rotary seals are used, datasheets of the seals are given in annexe C. The surface that is in contact with the seals needs to have a surface roughness of $0.05 < R_a < 0.2\,\mathrm{\mu m}$. The stationary groove surface requires a surface roughness less than $3\,\mathrm{\mu m}$ [75]. To ensure that no fluid gets in from in between the shafts a mechanical seal is implemented. A basic mechanical seal contains three sealing points. The stationary part of the seal is fitted to the pump housing with a static seal – this may be sealed with an o-ring or gasket clamped between the stationary part and the pump housing. The rotary portion of the seal is sealed onto the shaft usually with an O-ring. This sealing point can also be regarded as static as this part of the seal rotates with the shaft. One part of the seal, either static or rotary portion, is always resiliently mounted and spring loaded to accommodate any small shaft deflections, shaft movement due to bearing tolerances and out-of-perpendicular alignment due to manufacturing tolerances [76].

6
Conclusions

Conclusions

The main objective of this thesis was to design and optimise a propulsion system for the TSB project and to address the need for robust and efficient propulsion systems in a rapidly evolving marine sector. To face this problem, a review of different propulsion methods and the different electrical motors available was made to arrive at a pairing of both that would satisfy the needs of the project. An overview of the materials and layouts was given and the most appropriate were selected and used for the design process. The obtained solutions of the optimisation process are presented and a deeper analysis of the necessary changes needed to implement the final system was performed. Electromagnetic, thermal and hydrodynamical simulations were performed to evaluate the performance of the solutions and verify the results.

The mechanical design of the system is also explored, tying both parts together and preparing the system to be manufacturable and robust enough for the demanding races it will face while in use. The mechanical joints were analysed, a bearing selection was performed and a mechanical failsafe was implemented in order to protect the motors from a torque spike in case of a collision of the propellers with an external object.

The MPS will be implemented in the next prototype of the project, SG01, and hopefully bring the team a reliable propulsion that can be further improved with the know-how created in this work.

The design process can be considered effective in reducing the time needed to develop such a system from the ground up. The in-house development of the full propulsion system gives the team more control over the behaviour of the vessel and doesn't compromise on the applications possible for commercially available propulsion systems. The shortcomings of the numerical analysis of the propellers are clear, further improvements to the rear propeller performance are necessary to reduce the $17\,\%$ deviation in efficiency from the CFD results.

The CFD methods implemented in this thesis help to analyse the developed propeller geometries for not only the CRP of SG01 but also future prototypes. The team can have greater confidence in their designs while also reducing the development time with the GA routine.

The CFD routines implemented in this work can be further used to analyse the cavitation of the propellers and verify the method used in this thesis. This leads to the future work that can be developed based on this thesis.

6.1 Future Work

In what concerns the future work related to the MPS, the suggestions can be divided into four distinct categories:

- The construction and implementation of the MPS;
- Testing the impact of using other material choices for the electric motor;
- Further CFD analysis of the CRP system with regards to cavitation occurrence and its acoustic profile;
- Testing both the electric motor and the propellers in a laboratory environment to verify the theoretical results.

For the construction and implementation of the MPS for the prototype a partnership with a company is recommended since the construction of two electric motors is a delicate operation and must be done in a controlled environment. For testing the impact of different material choices on the performance of the electric motor, choices of the core and PM material are the ones that could provide the biggest impact.

Due to time restrictions, the CFD simulations performed in this work were limited and can be further explored. Cavitation prediction and acoustic profiling are the main studies to be performed but an exploration of different rotational speeds for the propellers can be performed to study the interaction between the two propellers.

Finally, laboratory tests can be performed for both the electric motor and propellers to validate the results presented in this work and further expand the team's knowledge on the topic.

Bibliography

[1] "Eu maritime transport: first environmental impact report acknowledges good progress towards sustainability and confirms that more effort is needed to prepare for rising demand — european environment agency," www.eea.europa.eu, 09 2021. [Online]. Available: https://www.eea.europa.eu/highlights/eu-maritime-transport-first-environmental (Accessed on 2023-05-18).

[2] E. Observer, "About Energy Observer," Energy Observer. [Online]. Available: https://www.energy-observer.org/about (Accessed on 2023-05-26).

[3] B. P. Epps, M. J. Stanway, and R. Kimball, "OpenProp: An Open-source Design Tool for Propellers and Turbines," 09 2009. [Online]. Available: https://transistor-man.com/files/cnc_prop/Epps_OpenProp_SNAME_090420.pdf (Accessed on 2023-09-13).

[4] M. Doppelbauer, "Institute - History - Jacobi's first real electric motor," www.eti.kit.edu, 08 2018. [Online]. Available: https://www.eti.kit.edu/english/1382.php (Accessed on 2023-04-29).

[5] "Electric Boats - Engineering and Technology History Wiki," Ethw.org, 2013. [Online]. Available: https://ethw.org/Electric_Boats (Accessed on 2023-04-29).

[6] F. Allavena, "History - MEBC," Monaco Energy Boat Challenge, 05 2021. [Online]. Available: https://energyboatchallenge.com/en/history/ (Accessed on 2023-04-29).

[7] E. Union, "CE marking – obtaining the certificate, EU requirements," Your Europe, 08 2023. [Online]. Available: https://europa.eu/youreurope/business/product-requirements/labels-markings/ce-marking/index_en.htm#abbr-ID0E1 (Accessed on 2023-10-15).

[8] W. O'neil, "Hydrofoil Ship Design - W Neill," Scribd, 2003. [Online]. Available: https://www.scribd.com/document/238942622/Hydrofoil-Ship-Design-W-Neill (Accessed on 2023-05-30).

[9] W. Tong, *Mechanical design of electric motors*. Crc Press, Taylor and Francis Group, 2017.

[10] S. J. Chapman, *Electric machinery fundamentals*, 4th ed. New Delhi :: McGraw Hill Education (India) Pvt. Ltd.,, 2010., includes index.

[11] J. Wang, J. Wu, C. Gan, and Q. Sun, "Comparative study of flux-weakening control methods for PMSM drive over wide speed range," *2016 19th International Conference on Electrical Machines and Systems (ICEMS)*, pp. 1–6, 2016.

[12] D. Oliveira, "Electromagnetic Design of a PM Synchronous Generator for a 20 kW Ultra-low Head Hydro Turbine," 05 2017. [Online]. Available: https://fenix.tecnico.ulisboa.pt/downloadFile/1689244997257526/dissertacao.pdf (Accessed on 2023-09-13).

[13] J. Sarrico, "Design and Implementation of a 20 kW, 12000 RPM Permanent Magnet Synchronous Motor for the IST Formula Student Powertrain," 11 2017. [Online]. Available: https://fenix.tecnico.ulisboa.pt/downloadFile/281870113704247/paper_MJF.pdf (Accessed on 2023-09-13).

[14] P. P. C. Bhagubai, L. F. D. Bucho, J. F. P. Fernandes, and P. J. Costa Branco, "Optimal Design of an Interior Permanent Magnet Synchronous Motor with Cobalt Iron Core," *Energies*, vol. 15, p. 2882, 04 2022.

[15] H. Ahn, H.-J. Park, C.-H. Kim, and H. Lee, "A Review of State-of-the-art Techniques for PMSM Parameter Identification," *Journal of Electrical Engineering and Technology*, vol. 15, pp. 1177–1187, 03 2020.

[16] "Powercore A — thyssenkrupp Steel," thyssenkrupp. [Online]. Available: https://www.thyssenkrupp-steel.com/en/products/electrical-steel/electrical-steel-non-grain-oriented/powercore-a/powercore-a.html (Accessed on 2023-06-11).

[17] T. Steel, "NO15-1230N Data sheet thin non-oriented electrical steel," 03 2019. [Online]. Available: https://www.tatasteeleurope.com/sites/default/files/tata-steel-hi-lite-electrical-steel-no15-1230n-datasheet-en.pdf (Accessed on 2023-09-23).

[18] "Hyperco50 data sheet," Carpenter Electrification, 2022. [Online]. Available: https://www.carpenterelectrification.com/hubfs/Resources/Datasheets/Hiperco_50_Alloy_(E200).pdf (Accessed on 2023-06-11).

[19] E. Tutorials, "Magnetic Hysteresis Loop including the B-H Curve," Basic Electronics Tutorials, 02 2018. [Online]. Available: https://www.electronics-tutorials.ws/electromagnetism/magnetic-hysteresis.html (Accessed on 2023-09-26).

[20] J. Gieras, *PERMANENT MAGNET MOTOR TECHNOLOGY: DESIGN AND APPLICATIONS*. CRC Press, 01 2010.

[21] M. Coey and S. S. Parkin, *Handbook of Magnetism and Magnetic Materials*. Springer, 11 2021.

[22] "Neodymium Iron Boron Magnet Catalog," Arnold Magnetic Technologies, 2021. [Online]. Available: https://www.arnoldmagnetics.com/wp-content/uploads/2019/06/Arnold-Neo-Catalog.pdf (Accessed on 2023-06-11).

[23] "Alnico permanent magnets," Arnold Magnet Technologies, 02 2003. [Online]. Available: https://www.arnoldmagnetics.com/wp-content/uploads/2017/10/Sintered-Alnico-Permanent-Magnets-101117-1.pdf (Accessed on 2023-06-11).

[24] "RECOMA: Range of SmCo Materials," Arnold Magnet Technologies, 2014. [Online]. Available: https://www.arnoldmagnetics.com/wp-content/uploads/2017/10/Recoma-Combined-160301.pdf (Accessed on 2023-06-11).

[25] "Samarium Cobalt Magnets in Electric Machinery Industry," Stanford Magnets, 04 2019. [Online]. Available: https://www.stanfordmagnets.com/samarium-cobalt-magnets-in-electric-machinery-industry.html (Accessed on 2023-05-26).

[26] "How to Avoid Neodymium Magnet Corrosion?" Stanford Magnets, 06 2020. [Online]. Available: https://www.stanfordmagnets.com/how-to-avoid-neodymium-magnet-corrosion.html (Accessed on 2023-05-26).

[27] "Matweb - the online materials information resource," www.matweb.com. [Online]. Available: https://www.matweb.com

[28] D. K. Brown, "Sir Francis Pettit," *Oxford Dictionary of National Biography*, 12 2004.

[29] A. F. Molland, S. R. Turnock, and D. A. Hudson, "Propulsor Types," *Cambridge University*, pp. 264–276, 08 2017, (Accessed on 2023-07-12).

[30] "Controllable pitch propeller," www.kongsberg.com. [Online]. Available: https://www.kongsberg.com/maritime/products/propulsors-and-propulsion-systems/propellers/propeller-products/controllable-pitch-propeller/ (Accessed on 2023-09-12).

[31] "Supermarine Spitfire Mk XIV prototype JF321," www.worldwarphotos.info, 2013. [Online]. Available: https://www.worldwarphotos.info/gallery/uk/raf/spitfire2/spitfire-mk-xiv-prototype-jf321/ (Accessed on 2023-08-30).

[32] V. Štorch, "Verified Unsteady Model for Analysis of ContraRotating Propeller Aerodynamics," 2017. [Online]. Available: https://dspace.cvut.cz/bitstream/handle/10467/75503/F2-D-2018-Storch-Vit-priloha-Storch_thesis_statement_PRINT.pdf?sequence=-1 (Accessed on 2023-07-12).

[33] “Comparative properties of propeller alloys,” Stone Marine propulsion, 2021. [Online]. Available: https://stonemarinepropulsion.com/wp-content/uploads/2021/08/Comparing-Alloys-NL.pdf (Accessed on 2023-07-14).

[34] “ReFRESCO — MARIN,” www.marin.nl. [Online]. Available: https://www.marin.nl/en/facilities-and-tools/software/refresco (Accessed on 2023-09-12).

[35] M. Drela, “Xfoil - Subsonic Airfoil Development System,” Mit.edu, 2013. [Online]. Available: https://web.mit.edu/drela/Public/web/xfoil/ (Accessed on 2023-09-07).

[36] S. F. Hoerner, *Fluid-dynamic Drag*, 2nd ed. Liselotte A. Hoerner, 01 1965, pp. 8 – 11 to 12.

[37] T. , “XFLR5,” www.xflr5.tech, 01 2021. [Online]. Available: https://www.xflr5.tech/xflr5.htm (Accessed on 2023-09-07).

[38] N. Drakos, “Unified Propulsion 4 - Thermodynamics and Propulsion,” ocw.mit.edu, 2002. [Online]. Available: https://ocw.mit.edu/ans7870/16/16.unified/propulsionS04/UnifiedPropulsion4/UnifiedPropulsion4.htm (Accessed on 2023-09-07).

[39] I. ABBOTT, *Theory of Wing Sections, Including a Summary of Airfoil Data.*, 1st ed. Dover Publications, 1959. [Online]. Available: https://www3.nd.edu/~ame40431/AME20211_2021/Other/AbbottDoenhoff_TheoryOfWingSectionsIncludingASummaryOfAirfoilData.pdf (Accessed on 2023-09-03).

[40] F. M. White, *Fluid Mechanics*, fourth edition ed. McGraw-Hill, 1999.

[41] S. F. Hoerner, *Fluid-dynamic Drag*, 2nd ed. Liselotte A. Hoerner, 01 1965, pp. 11–26.

[42] S. F. Hoerner, *Fluid-dynamic Drag*, 2nd ed. Liselotte A. Hoerner, 01 1965, pp. 3 – 12.

[43] “Lecture on finite wings - Aerodynamics.” [Online]. Available: https://people.clarkson.edu/~pmarzocc/AE429/AE-429-4.pdf (Accessed on 2023-10-21).

[44] M. Abdel-Basset, L. Abdel-Fatah, and A. K. Sangaiah, “Metaheuristic Algorithms: A Comprehensive Review,” *Computational Intelligence for Multimedia Big Data on the Cloud with Engineering Applications*, pp. 185–231, 2018. [Online]. Available: https://doi.org/10.1016/B978-0-12-813314-9.00010-4 (Accessed on 2023-10-11).

[45] H. Sayyaadi, *Optimization Basics*, 01 2020, pp. 327–430. [Online]. Available: https://www.sciencedirect.com/book/9780128166567/modeling-assessment-and-optimization-of-energy-systems (Accessed on 2023-09-11).

[46] M. W. Mkaouer and M. Kessentini, “Model Transformation Using Multiobjective Optimization,” *Advances in Computers*, vol. 92, pp. 161–202, 01 2014, (Accessed on 2023-09-12).

[47] J. A. C. F. de Campos, “Lecture notes in Resistance and Propulsion,” 2021-2022.

[48] J. Carlton, *Marine Propellers and Propulsion*. Butterworth-Heinemann, 11 2018. [Online]. Available: https://maritimeexpert.files.wordpress.com/2018/03/marine-propellers-and-propulsion-carlton.pdf (Accessed on 2023-09-13).

[49] E. Kravitz, “Analysis and Experiments for Contra-Rotating Propeller,” 05 2011. [Online]. Available: https://core.ac.uk/download/pdf/4430009.pdf (Accessed on 2023-09-13).

[50] Davidhv22, “Cavitación,” Wikimedia Commons, 06 2011. [Online]. Available: https://commons.wikimedia.org/w/index.php?curid=15474876 (Accessed on 2023-09-13).

[51] G. Abad, *Power electronics and electric drives for traction applications*. Wiley, 2017.

[52] “Matweb - the online materials information resource- copper,” www.matweb.com. [Online]. Available: https://www.matweb.com/search/DataSheet.aspx?MatGUID=9aebe83845c04c1db5126fada6f76f7e

[53] DuPont, “DuPont Nomex 410,” 2016. [Online]. Available: https://www.dupont.com/content/dam/dupont/amer/us/en/safety/public/documents/en/DPT16_21668_Nomex_410_Tech_Data_Sheet_me03_REFERENCE.pdf (Accessed on 2023-10-17).

[54] L. Marackova, V. Melcova, J. Samek, and O. Zmeskal, “Thermal Properties of Electro Insulating Paper,” *Materials Science Forum*, vol. 955, pp. 25–30, 05 2019, (Accessed on 2022-11-04).

[55] E. Jih, K. Chen, T. Abraham, and V. Siddapureddy, “Thermal Management for the HEV Liquid-Cooled Electric Machine,” *SAE technical paper series*, 05 2001, (Accessed on 2023-10-17).

[56] P. Cunha, “Parametric Design of an End-winding Cooling Method for a Permanent Magnet Synchronous Motor,” pp. 41 – 45; 53, 10 2022.

[57] W. Frey, “Modeling Natural and Forced Convection in COMSOL Multiphysics,” COMSOL, 04 2017. [Online]. Available: https://www.comsol.com/blogs/modeling-natural-and-forced-convection-in-comsol-multiphysics/ (Accessed on 2023-10-24).

[58] C. Ruoff, “A closer look at torque ripple - minimizing its effects on electric machines,” Charged EVs, 09 2015. [Online]. Available: https://chargedevs.com/features/minimization-of-torque-ripple-is-

important-for-motors-in-many-applications-because-it-is-one-of-the-main-causes-of-vibration/#:~:text=be%20generally%20acceptable%3F- (Accessed on 2023-10-24).

[59] ASTM, "Standard Specification for Standard Nominal Diameters and Cross-Sectional Areas of AWG Sizes of Solid Round Wires Used as Electrical Conductors," www.astm.org, 10 2018. [Online]. Available: https://www.astm.org/b0258-18.html (Accessed on 2023-10-14).

[60] M. Ceze, M. Hayashi, and E. Volpe, "A Study of the CST Parameterization Characteristics," *27th AIAA Applied Aerodynamics Conference*, 06 2009. [Online]. Available: http://www-personal.umich.edu/~mceze/shared_papers/Ceze_etal_AA2009.pdf (Accessed on 2023-01-07).

[61] X. Peng, L. Zhang, B.-l. Wang, L. Xu, M. Song, Y. Cao, Y. Liu, F.-w. Hong, and K. Yan, "Study of tip vortex cavitation inception and vortex singing," *Journal of Hydrodynamics*, vol. 31, pp. 1170–1177, 12 2019, (Accessed on 2023-10-06).

[62] Siemens, "Simcenter STAR-CCM+," Siemens Digital Industries Software. [Online]. Available: https://plm.sw.siemens.com/en-US/simcenter/fluids-thermal-simulation/star-ccm/ (Accessed on 2023-10-19).

[63] J. F. Campos, "Formulação de um Método de Elementos de Fronteira para o cálculo do escoamento potencial incompressível em hélices propulsores," Ph.D. dissertation, 1996.

[64] C. G. Association, "Carbon Dioxide and Dry Ice Fact Sheet," Compressed Gas Association. [Online]. Available: https://www.cganet.com/carbon-dioxide-dry-ice-fact-sheet/#:~:text=Solid%20carbon%20dioxide%20%E2%80%93%20also%20known (Accessed on 2023-10-08).

[65] R. Budynas and K. Nisbett, *Shigleys Mechanical Engineering Design*, 8th ed. McGraw-Hill Science/Engineering/Math, 2008. [Online]. Available: https://docs.google.com/file/d/0B7gVyEHYuxX4UWgtRjdzZ1F5LVU/preview?resourcekey=0-nEBu-yzq4wN8FtQYIcz1Wg (Accessed on 2023-10-08).

[66] J. F. Sullivan, *Technical Physics*. John Wiley and Sons, 1988.

[67] G. Technologies, "GWJ eAssistant: Web-based calculation software for mechanical engineering," www.eassistant.eu. [Online]. Available: https://www.eassistant.eu/en/home.html (Accessed on 2023-10-08).

[68] NORMADOC, "DIN 6892," Normadoc. [Online]. Available: https://www.normadoc.com/english/din-6892-2012-08.html (Accessed on 2023-10-08).

[69] D. D. I. für Normung, “Splined connections with involute splines based on reference diameters - DIN 5480,” 03 2006. [Online]. Available: https://d2t1xqejof9utc.cloudfront.net/files/209189/Spline_DIN_5480.pdf?1604497003#:~:text=The%20DIN%205480%20series%20of (Accessed on 2023-10-08).

[70] G. Niemann, H. Winter, and B.-R. Höhn, *Maschinenelemente*. Springer-Verlag, 12 2013.

[71] SKF, “32005 X - Single row tapered roller bearing,” Skf.com, 2023. [Online]. Available: https://www.skf.com/group/products/rolling-bearings/roller-bearings/tapered-roller-bearings/single-row-tapered-roller-bearings/productid-32005%20X (Accessed on 2023-10-13).

[72] SKF, “K 15X19X10 - Single row needle roller and cage assembly,” Skf.com, 2023. [Online]. Available: https://www.skf.com/group/products/rolling-bearings/roller-bearings/needle-roller-bearings/needle-roller-and-cage-assemblies/productid-K%2015X19X10 (Accessed on 2023-10-13).

[73] SKF, “W 61702-2RS1 - Stainless steel deep groove ball bearing with integral sealing,” www.skf.com. [Online]. Available: https://www.skf.com/group/products/rolling-bearings/ball-bearings/deep-groove-ball-bearings/productid-W%2061702-2RS1 (Accessed on 2023-10-13).

[74] Parker, “Parker O-Ring Selector.” [Online]. Available: https://divapps.parker.com/divapps/oring/ORingSelector/?LangID=EN&lang=en&cntry=us/17061&LangSrcType=local (Accessed on 2023-10-14).

[75] SKF, “Industrial shaft seals catalog,” skf.com. [Online]. Available: https://cdn.skfmediahub.skf.com/api/public/09433a92e9164581/pdf_preview_medium/09433a92e9164581_pdf_preview_medium.pdf (Accessed on 2023-10-14).

[76] AESSEAL, “What is a Mechanical seal?” Aesseal.com, 07 2019. [Online]. Available: https://www.aesseal.com/en/resources/academy/what-is-a-mechanical-seal (Accessed on 2023-10-14).

[77] B. Etkin, *Dynamics of flight : stability and control.*, 3rd ed. JOHN WILEY and SONS, INC, 1995.

[78] A. H. Slocum, *Precision Machine Design*. Society of Manufacturing Engineers, 1995.

A Detailed Boat Angle Calculations

The trim calculations are performed as follows:

If $V > V_{takeoff}$, flying condition, the following stability matrix equation is resolved,

$$\begin{bmatrix} 1 & 1 \\ -X_{FW} & X_{RW} \end{bmatrix} = \begin{bmatrix} L_{FW} \\ L_{RW} \end{bmatrix} \cdot \begin{bmatrix} m \cdot g \\ -cm_{FW} \cdot q \cdot S_{FW} \cdot MAC_{FW} \end{bmatrix}, \tag{A.1}$$

where X_{FW} and X_{RW} are the distances from the front and aft hydrofoil to the centre of mass as shown in Figure 3.3. L_{FW} and L_{RW} are the lift forces produced by the front and aft hydrofoils respectively. m is the mass of the vessel, g is the gravitational constant, cm_{FW} is the moment coefficient of the front hydrofoil, S_{FW} is the planform area of the front hydrofoil, MAC_{FW} is the mean aerodynamic chord of the front hydrofoil, and q is the dynamic pressure. This equation comes from the force and moment balance around the centre of mass.

The 3D lift coefficients are calculated by adimentionalising the lift of the front and aft hydrofoils using the area of the respective wings:

$$CL_{FW} = \frac{L_{FW}}{q * S}, \tag{A.2}$$

$$CL_t = \frac{L_{RW}}{q * S_t}, \tag{A.3}$$

these coefficients need to be converted to the 2D coefficients in order to be used by the Xfoil routine. The 2D coefficients are obtained by using Equation 3.17. Next, Xfoil routines are used to determine the AoA of both front and aft hydrofoils. With these angles, the pitch of the boat can be determined by:

$$Pitch = \alpha_{frontwing} - \alpha_{FW_{fixed}}, \tag{A.4}$$

where $\alpha_{frontwing}$ is the apparent AoA of the front wing and $\alpha_{FW_{fixed}}$ is the fixed angle the wing is mounted on to the boat. With the pitch angle of the boat the aft hydrofoil AoA can be determined:

$$\alpha_{tail_{mech}} = \alpha_{tail} + \epsilon - Pitch, \tag{A.5}$$

where $\alpha_{tail_{mech}}$ is the actual AoA of the aft hydrofoil concerning the boat horizontal plane, α_{tail} is the apparent AoA of the aft hydrofoil, ϵ is the downwash that is calculated by:

$$\epsilon = \alpha_{frontwing} * (1 - \epsilon_\alpha) + \epsilon_0, \tag{A.6}$$

where ϵ_α and ϵ_0 are the intercept and slope constants of the downwash linear function with regards to the front hydrofoil AoA. The constants are taken from [77].

If $V < V_{takeoff}$, before takeoff, then the AoA of the front hydrofoil is known by computing the pitch of the boat using the interpolation obtained from the data of Table 3.1 and the fixed AoA of the front hydrofoil:

$$\alpha_{frontwing} = 5 + 0.0805 \cdot e^{0.7402 \cdot V}. \quad \text{(A.7)}$$

The aft hydrofoil angles are then calculated the same way as for the flying condition.

In either condition, the calculated angles are used to calculate the drag of the boat and hydrofoil system using the equation detailed in Chapter 3.1.1.

B Detailed Press Fit Calculations

Starting with the equation that gives the interference pressure as a result of diametrical interference:

$$P = \frac{\delta}{\frac{d}{E_r}(\frac{d_o^2+d^2}{d_o^2-d^2}+\nu_r)+\frac{d}{E_s}(\frac{d^2+d_i^2}{d^2-d_i^2}+\nu_s)}, \tag{B.1}$$

the pressure gives the radial stress on the hub:

$$\sigma_{r,pressure} = -P, \tag{B.2}$$

circumferential stress on the hub due to interference pressure is calculated by:

$$\sigma_{\theta,pressure} = P\frac{D_{ho}^2 + D_{hi}^2}{D_{ho}^2 - D_{hi}^2} \tag{B.3}$$

and the shear stress on the hub caused by torque is calculated by:

$$\tau = \frac{16 \cdot TD_{hi}}{\pi(D_{ho}^4 - D_{hi}^4)}. \tag{B.4}$$

The axial stress on the hub due to axial force is neglected since the pieces interlock mechanically restricting any movement in the axial direction due to thrust. Centrifugal effects are also neglected since the rotation rates are below $10\,000\,\mathrm{r\,min^{-1}}$. The Von Misses stress at the hub at the surface is given by:

$$\sigma_{VM} = \sqrt{\frac{(\sigma_{r,pressure} - \sigma_{\theta,pressure})^2 + \sigma_{\theta,pressure}^2 + \sigma_{r,pressure}^2}{2} + 3\tau^2} \tag{B.5}$$

The same equations can be used to calculate the stresses on the bushing side [78]. By using the material data for stainless steel on the hub side and brass on the bushing side the transmission torque can be calculated for different interference values. Using a trial and error method a suitable interference can be determined that offers a factor of safety of 2 while being much lower than other mechanical connections making it a mechanical failsafe in case of a colition.

15X21X3 HM4 RRadial shaft seal with metal case and single sealing lip, for grease

Radial shaft seal with metal case and single sealing lip, for grease

Radial shaft seals are used between rotating and stationary machine components, or between components in relative motion. HM4 seals are designed with a single metal case. They have a conventional single sealing lip made of elastomer. Typical applications include grease lubricated agriculture machinery.

- Maximise the exclusion of contamination
- Accommodate low speed
- Easy installation

Overview

Dimensions

Shaft diameter	15 mm
Housing bore diameter	21 mm
Seal width	3 mm

Performance

Maximum operating temperature	100 °C
Minimum operating temperature	-40 °C
Permissible circumferential speed	2.96 m/s
Rotational speed	3 780 r/min

Properties

Design	HM4
Auxiliary lip	No
Sealing lip material	Nitrile rubber (NBR)
Type of outside diameter	Metal-cased
Unit system	Metric

Technical Specification

Type of outside diameter	Metal-cased
Lip material	Nitrile rubber (NBR)
Seal design	HM4

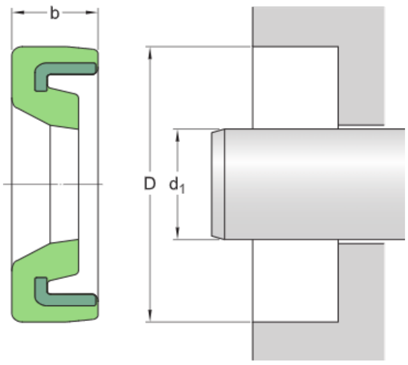

Dimensions

d_1	15 mm	Shaft diameter
D	21 mm	Housing bore diameter
b	3 mm	Seal width

Application and operating conditions

Operating temperature	min. -40 °C
Operating temperature	max. 100 °C
Circumferential speed	max. 2.96 m/s
Rotational speed	max. 3 780 r/min
Pressure differential	0.07 N/mm^2

Associated products

SKF Speedi-Sleeve	99059

R01-F

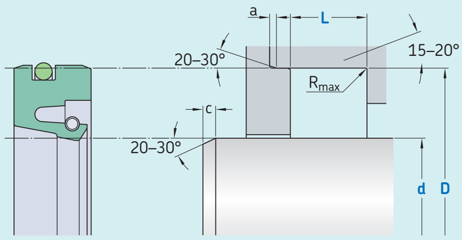

Ordering dimensions in **blue**

Surface roughness	R_{tmax}	R_a
	µm	
Sliding surface	≤ 2	0,05–0,2
Bottom of groove	≤ 6,3	≤ 1,6
Groove face	≤ 15	≤ 3

Hardness: On the surface min 55 HRC, hardened depth > 0,3 mm.
Bearing area: 50–95% and a cutting depth of 0,5 R_z based on C_{ref} = 0%

Standard dimensions

d h11 Rotating application over	incl.	d h11 Pivoting application over	incl.	D H8	L –0,1	c	a	R_{max}
mm								
15	**66**	**15**	**33**	d + 12	7,0	3,0	1,25	0,4
66	**110**	**33**	**55**	d + 16	9,0	3,5	1,50	0,4
110	**280**	**55**	**140**	d + 20	10,0	5,0	2,00	0,4
280	**400**	**140**	**200**	d + 25	12,5	6,5	2,50	0,8
400	**600**	**200**	**400**	d + 30	15,0	7,5	3,00	0,8
		400	**600**	d + 40	20,0	9,0	3,50	0,8

Ordering example

Profile	**Rotary seal R01-F**
d x D x L [mm]	**100 x 120 x 10**
Sealing material / O-Ring / Spring	**SKF Ecoflon 4 / NBR 70 / 1.4310**

R01-F

Operating parameters

Material Seal	O-Ring	Spring	**Temperature** from	to	**Speed**[1)] max	**Pressure** max
			°C		m/s	bar (*MPa*)
■ SKF Ecoflon 4	NBR 70	1.4310	–30	+100	10	15 (*1,5*)
■ SKF Ecoflon 4	FPM 75	1.4310	–20	+200	10	15 (*1,5*)

IMPORTANT NOTE: The stated operating conditions represent general indications. It is recommended not to use all maximum values simultaneously.
1) Surface speed limit values are valid only in the presence of a lubrication film.

PUB SE/P8 11865/2 EN · October 2019